Structural-Acoustic Analysis and Optimization of Embedded Exhaust-Washed Structures

A thesis submitted in partial fulfillment of the
requirements for the degree of
Master of Science in Engineering

By

RYAN N. VOGEL
B.S., Wright State University, Dayton, OH, 2011

2013
Wright State University

WRIGHT STATE UNIVERSITY

WRIGHT STATE GRADUATE SCHOOL

July 25, 2013

I HEREBY RECOMMEND THAT THE THESIS PREPARED UNDER MY SUPERVISION BY **Ryan N. Vogel** ENTITLED **Structural-Acoustic Analysis and Optimization of Embedded Exhaust-Washed Structures** BE ACCEPTED IN PARTIAL FULFILLMENT OF THE REQUIREMENTS FOR THE DEGREE OF **Master of Science in Engineering**.

Ramana V. Grandhi, Ph.D.
Thesis Director

George P. G. Huang, Ph.D., P.E.
Chair, Department of Mechanical and Materials Engineering

Committee on Final Examination:

Ramana V. Grandhi, Ph.D.

Ha-Rok Bae, Ph.D.

Gregory Reich, Ph.D.

R. Williams Ayres, Ph.D.
Interim Dean, Graduate School

ABSTRACT

Vogel, Ryan N. M.S. Egr. Department of Mechanical and Materials Engineering, Wright State University, 2013. Structural-Acoustic Analysis and Optimization of Embedded Exhaust-Washed Structures.

The configurations for high speed, low observable aircraft expose many critical areas on the structure to extreme environments of intense acoustic pressure loadings. When combined with primary structural and thermal loads, this effect can cause high cycle fatigue to aircraft skins and embedded exhaust system components. In past aircraft design methods, these vibro-acoustic loads have often been neglected based on their relatively small size compared to other thermal and structural loads and the difficulty in capturing their dynamic and frequency dependent responses. This approach is insufficient for effective advanced designs of complex aerospace structures, such as internal ducted exhaust systems and sensitive airframes. By optimizing the integrated aircraft components that involve interactions between fluid and structural coupled systems, the structural stresses created from the high acoustic pressure magnitude of the frequency response functions can be reduced, therefore prolonging the fatigue life of the aircraft structure.

This research investigates acoustic excitations generated by structurally integrated acoustic pressure sources and explores the coupling effects of the fluid and structure domains. Utilizing a hybrid optimization scheme that comprises both global and local optimization methods, acoustic related stresses and mass can be simultaneously reduced in these highly dynamic and frequency dependent structural-acoustic aerospace systems.

Table of Contents:

List of Figures:

List of Tables:

Acknowledgements

I would like to thank my advisor Dr. Ramana V. Grandhi for his help and guidance in my graduate career. I would also like to thank my committee members Ha-Rok Bae and Gregory Reich for their valuable feedback and input into my work. I extend my thanks to the sponsors of this work: the Dayton Area Graduate Studies Institute fellowship program and the support provided by the Air Force Research Laboratory through the Collaborative Center for Multidisciplinary Sciences, as well as Dr. Ron Averill from Red Cedar Technology for providing Wright State University with the HEEDS optimization software.

Additionally, I would like to thank fellow students and researchers in CEPRO for their help, advice, criticism, and feedback throughout my research work at Wright State. I would also like to extend a special thanks to my beautiful wife, Jodi, for always believing in me, as well as the rest of my family and friends for the encouragement and support they provided me along the way.

1. Introduction

1.1. Motivation

As aerospace technology continues to advance across the globe, demand is ever increasing for future capabilities of aircraft. These requests call for improvements in extended flight intervals, rapid attack and defense mechanisms, reusable launch system techniques, and improved configurations for low observability. In each of these cases, the critical sections more susceptible to failure, such as aircraft skin, embedded engine exhaust systems, etc., on aircraft structures may endure extreme environments characterized by elevated temperatures, intense acoustic effects, as well as additional structural loads introduced by high speed and prolonged flight. Although many of these disciplines have been considered in the past, most works focus only on part of the combined loading situation that these new extreme conditions pose. In regard to previous methods of aircraft design, often specific loading conditions, such as the ones created from vibro-acoustics, are neglected because of their relatively small contribution compared to other structural or thermal loads. In addition, the response of aircraft components under dynamic acoustic loading has been difficult to predict. This approach is insufficient for the effective design of complex aerospace structures, such as internal ducted exhaust systems and sensitive airframe designs, because the true

structural response is a combined loading effect that requires attention from all disciplines. The high cycle acoustic loads resulting from the vibro-acoustics can significantly decrease the fatigue life of aircraft components when added to primary structural or thermal loading environments. Thus, a multidisciplinary computational analysis and simulation for aerospace structures should be considered in future aircraft designs.

More specifically, when an aircraft travels through the atmosphere at hypersonic speeds during sustained flight, random intense acoustic environments are introduced by the air flow, wake vortices, and the vehicle's propulsion system with varying sound pressure at different locations on the structure. The structural-acoustic pressures transmit random vibration though mechanical substructures and exhaust-washed system components of the aircraft. The addition of vibro-acoustic loading directly on the surface structures at certain excitation frequencies creates high cycle fatigue issues and premature structural failure. As a result, acoustic effects become very significant to the fatigue life of critical constituents that already experience loading forces from structural, aerodynamic, and thermal conditions.

Aircraft that rely on low observability from both radar cross section and infrared detection utilize the concept of embedding engines inside the airframe. Ducted paths for the expulsion of the hot exhaust gases experience extreme thermal loads, while engine noise and exhaust flow contribute wide-band acoustic loading to the same area. The substructures that surround the engine and the components of the exhaust nozzle

or aft deck experience heightened acoustic excitations. Previous research investigated the premature cracking of the aft deck of the B-2 Spirit shown in Figure 1. The work concluded that nonlinear thermal stresses initiated cracking and random acoustic loading accelerated the crack growth to component failure [1].

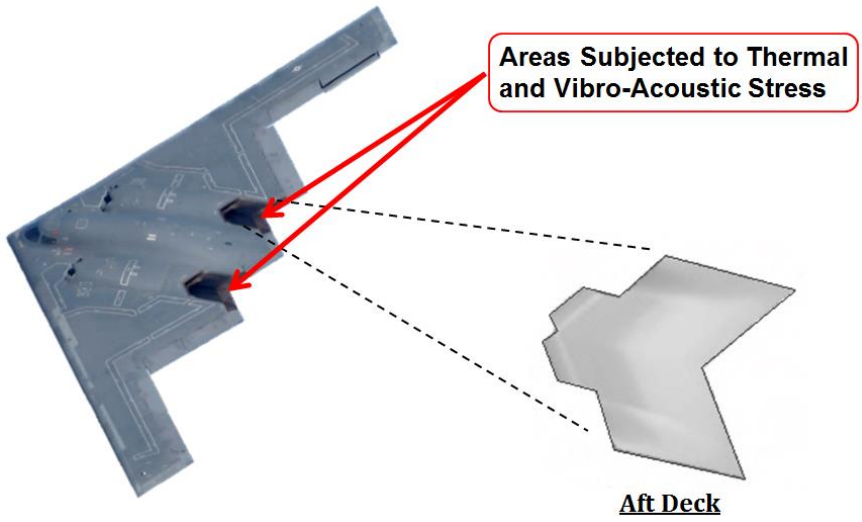

Figure 1: Location of the aft deck structure relative to B-2 aircraft

In the past, multidisciplinary optimization of airframe structures has typically considered aerodynamic and structural disciplines in iterative design processes. Most investigations involved linear structural analysis for static displacements and stresses under multiple flight load conditions. In addition, these procedures used integration of aerodynamic loads computed through panel and computational fluid dynamics to study steady and unsteady flight conditions. The limited number of disciplines that were considered in preliminary designs served well for aircraft in the past. With the current demand for new air vehicle platforms, including the Efficient Supersonic Air Vehicle (ESAV) concept, the technical challenges are much more critical for a reliable and cost

effective operation in new and extreme environments. Notable challenges include the need for structural design based on finite element analysis procedures that can account for the acoustic pressures created from the presence of airframe vibro-acoustics caused by high-lift devices and landing gear and acoustic pressure in engine exhaust-washed structures (EEWS) caused by the implementation of embedded engines [2]. Figure 2 shows the exhaust duct configuration of a high speed, low observability concept aircraft and depicts the problematic areas of loading to which this type of vehicle would be susceptible.

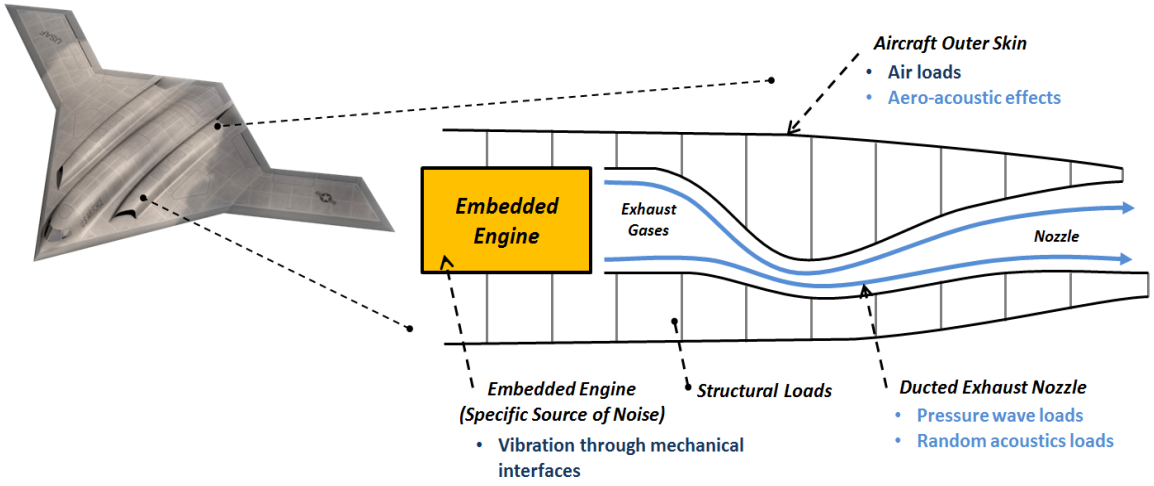

Figure 2: Schematic of high speed, low observability aircraft exhaust duct with combined loading sources

Important acoustic goals in this type of environment include quantifying the loads generated from the specific source of noise (embedded engine) and studying what type of effects acoustic pressure waves and mechanical vibrations have on the system and how they travel throughout the structure. Another important aspect of the work is to locate critical areas of high stress due to the coupled vibrations and acoustic loads

(vibro-acoustic loads) in order to better redesign these areas, therefore prolonging the fatigue life of the structure. Using optimization schemes, not only can the acoustic pressure and stress be reduced, but also the weight of the structure, which is especially beneficial for aerospace applications. So, by analyzing acoustics loads that would be present in a multidisciplinary design of an aircraft, critical components can be redesigned or reinforced using optimization techniques and the fatigue life of system can be improved.

1.2. Document Summary

Although the motivation of this work is aerospace-related, this document sets the groundwork for structural-acoustic analysis and optimization in any environment in which acoustic loading may be important. Investigations were conducted to accurately capture acoustic pressure loads in a fluid domain and efficiently determine the effects of the loads through finite element analysis. Through this work it was determined that the complexity of coupled structural-acoustic systems create multi-model problems in which results are dependent on both space and time. Therefore an optimization procedure that can account for these dependencies was developed and utilized.

The remainder of the paper is organized in the following manner: Chapter 2 begins with a literature review containing information about structural-acoustic analysis and optimization methods and other related work currently used in the field of acoustics. Chapter 3 introduces the critical acoustic equations and other governing

equations needed when solving the structural-acoustic problem, as well as key concepts in understanding acoustic analysis and results. The analysis technique and validations for the work appear in Chapter 4, as well as the results from investigations on the necessity for coupled structural-acoustic analysis. Chapter 5 introduces the need for a hybrid optimization scheme in multi-model problems and discusses the results and findings obtained from the research. Chapter 6 will then summarize the results and research contributions of this work.

2. Literature Review

2.1. Structural-Acoustic Analysis

The study of structural-acoustics and the associated pressure waves has been a field of interest that, although explored in the 60's and 70's, has been receiving much more attention from the research field in the past two decades. This could be the result of stricter demands for new multidisciplinary industrial platforms, where the technical challenges are much more critical for a reliable and cost effective operation under new and adverse stipulations. In the separate works by Hong and Kim [5], Pan and Bies [6], and Pretlove [7], the structural-acoustic problem was studied by using analytical expressions for the two domains. It is apparent in this literature that the two connecting domains, the flexible structure and acoustic cavity, can be adequately coupled together. In this way, the entire system can be studied as a whole, and a coupled fluid-structure analysis is conducted in order to properly evaluate the natural frequency and true response of the dynamic excitations. In several of these models, a theoretical framework of modal based sound fields was investigated for very basic systems.

In most real applications, the vibro-acoustic systems that are studied involve complex shapes and require a fine discretization to capture the geometry. So although analytical functions are the basis for solving the structural-acoustic problem, they

cannot be practically used for describing the spatial distribution of the primary variables. Instead, numerical approaches are utilized. In the acoustics review by Atalla and Bernhard [8], numerical structural-acoustic analysis techniques, such as boundary element methods and finite element methods, are utilized and directly compared to analytical methods. In this work, a comprehensive review was also completed to define more detail on methods used in the community. The numerical approaches provide a way to accurately solve complicated geometries and non-linear structures with high confidence, provided that the user properly defines the boundary conditions and input parameters. Additional comparisons using various elements to more effectively model the coupling between the fluid and structure in acoustic analysis has been explored in Brunner et al. [9], Mejdi and Atalla [10], and Dominquez et al. [11]. In the work of Brunner, various coupling formulations are investigated, and it was found that strong coupling schemes are even more important when simulating vibro-acoustic behavior in thin-walled structures with dense fluids. Atalla developed techniques to better predict the vibro-acoustic response of both unidirectionally and bidirectionally stiffened thin panels. A simplified version of the acoustic pressure forces were used to apply on stiffeners which are used to reduce the thin plate displacements. Further exploration of FE and BE coupling was executed in the work by Dominquez, in which an error analysis was developed in two and three dimensional problems. Through these analysis techniques and coupling schemes it was determined that finite elements are efficient in modeling vibro-acoustic problems and effective in solving even complicated structural-acoustic systems. Another aspect of these acoustic finite element models that resulted

in large errors in the solution was the acoustic element resolution. In the paper by Ihlenburg [12], resolution rules were established, which if followed result in an admissible errors for the finite element solution.

More thorough investigations of finite element methods in structural-acoustics have been a major topic of research in the acoustics field, especially with a focus on dynamic problems. The formulation of coupled structure-acoustic problems using finite element analysis, such as the works by Peretti and Dowell [13], Morand and Ohayon [14], Everstine [15], and Fang et al. [16], explored the system of equations needed to describe the motion of fluid and structural walls. Initially the approaches studied rigid boundary conditions because of the simplicity of the acoustic equations, but have extended to coupling of boundaries in which the structural walls are flexible as shown in the more recent works on thin panel structures. The excitations from the structural walls by the sound source cause vibrations throughout the system and noise within the acoustic domain. Due to the coupling between the structural vibrations and acoustic pressure field, these systems are typically referred to as vibro-acoustic systems. The acoustic formulations for the initial rectangular enclosures were extended to irregular cavities with more flexible structural boundaries in studies conducted by Geng et al. [17] and Meissner [18]. Both of these papers correspond to noise control in rooms and how the acoustic intensity field can be manipulated by using various sound damping distributions. In fact, much of the acoustic literature in the past decade has been devoted to improve quantification schemes on measuring acoustics noise and the reduction of acoustic or environmental sounds through redesign of structures or

applying complex damping materials. Although many of the acoustic research papers implement different strategies to describe and model various structural-acoustic systems, most are primarily concerned with the noise levels and sound intensity within the fluid domain. Reducing the noise levels in house appliances, automobiles, and commercial airliners is important due to their irritating and disturbing effects on human hearing. Studies on noise pollution of compressors by Forouharmajd et al. [19], traffic levels by Onuu [20] and by Rahmani et al. [21], and environmental noise in general by Zannin et al. [22] have been conducted on the purposes of benefiting the public by attempting to reduce these noise levels. This noise reduction becomes even more important to the aerospace field in a military or intelligent defense standpoint when the goal is to prohibit acoustic detection of aircraft by the enemy. The topic of reducing noise and acoustic emissions in aircraft is a pressing objective and has been embedded in the Strategic Research Agenda (SRA) of the Advisory Council for Aeronautic Research in Europe (ACARE) [23], as well as being implemented in programs such as the Great Horned Owl (GHO) by the US Intelligence Advanced Research Projects Activity (IARPA). Currently, noise reduction procedures are employed in Intelligence Surveillance and Reconnaissance (ISR) mission applications in which Unmanned Aerial Vehicles (UAV's) are designed to contain more efficient and quiet power sources and propulsion systems in order to reduce the ability of the target to counter surveillance. The experimental analysis and research on the reduction of external noise generated specifically by UAV's has been conducted by Sinibaldi and Marino [24], in which several concepts are explored to reduce detectability of these aircraft.

The reduction of acoustic noise levels and environmental sound, although a relatively new field, has been previously explored and well documented. Even purely devoted acoustic and environmental sound programs has been developed, such as the NASA built Aircraft Noise Prediction Program (ANOPP) which is used to quantify the external noise generated from acoustic sources at a distance. Programs like these can be utilized to quickly determine far-field acoustic effects from various aircraft components like landing-gear which was studied in the work by Burley et al. [25]. However, a typical acoustic source not only emits noise in the air, but also indirectly, through substructures and mechanical interfaces via structure-borne and fluid-borne paths [26]. While the characterization of structural-borne sources [27-30] have been dealt with fairly extensively, the direct air-borne characterization effects along with coupled vibrations has received less attention. Therefore, this work is focused towards the acoustic loading effect that is observed in intense acoustic fields with close structural boundaries. In this type of research, the primary objective is to reduce the structural effects and impact from the acoustic source loads originating from embedded engine aircraft. There are several techniques that can be used to suppress vibration and noise, and among these is the addition of damping materials which is utilized extensively in applications from transportation to structures [31]. However, in these design configurations, adding advanced dampening material is many times infeasible due to the intense thermal temperatures and possibility of the obstruction of exhaust flow. Therefore, a thickness redesign approach of existing material and substructural supports is investigated in this research. As previously specified, the acoustic excitations generated in this environment

can cause a negative influence on the fatigue life of critical components on embedded engine aircraft. Therefore, this work looks to relate the acoustic pressure to structural stresses, and couple these effects with the structural vibrations present in the system in order to effectively model the response.

2.2. Structural-Acoustic Optimization

Since numerical acoustic analysis is relatively new in the engineering field, there are only a limited number of optimization approaches that have been explored. Also, the optimization process in structural-acoustics is computationally expensive and leaves some uncertainty in the quality of optimum results achieved based on approximations used in low fidelity simulations. Finding the optimal solution in any dynamic system with frequency or time dependency is challenging. One of the first to publish on optimization in these dynamical acoustic systems was Olhoff [32]. In this work, vibrating circular plates were redesigned to maximize the fundamental frequency by changing the dimensions and material of the structure. A similar optimization approach was used by Thambiratnam and Thevendran [33] in which vibrating beams and plates' thicknesses were optimized while keeping the volume of the structure constant. Again, in this way the fundamental frequency could be shifted. This work was important because it studied the effects of changing boundary conditions which significantly altered the structural-acoustic effects and optimization results. A method for optimization of nodal point placements using a sensitivity analysis was developed by Pritchard, Adelman, and

Haftka [34]. Using the sensitivity analysis to minimize generalized force, vibration control was obtained on helicopter rotor blades in this study.

In more recent optimization research, Bai and Liu [35] utilized genetic algorithm in their optimization scheme to improve panel speakers by achieving omnidirectional responses in higher frequencies. Utilizing this procedure, optimal higher excitation frequencies were determined to yield optimal performance. Other forms of global optimization schemes were utilized by Lee and Park [36] and Fritze et al. [37]. Lee and Park developed a global robust optimization technique that utilized kriging approximation models. The kriging model approximations reduced the number of functional acoustic calculations to a manageable amount for the global optimizer. Then the robustness of the global optimum was determined from a simulated annealing algorithm, and further refinement of this design was achieved through a post process approximation method. In the research conducted by Fritze and his colleagues, approximation methods were again utilized, only this time to reduce the RMSL of the acoustic signature. In this way, he was able to correlate the reduction of RMSL to the reduction of radiated sound power. However, the research was inconclusive on whether this different acoustic measurement technique was able to increase the optimization method performance.

Local optimization techniques were also explored in structural-acoustic problems. Qzakca and Hinton [38] developed an acoustic optimization algorithm that combined a semi-analytical sensitivity analysis with a sequential quadratic programming

method. This method was applied to shape optimization of square plates and cylindrical shells to either maximize the fundamental frequency or minimize volume in these acoustic problems. In the works performed by Ranjbar et al. [39, 40], several optimization approaches, both global and local, are explored to find the benefits of each method in various vibro-acoustic systems. Optimization approaches such as random search, tabu search, neural networks, simulated annealing, along with others, are utilized in the shape optimization of rectangular plate models. These forms of advanced shape optimization techniques lead into other advanced types of structural-acoustic optimization strategies like topology optimization, which was utilized in the works of Akl et al. [41], Jensen and Pedersen [42], Yoon et al. [43], Maeda et al. [44], Bendsoe et al. [45], and Du and Olhoff [46].

Although there have been optimization procedures already researched for noise reduction and frequency manipulation, most literature does not focus on the acoustic loading effect on the structural health of systems. Various optimization techniques regarding complex sandwich panel structures [47-49] and damping treatments [50] attempt to reduce the vibro-acoustics in the systems, but not on a structural health monitoring basis. The research by Aginsky and Gottlieb [51] begins to optimize the structural-acoustic systems based on a thickness parameterization of the variables. This work looks at near-field acoustics and attempts to reduce both acoustic properties and system vibration. The acoustic excitations and vibrations on the structural walls of an embedded engine structure, however, are significantly larger and have a much more significant effect to the structural integrity of the system. This causes the peak pressures

of the frequency response functions in these already complex dynamic and frequency dependent systems to be much more drastic and sensitive to change. The optimization scheme in this paper attempts to compensate for this by using a hybrid optimization technique in which a global optimizer determines the input variable parameters that are utilized by a gradient based local optimization method. Hybrid optimization of dynamic systems have been studied in the past works by Monnigmann et al. [52] and Yildiz et al. [53], however these problems did not account for frequency and spatially dependent problems in which fluid and structurally coupled systems behave and require a large computational cost. Utilizing a hybrid optimization scheme, in which a global and local (gradient-based) optimization method are sequentially applied, not only can we account for the structural-acoustic problem dependent on space, frequency and time, but we can significantly reduce the mass and acoustic related stress in the system while decreasing our computational expense.

3. Methodology

While considering a three-dimensional structural-fluid problem, one needs to properly model both the structure as well as the fluid, and the interaction between these two domains. When the fluid flow (fluid-structure interaction or FSI) or acoustics (structural-acoustic interaction) causes a deformation of the structure, the deformed structure can in turn have an effect on the fluid domain due to changing boundary and interface conditions. These types of interactions occur in most models where a flexible body has an internal or surrounding fluid. In many engineering problems where gases, such as air, are incorporated into the system, a majority of the effects seen in the coupled fluid-structure behavior are contributed by the structure. In some systems, the contribution from the gas or fluid in the model is so trivial that an analysis of only the structural response is sufficient for a decent approximation of the response. If the accuracy of only accounting for the structural response is adequate for the analysis, the computational cost can be significantly reduced by simply not modeling the fluid. However, if the fluid domain does have an effect on the system's total response, inaccurate results will be produced by not modeling the coupled problem and the coupling interactions. Therefore, before any in depth analysis is done on a vibro-acoustic problem, in which a structural and fluid domain exists, it is crucial to determine whether the acoustics in the fluid domain has an effect on the total response.

The Navier Stokes equations that describe the motion of the fluid, not only represents the fluid flow, but also in the weak form represents the acoustic pressure waves' movement. In a structural-acoustic system, acoustic waves constitute a pressure fluctuation that can exist in a compressible fluid domain. In this domain, the pressure changes that occur when the fluid is compressed or expanded create the restoring forces that are responsible for propagating an acoustic wave. These restoring forces are the forces with which the fluid body resists deformation and can be thought of similar to the restoring forces in a spring. In this research, the three-dimensional fluid is modeled using conventional fluid elements in Abaqus. The individual elements of the fluid move back and forth in the direction of the forces (which can be initiated through acoustic loading inputs or structural borne vibrations) producing adjacent regions of compression and refraction similar to longitudinal waves in a beam. These available elements in Abaqus are utilized in modeling a fluid medium that can be coupled to a structural system and the ability to model a variety of dynamic interactions between the two domains. The acoustic element formulations utilize fluid equation definitions and structural-acoustic analogies to better represent the fluid domain. The details of the structural-acoustic methods used and the formulation of the coupled finite element matrix are discussed in detail in the following sections.

3.1. The Equation of State

The equation of state for a fluid relates the internal restoring forces to the corresponding deformations. For fluid medium, the equation of state must relate the physical quantities describing the thermodynamic behavior of the fluid. The equation of state for perfect gas is:

$$p_i = \rho r T_K \tag{1}$$

Where p_i is the total instantaneous pressure in Pascals, ρ is the fluid density in kilograms per cubic meter, and T_K is the absolute temperature in Kelvin. Greater simplification can be achieved, because acoustic processes are nearly isentropic (adiabatic and reversible). This is due to the heat diffusion being much slower than the acoustic vibrations, meaning that the thermal conductivity of the fluid and temperature gradients are small enough that no significant thermal energy transfer occurs between adjacent fluid elements. Therefore, the entropy of the fluid remains nearly constant, and the acoustic behavior can be described in the adiabatic equation:

$$\frac{p_i}{p_0} = \left(\frac{\rho}{\rho_0}\right)^{\gamma} \tag{2}$$

Where p_0 is the equilibrium pressure, ρ_0 is the constant equilibrium fluid density, and γ is the ratio of specific heats. For fluids other than a perfect gas, the adiabatic relation in (2) becomes more complicated. However, the relationship between pressure and density fluctuations can still be represented by a Taylor Series expansion:

$$p_i = p_0 + \left(\frac{\partial p_i}{\partial \rho}\right)_{\rho_0} (\rho - \rho_0) + \frac{1}{2}\left(\frac{\partial^2 p_i}{\partial \rho^2}\right)_{\rho_0} (\rho - \rho_0)^2 + \cdots \quad (3)$$

Here the partial derivatives are determined for isentropic compression and expansion of the fluid about its equilibrium density. When these fluctuations are small, only the lowest order term needs to be retained, giving a linear relationship between the pressure fluctuation and density

$$p_i - p_0 \approx \beta(\rho - \rho_0)/\rho_0 \quad (4)$$

Where β is the adiabatic bulk modulus defined as $\rho_0(\partial p_i/\partial \rho)_{\rho_0}$. In terms of acoustic pressure, $p = p_i - p_0$, and condensation, s, the relationship between pressure and condensation can be written as

$$p = \beta s \quad (5)$$

3.2. The Equation of Continuity

The equation of continuity gives a functional relationship between the particle velocity and the fluid density, which connect the fluid motion with its compression or expansion. The rate with which the mass increases in the volume is $(\partial \rho/\partial t)dV$. The net influx must equal the rate of increase and the equation in which this can be accomplished is

$$\frac{\partial \rho}{\partial t} + \nabla \cdot \left(\rho \dot{u}_f\right) = 0 \quad (6)$$

Where $\dot{u}_f$ refers to the fluid particle velocity. The second term on the left involves the particle velocity and instantaneous density, both of which are acoustic variables.

3.3. Euler's Equation

Euler's equation, utilizing the conservation of momentum, is a simple nonlinear inviscid force formulation that is obtained using Newton's second law:

$$\rho\left[\frac{\partial \dot{u}_f}{\partial t} + (\dot{u}_f \cdot \nabla)\dot{u}_f\right] = -\nabla p \tag{7}$$

If changes in momentum are negligible, this equation becomes linearized resulting in the linear Euler's equation

$$\rho_0 \frac{\partial \dot{u}_f}{\partial t} = -\nabla p \tag{8}$$

3.4. The Linear Wave Equation

The linearized equations (5), (6), and (8) can be combined to yield a single differential equation with one dependent variable, which is the linear wave equation.

$$\nabla^2 p - \frac{1}{c^2}\frac{\partial^2 p}{\partial t^2} = 0 \tag{9}$$

Where p is the acoustic pressure at any point, c is the phase speed for acoustic waves in the fluid, and t is time. The variable c can also be defined as: $c = \sqrt{\beta/\rho}$. This linearized wave equation assumes small and irrotational motion and locally isentropic pressure-density. This equation is used to solve for the pressure at any field point location with respect to time.

If the acoustic pressure is harmonic in time with frequency ω, the problem now deals with standing waves where the perturbations can be written as:

$$p(x,t) = \hat{p}(x)g(t) \tag{10}$$

Where $\hat{p}(x)$ is the pressure function in terms of only position and $g(t) = e^{\pm i\omega t}$. As a result:

$$\frac{1}{g(t)}\frac{\partial^2 g(t)}{\partial t^2} = -\omega^2 \tag{11}$$

The substitution of equation (10) into equation (9) yields:

$$\hat{p}(x)\frac{\partial^2 g(t)}{\partial t^2} - c^2 g(t)\nabla^2 p(x) = 0 \quad \rightarrow \quad \frac{c^2}{\hat{p}(x)}\nabla^2 p(x) = \frac{1}{g(t)}\frac{\partial^2 g(t)}{\partial t^2} \tag{12}$$

From (11), the right side of the equation equals $-\omega^2$ as shown:

$$\frac{c^2}{\hat{p}(x)}\nabla^2 \hat{p}(x) = -\omega^2 \tag{13}$$

Defining the wave number k, as $k = \omega/c$, where ω is the angular frequency, the wave equation (9) becomes the Helmholtz equation.

$$\nabla^2 \hat{p} + k^2 \hat{p} = 0 \tag{14}$$

The solutions of the Helmholtz equation for a domain with specified shape and boundary conditions are the normal modes of the problem. The wave equation or the Helmholtz equation are relevant to complete the fluid domain and describe the fluid behavior in a system, and are essential when analyzing a structural-acoustic problem in which the fluid interacts with the structure. Since both equations (9) and (14) are the differential equations, dependent on time and frequency respectively, they must be converted to a different form so that the structure and interaction/coupling terms can be more easily included in a model that can be solved using finite element methods. The following sections will show how this relation is established, as well as the interaction terms in a structural-acoustic system.

3.5. Interface Boundary Conditions

The structural-acoustic boundary conditions for the fluid field at the structural-fluid interface can be obtained from Euler's momentum and continuity equation considerations. This boundary condition can be defined for the pressure formulation on a flexible structural interface as:

$$\frac{\partial p}{\partial n} = -\rho \ddot{u}_n^f \tag{15}$$

Here, the normal acceleration component of the fluid particle, $\ddot{u}_n^f$, at the interface between the structure and fluid is related to the gradient of the acoustic pressure field. Again, ρ refers to the fluid density and $\frac{\partial}{\partial n}$ is the derivative in the direction n normal to the interface. When this relation is added as a boundary condition, it produces a forcing term in the equation for the acoustic pressure field which is accounted for and defined in more detail in the following *Variation Principle* section. This pressure formulation of the boundary condition can be expressed for various boundaries like a boundary on a rigid wall as:

$$\frac{\partial p}{\partial n} = 0 \tag{16}$$

on a free surface of zero ambient pressure,

$$p = 0 \tag{17}$$

Other types of boundary conditions such as impedance or infinite boundaries are sometimes required in a structural-acoustic problem, but these types of boundary conditions require different formulations and will be discussed in more detail in the following sections.

3.6. Relation of Differential Acoustic Equation to Finite Element Method

The preceding sections developed differential equations and boundary conditions that are relevant to the complete fluid domain. In order to utilize the efficiency of the finite

element method, an integral relation is required. This relation is especially useful for implementing computational FEA solvers which are better suited and capable of handling large structural-acoustic problems and complex coupling interactions. When this relation is solved, it provides an approximate solution to these differential acoustic equations and boundary conditions. There are several methods to obtain the integral functional finite element equation of motion, such as direct application of the weighted residual method, formation of the system on the basis of a variational principle, and structural analogies for scalar field problems to name only a few. A variational principle approach is commonly used because it typically bounds well to a well-posed numerical solution. Another relation technique that has been accepted which develops the same result, is one in which an analogy is used to relate the wave or Helmholtz equation to elasticity and common mathematical equations.

3.7. Variational Principle

The scalar formulation of the fluid equation of motion is obviously appealing since it results in a minimum number of fluid degrees of freedom while still satisfying the irrotational fluid condition. Also, utilizing scalar forms of the fluid/acoustic equations work better with the scalar forms of the structural equations of motion and degrees of freedom that can be more easily utilized in finite element methods. Therefore, these formulations are immediately applicable for the solution of the linearized wave equation or the Helmholtz equation. The wave equation (9), with $\beta = c^2\rho$, can be

integrated over the fluid volume and multiplied by a virtual pressure δp to get the integral:

$$\int_V \left[\frac{1}{\beta} \frac{\partial^2 p}{\partial t^2} - \frac{1}{\rho} \nabla^2 p \right] dV \delta p = 0 \tag{18}$$

This equation represents the virtual work expression for the acoustic pressure. Then the second term of (18) can be integrated by parts using Green's theorem to get:

$$\int_V \frac{1}{\beta} \frac{\partial^2 p}{\partial t^2} \delta p dV + \delta \int_V \frac{1}{2\rho} \nabla p \cdot \nabla p \, dV - \int_S \frac{1}{\rho} \nabla p \cdot dS \delta p = 0 \tag{19}$$

Because there is no easy way to factor out δp from each integral to obtain a direct and simple variational statement, the Galerkin method is typically applied to get a more useful form of the equation. Applying this method will allow the factorization of δp from the first term, while also defining the normal acceleration of the fluid from the surface is defined as $\ddot{u}_{n_o}^f$ results in the integral:

$$\Pi = \int_V \left[\frac{1}{\beta} p \frac{\partial^2 p}{\partial t^2} + \frac{1}{2\rho} \nabla p \cdot \nabla p \right] dV + \int_S \ddot{u}_{n_o}^f \, p \, dS \tag{20}$$

and the variational statement becomes

$$\delta \Pi = 0 \tag{21}$$

The fluid pressure at any location can now be defined using the row matrix of pressure shape functions $\lfloor \mathrm{N}_f \rfloor$ and nodal pressure vectors $\{p\}$ in the following definition

$$p = \lfloor N_f \rfloor \{p\} \tag{22}$$

The expression for Π can now be expressed as:

$$\begin{aligned} \Pi = \lfloor p \rfloor \int_V \frac{1}{\beta} \{N_f\} \lfloor N_f \rfloor dV \left\{ \frac{\partial^2 p}{\partial t^2} \right\} \\ + \lfloor p \rfloor \int_V \frac{1}{2\rho} \{\nabla N_f\} \lfloor \nabla N_f \rfloor dV \{p\} + \lfloor p \rfloor \int_S \{N_f\} \ddot{u}_{n_o}^f dS \end{aligned} \tag{23}$$

Regarding the normal acceleration of the fluid, if n_o refers to the outward normal fluid and n refers to the structure boundary normal pointing inward into the fluid, then naturally $n_o = -n$ as shown in Figure 3,

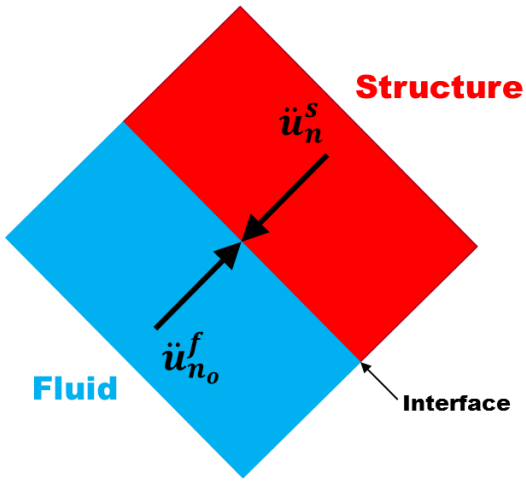

Figure 3: Normal acceleration of the fluid and structure at the interface

The surface integral can now be written as:

$$\lfloor p \rfloor \int_S \{N_f\} \ddot{u}_{n_o}^f dS = -\lfloor p \rfloor \int_S \{N_f\} \ddot{u}_n dS \tag{24}$$

The term $\ddot{u}_n$ can further be defined using the direction of cosines matrix $[C]$, and establishing $[\mathrm{N}_s]$ as the matrix of structural shape functions and $\{\ddot{u}_s\}$ as the matrix of structural nodal accelerations at the boundary. The normal acceleration component can be defined as:

$$\ddot{u}_n = \lfloor C \rfloor [N_s] \{\ddot{u}_s\} \tag{25}$$

$$\ddot{u}_n = \lfloor N_s \rfloor \{\ddot{u}_s\} \tag{26}$$

Therefore, equation (24) can be defined as:

$$-\lfloor p \rfloor \int_S \{N_f\} \ddot{u}_n^s dS = -\lfloor p \rfloor \int_S \{N_f\} \lfloor N_s \rfloor dS \, \{\ddot{u}_s\} \tag{27}$$

Then, $\delta\Pi$ can be computed and the following integrals can be defined:

$$[M_f] = \int_V \frac{1}{\beta} \{N_f\} \lfloor N_f \rfloor dV \tag{28}$$

$$[K_f] = \int_V \frac{1}{\rho} \{\nabla N_f\} \lfloor \nabla N_f \rfloor dV \tag{29}$$

$$[A^T] = \int_S \{N_f\} \lfloor N_s \rfloor dS \tag{30}$$

Where $[M_f]$ is the fluid mass matrix, $[K_f]$ is the fluid stiffness matrix, and $[A]$ is the coupling matrix that includes both the fluid shape function N_f and structural shape function N_s respectively. Note that while the mass and stiffness matrices are integrated over the volume of the fluid, the coupling matrix is integrated over the surface that the fluid and structure share. These integrals can be combined to form the fluid equation of motion defined as:

$$[M_f]\{\ddot{p}\} + [K_f]\{p\} - [A^T]\{\ddot{u}_s\} = 0 \tag{31}$$

If the effect of acoustic source density is included, the virtual work expression in equation (18) will yield an acoustic load $\{P_f\}$ on the right hand side of (31). This acoustic load refers to the input acoustic pressure load that can be applied to the fluid domain. Also, when damping is included in the fluid, the frequency dependent wall impedance $z = p/\dot{u}_f$ is applied at the structural-fluid interface introducing the damping matrix term $[B_f]\{\dot{p}\}$. Therefore, the fluid equation of motion becomes:

$$[M_f]\{\ddot{p}\} + [B_f]\{\dot{p}\} + [K_f]\{p\} = \{P_f\} + [A^T]\{\ddot{u}_s\} \tag{32}$$

Where, again, $\dot{u}_f$ is the fluid particle velocity, $[B_f]$ is the fluid damping matrix, and $\{P_f\}$ is the applied acoustic load. Now, the fluid pressure at the structural-fluid boundary causes surface tractions on the structure which can be represented by the relationship shown in (33).

$$\{F_s\} = \int_S [N_s]^T \{\varphi\} dS \tag{33}$$

However, the surface traction is related to pressure by the definition $\{\varphi\} = -p\{C\}$. Therefore, the forcing function can be redefined as:

$$\{F_s\} = -\int_S [N_s]^T \{C\} p \, dS = -\int_S \{N_s\} \left[N_f\right] dS\{p\} = -[A]\{p\} \tag{34}$$

The common structural equation of motion will now also contain the fluid pressure on the interface nodes as defined in (34):

$$[M_s]\{\ddot{u}_s\} + [B_s]\{\dot{u}_s\} + [K_s]\{u_s\} = \{P_s\} - [A]\{p\} \tag{35}$$

Where $[M_s]$ is the structural mass matrix, $[B_s]$ is the structural damping matrix, $[K_s]$ is the structural stiffness matrix, $\{P_s\}$ is the externally applied structural forcing function, and as before $\{u_s\}$ is the nodal structural displacements. Combining the equation of motion for both the fluid (32) and the structure (35), the structural-fluid coupled matrix can be built:

$$\begin{bmatrix} M_s & 0 \\ -A^T & M_f \end{bmatrix} \begin{Bmatrix} \ddot{u}_s \\ \ddot{p} \end{Bmatrix} + \begin{bmatrix} B_s & 0 \\ 0 & B_f \end{bmatrix} \begin{Bmatrix} \dot{u}_s \\ \dot{p} \end{Bmatrix} + \begin{bmatrix} K_s & A \\ 0 & K_f \end{bmatrix} \begin{Bmatrix} u_s \\ p \end{Bmatrix} = \begin{Bmatrix} P_s \\ P_f \end{Bmatrix} \tag{36}$$

The output when solving this equation is expressed in terms of the nodal structural displacements $\{u_s\}$ and the fluid pressures $\{p\}$.

3.8. Method of Analogies

A method of analogies that uses solid three-dimensional structural elements ideology can produce the same structural-acoustic matrix equation (36) for the pressure field in the fluid domain [54]. Many engineering linear problems involve the solution of the equation in a general form:

$$\nabla^2\alpha + v = a\ddot{\alpha} + b\dot{\alpha} \tag{37}$$

Where ∇^2 is the Laplacian operator, functions v, a, and b are, in general, position dependent, α is an unknown scalar function that depends on both position and time, and the dots denote partial time differentiation. The commonality among all these problems is the mathematical model. The structure, assuming that it can remain elastic, behaves in accordance to classical elasticity and the various approximations established mechanical theory of beams, plates, and shells. In a structural-acoustic interaction problem, the acoustic medium behaves as a fluid whose pressure p satisfies the scalar wave equation (9) or α in the generalized equation (37). Again, the boundary condition at the fluid-structure interface can be obtained from momentum and continuity considerations as shown in Eq. (15). Special cases of (37) arise in diverse engineering applications such as acoustics, heat conduction, and potential fluid flow. These special cases include both the wave equation and Helmholtz equation. In accordance with the analogy developed by Everstine [54], equation (37) and the Navier equations of classical elasticity can be solved with elastic finite elements.

For example, the linearized wave equation in (9) can be defined in Cartesian co-ordinates with the time dependent term on the right hand of the equation as:

$$\frac{\partial}{\partial x}\left(\frac{1}{\rho}\frac{\partial p}{\partial x}\right)+\frac{\partial}{\partial y}\left(\frac{1}{\rho}\frac{\partial p}{\partial y}\right)+\frac{\partial}{\partial z}\left(\frac{1}{\rho}\frac{\partial p}{\partial z}\right)=\frac{1}{\beta}\frac{\partial^2 p}{\partial t^2} \tag{38}$$

Utilizing the classical expression for equilibrium of stresses in the x direction can be shown as:

$$\frac{\partial \sigma_{xx}}{\partial x}+\frac{\partial \tau_{xy}}{\partial y}+\frac{\partial \tau_{xz}}{\partial z}=\rho_s\frac{\partial^2 u_x}{\partial t^2} \tag{39}$$

Where σ_{xx} , $\partial\tau_{xy}$, and $\partial\tau_{xz}$ are the stress components, u_x is the structural displacement, and ρ_s is the structural density. Using Hooke's Law, the stress to strain relationship can be established:

$$\begin{Bmatrix}\sigma_{xx}\\ \tau_{xy}\\ \tau_{xz}\end{Bmatrix}=\begin{bmatrix}G_{11} & G_{14} & G_{16}\\ G_{14} & G_{44} & G_{46}\\ G_{16} & G_{46} & G_{66}\end{bmatrix}\begin{Bmatrix}\varepsilon_{xx}\\ \gamma_{xy}\\ \gamma_{xz}\end{Bmatrix} \tag{40}$$

Where G_{ij} is an element of a 6 by 6 elastic material matrix. In this analogy, since the x-component of displacement is chosen to represent the scalar field variable (α in Eq. 32), all other components of displacement are constrained in the field. Since the displacement components in the y and z direction are zero, the stain-displacement relationship becomes:

$$\varepsilon_{xx}=\frac{\partial u_x}{\partial x} \tag{41}$$

$$\gamma_{xy} = \frac{\partial u_x}{\partial y} \tag{42}$$

$$\gamma_{xz} = \frac{\partial u_x}{\partial z} \tag{43}$$

Since u_x represents the scalar pressure, the strains are analogues to the pressure gradients. Comparing (38) to (39) and taking the relationships,

$$\sigma_{xx} = \frac{1}{\rho}\frac{\partial p}{\partial x} \tag{44}$$

$$\tau_{xy} = \frac{1}{\rho}\frac{\partial p}{\partial y} \tag{45}$$

$$\tau_{xz} = \frac{1}{\rho}\frac{\partial p}{\partial z} \tag{46}$$

$$u_x = p \tag{47}$$

$$\rho_s = \frac{1}{\beta} \tag{48}$$

$$G_{11} = G_{44} = G_{66} = \frac{1}{\rho_s} \tag{49}$$

$$G_{14} = G_{16} = G_{46} = 0 \tag{50}$$

it can be shown that the equations (38) and (39) are analogous. It is clear that the equations of elasticity can represent the acoustic wave equation with certain matrix modifications within the properties of the elements. Utilizing a method of analogies

enables the differential acoustic equation to be defined in a matrix acoustic equation to obtain a fluid equation of motion:

$$\left[M_f\right]\{\ddot{p}\} + \left[K_f\right]\{p\} = 0 \tag{51}$$

This equation becomes the same as equation (32) when the structural acoustic boundary condition is applied and the coupling matrix is included, fluid damping is considered, and an acoustic forcing function involving the pressure of the fluid on the structural interface.

3.9. Boundary Conditions

In the previous section, several conditions were specified for the boundary at the structural fluid interface: fluid bounded to an elastic structure, to a rigid structure, and on a free surface which is free of zero ambient pressure. Another type of interface boundary condition that can be applied is an impedance boundary condition, in which the equation for impedance is shown as:

$$z = \frac{p}{\dot{u}_f} \tag{52}$$

Where, as specified previously, p is the acoustic pressure and $\dot{u}_f$ refers to the fluid particle speed. This boundary condition determines the degree to which the acoustic waves that are incident upon this boundary are scattered, transmitted, or dissipated. Even if damping properties are not assigned to the fluid or the structure, damping terms

are introduced into the structural-acoustic coupled equation when an impedance boundary condition is specified, due to the presence of the velocity term.

The boundary conditions applied to the rest of the structural-fluid system, not just at the fluid-structure interface, must also be considered in a structural-acoustic analysis. The boundary conditions applied to the structure are basic in all finite element analysis techniques; however, the boundary conditions applicable for the acoustic interface are much less commonly explored. These boundaries can include the ones in which an acoustic load is applied or in applications where the acoustic elements are modeled external to the structure. The latter of the two instances, involves modeling an infinite fluid domain like the ones seen in problems such as submarines submerged in water, automobile mufflers open to the environmental air, and speakers radiating sound in a large or open room. Exterior acoustic problems like these can be modeled using finite element methods as long as special conditions are applied at the outer boundary. Two methods to model this infinite boundary are non-reflecting impedance conditions and acoustic infinite elements. Both types of conditions have pros and cons when implementing them into a finite element model, which will be discussed in the following sections.

The impedance boundary condition can be used to model a non-reflecting boundary condition on the acoustic region. The impedance boundary can be used to model anything from a rigid boundary that reflects all incident acoustic waves, to one in which all the acoustic waves are totally absorbed. Most realistic acoustic boundaries

present a condition that falls somewhere in between these two extremes, where most of the acoustic waves pass through the boundary but some waves are reflected back into the system. Impedance boundary conditions can model this phenomenon, as long as the default radiating condition is modeled relatively far away from the acoustic source, otherwise numerical errors are introduced. The influence of these errors for an acoustic finite element formulation using a polynomial basis function of order m can be approximated as:

$$\vartheta = \left(\frac{\tilde{k}\tilde{h}}{m}\right)^{m} = D \tag{53}$$

Where D is a constant, m is the order of the element used, $\tilde{h}$ is a measure of the FE mesh resolution defined as $\tilde{h} = h/L$ where h is the average mesh size and L is the characteristic problem dimension, and with $\tilde{k} = k/L$ where k is the acoustic wave number ($k = 2\pi/\lambda$) with λ being the acoustic wavelength. Typically a rule of thumb for fluids is that $D = 1$ for an acceptable accuracy which translates to the use of at least six linear acoustic elements or four quadratic per single acoustic wavelength. So in other terms, the equation for wavelength, λ, is:

$$\lambda = \frac{c}{f} \tag{54}$$

Where again, c is the speed of sound in the fluid (air at 1 atm and 20 ℃ results in c = 343 m/s) and f is the frequency of excitation in Hz. Therefore, for lower excitation frequencies, more acoustic elements are needed to accurately model the acoustic

pressure waves. Due to the need to capture effects at lower frequencies in this particular research, the computational cost can get very expensive. Therefore the method of applying acoustic infinite elements is more appealing for systems in which most of the pressure waves leaves the system (enters the unbounded domain). Acoustic infinite elements are elements that model a boundary in which total acoustic wave absorption takes place. This boundary condition is similar to the non-reflecting impedance boundary condition, except that an additional external finite element mesh is not needed to capture an accurate effect because the acoustic infinite elements can be directly coupled to the finite acoustic or structural region at a high order of approximation. As long as the structural-acoustic system has minimal acoustic pressure waves reflected back into the system at the boundary to the unbounded domain, an infinite acoustic boundary can be used to significantly reduce the computational cost of modeling an external acoustic element domain.

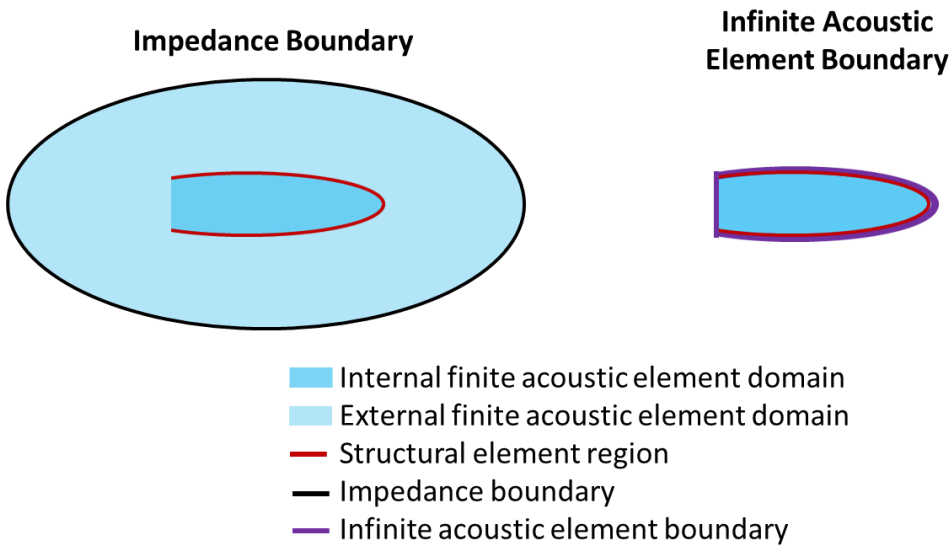

Figure 4: Schematic of impedance and infinite acoustic boundary conditions

3.10. Introducing Flow in Acoustic Analysis

Another aspect of an acoustic analysis in a problem containing both a structure and fluid is the inclusion of flow velocity in the fluid domain. Fluid flows are governed by partial differential equations which represent conservation laws for the mass, momentum, and energy, as was shown in the formulation of the acoustic wave equation and Helmholtz equation. Typically Computational Fluid Dynamics (CFD) is used to model these flow fields because it provides a quantitative prediction of the fluid flows by means of mathematical modeling, numerical methods, or software tools. However, computational flow analysis is typically computationally expensive in comparisons to structural analysis techniques. Therefore, when a structural analysis is already coupled with an acoustic analysis, combining an additional CFD analysis may be challenging in the engineering optimization sequences because of time and resource limitations. In some flow field applications, the fluid flow is moderately steady over a long period of time and can be modeled with a mean flow effect. Therefore, to keep the solution of a vibro-acoustic problem at a lower computational cost, a mean flow technique can instead be used to approximate the fluid flow. The mean flow allows the use of the linear wave equation for a fluid at rest to describe the acoustic field. However, the mean flow does not account for the actual fluid flowing effect on the structure (FSI) or the non-linear fluid flow behaviors at high supersonic speeds.

A mean flow application can approximate interior flows such as turbo machinery, pipe and exhaust manifold flows, and muffler flows, as well as exterior flows like those

seen when modeling noise and flutter analysis in aircraft. The flow velocity in these vibro-acoustic problems, affects the propagation of the acoustic waves in the flow direction. In this type of analysis, the flow velocity shortens the acoustic pressure wavelengths with the flow, and extends them against the flow. Due to this effect, acoustic waves can be treated as perturbations of the background flow field. However, this ideology is restricted to problems with a restricted Mach flow number. This can be explained by using a general steady-state solution of one-dimensional flow:

$$p(x,t) = \left[D_1 e^{-\left(\frac{ikx}{1+M}\right)} + D_2 e^{\left(\frac{ikx}{1-M}\right)}\right] e^{i\omega t} \tag{55}$$

Here k represents the quiescent wavenumber and M is the Mach number. Note that the propagation speed is different in the positive and negative directions, where in the positive direction, the speed of sound is higher and the wavelength longer. The opposite effect occurs in the negative direction. The methodology of including this mean flow into an acoustic analysis only works on subsonic flows ($M < 1$) because the density of the flow remains constant. So the statement of equilibrium for small motions of a compressible fluid in three-dimensional vector form can be expressed as:

$$\frac{\partial p}{\partial x} + \gamma \dot{u}_f + \rho \ddot{u}_f = 0 \tag{56}$$

where γ is the volumetric drag coefficient. With the introduction of mean flow, the equilibrium equation translates to:

$$\frac{\partial P_0}{\partial x} + \frac{\partial p}{\partial x} + \gamma\left(v_o + \dot{u}_f\right) + \rho\ddot{u}_f + v_o\frac{\partial \rho}{\partial t} = 0 \tag{57}$$

where P_0 is the ambient pressure and v_0 is the mean flow velocity of the fluid. The differential equation including the mean flow velocity term can then be related to the finite element method through the variation principle to include its effects in the coupled structural-acoustic matrix.

3.11. Sound Pressure Level

Another important aspect of acoustic analysis that is utilized in the following investigations is sound pressure level. Sound pressure level (SPL) refers to the physical intensity of sound, and can be defined as the ratio of absolute sound pressure and a reference level in the following equation:

$$SPL = 20log_{10}\left(\frac{p}{P_{ref}}\right) \tag{58}$$

where p is the acoustic pressure expressed in Pascals and P_{ref} is the reference sound pressure in the fluid medium (for air approximately 20 μPa). Since this is a logarithmic relationship, small sound pressure levels convert to negligible values of sound pressure, whereas a large SPL will translate to a massive amount of pressure. To emphasize this, a plot was created with an SPL range of contributing pressures.

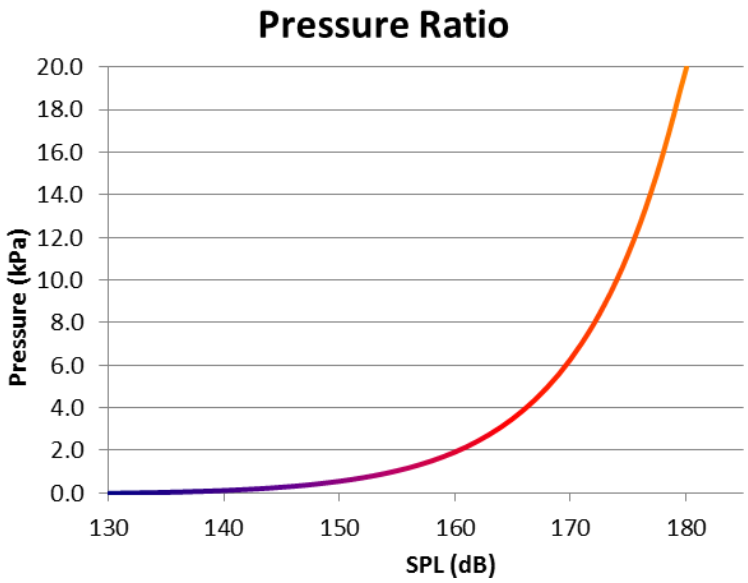

Figure 5: SPL to Pressure Ratio

To better relate the SPL to acoustic noise examples, the table was created below that shows various noise sources with their distances.

Table 1: Sound pressure level chart [55]

Sound Sources (Noise) Examples with Distance	Sound Pressure Level dB
1 Pound T.N.T. (4.5m)	180
12 Gauge Shotgun Blast	165
Jet Engine (50m)	140
Threshold of Pain	130
Sandblasting, Loud Rock Concert	120
Chainsaw (1m)	110
Snowmobile, Motorcycle	100
Diesel Truck (10m)	90
Curbside of Busy Road (5m)	80
Vacuum Cleaner (1m)	70
Conversational Speech (1m)	60
Average Home Noise	50
Quiet Library	40
Quiet Bedroom at Night	30
Background in TV Studio	20
Threshold of Hearing	0

It may not appear that 130 dB translates to very much pressure, but actually 130 dB is the threshold of pain for human hearing. Also, many times acoustic SPL values are defined as the RMS amplitude of the acoustic signature. The acoustic pressure profile can be thought of as a sinusoidal wave function as shown in Figure 6.

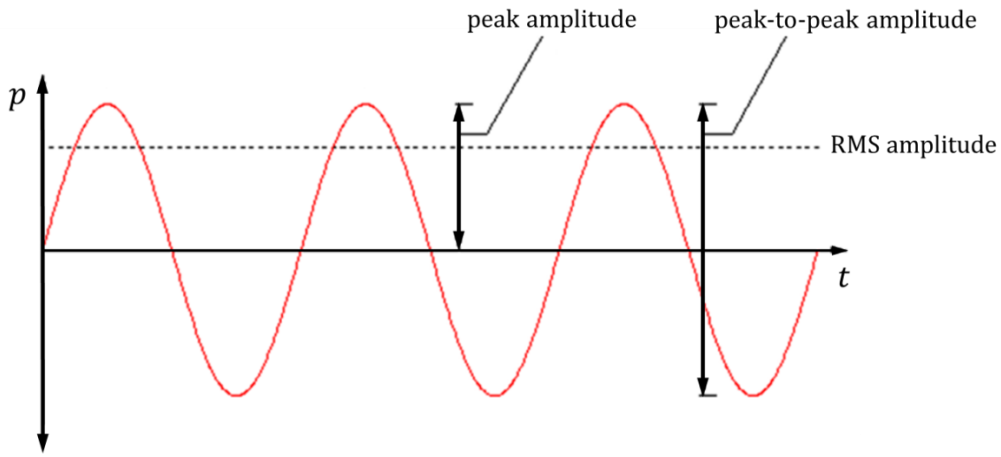

Figure 6: Acoustic pressure loading

The actual peak amplitude is larger than the RMS amplitude that is usually defined when regarding the SPL because it is easier to quantify in most systems where the peak amplitude is not the same for every wavelength. Also, it should be noted that this dynamic pressure loading is applied at a high rate in which many cycles are observed. Therefore, the large difference between the *peak-to-peak amplitude* observed in the above figure can have the effect of a load that is 2x the measure peak amplitude. So in the systems, like embedded exhaust-washed structures where the internal substructural components are located in a very close proximity to the acoustic source, the SPL level will be at the higher end of the SPL spectrum shown in Figure 5. From Figure 5, one can see that reducing the sound pressure level by only two decibels at 180 dB will have

much more of an effect than reducing the sound pressure level by 10 decibels at 140 dB. For a high cycle fatigue problem, a small reduction of sound pressure level at high decibel levels will be even more significant.

To further emphasize the severity of the acoustic load, one can use the distance law for sound pressure equation:

$$p_2 = p_1\left(\frac{r_1}{r_2}\right) \tag{59}$$

where p_1 and p_2 are the acoustic pressures at location 1 and 2, and r_1 and r_2 are the radius of locations 1 and 2 from the sound source. The relationship between the relative sound pressure and distance can be seen in the plot below.

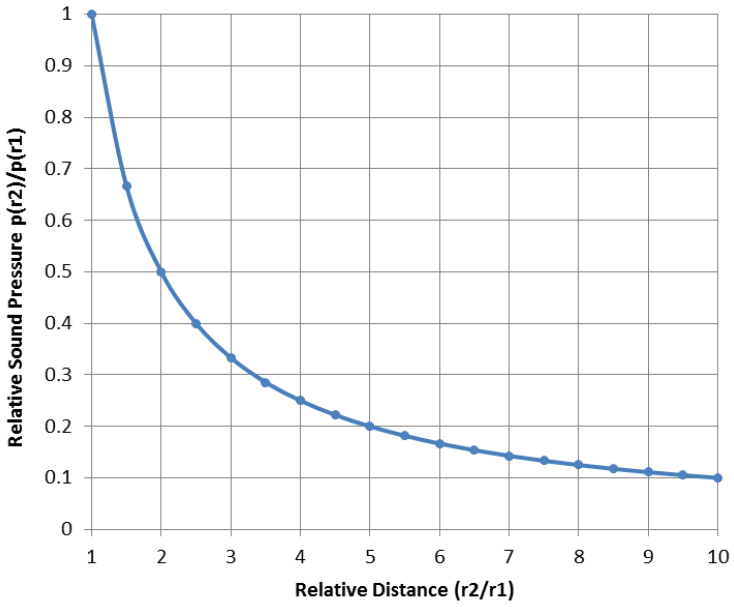

Figure 7: Inverse distance law for sound pressure

Therefore, to get an approximate idea of the SPL that could be observed in an embedded engine model, one can look at Table 1 and see that a commercial jet engine

at 50 meters away produces a SPL of approximately 140 dB. By using Eq. (59) the SPL can be back calculated to find what this SPL translates to at locations closer to the sound source and this is represented in Figure 8.

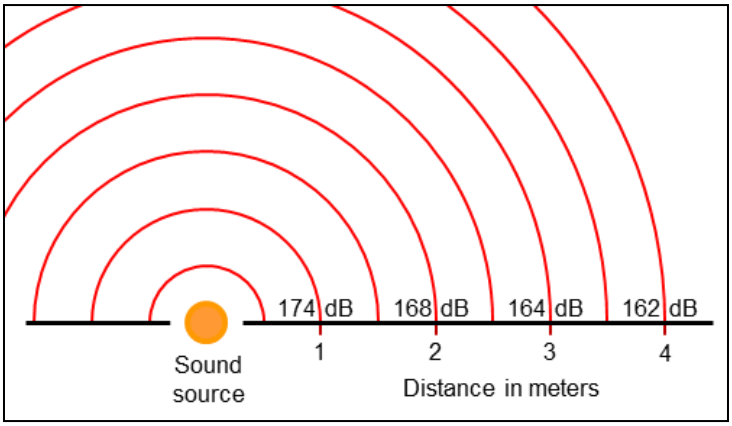

Figure 8: SPL of commercial jet engine at close proximities

As the above figure shows, an engine that measures 140 dB at 50 meters is approximately equal to 174 dB at one meter. In embedded engine exhaust washed systems, the internal structures experience much higher levels of sound pressure like observed in the plot. From the experimental results found in the works of Gordon and Hollkamp [4], in which aluminum panels were tested in acoustic chambers, sound pressure levels were measured to be anywhere from 150-180 dB. These calculations on acoustic source loadings, along with the confirmation of acoustic specialists at the Air Force Research Laboratory (AFRL) at Wright Patterson Air Force Base in Ohio, rationalize the extreme acoustic loading environments in embedded exhaust system applications.

3.12. Chapter Summary

The acoustic equations and concepts presented in this chapter are essential in the calculations for structural-acoustic problems. Utilizing the assumptions of small and irrotational motion, the fluid equations can be reduced to forms that capture the acoustic behavior and effects. Using integral relations, the acoustic equations can be solved using the finite element method, in which the structure and coupling/interaction terms between the two domains can be more easily represented. Representing these complex structural-acoustic equations in forms that FEA programs, like Abaqus, can efficiently solve the problem is especially beneficially when incorporating special boundary conditions and infinite domains. The definitions and SPL ideology will be used throughout the remainder of this research.

4. Finite Element Analysis in Structural-Acoustics

4.1. Model Representation

In this work, the objective as specified in the introduction to this document is to use a representative model of an exhaust system from an embedded-engine aircraft to explore the acoustic characteristics in this multidisciplinary loading environment. For this research, one can look at any type of embedded engine concept model and use a commercial FEA package to model the complex curved geometry of the duct walls, the supporting substructures and mechanical interfaces, the aircraft skins, and the inlet and outlet conditions as well as any other boundary conditions present as shown in Figure 9.

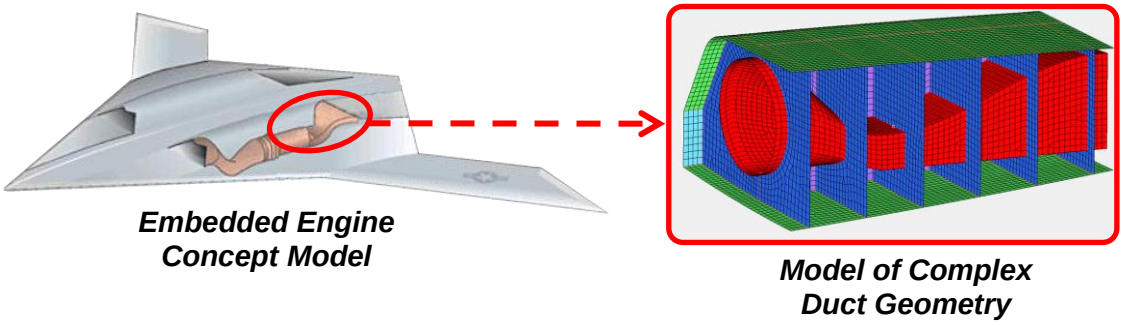

Figure 9: Embedded Exhaust System Representation

However, for this research we want to obtain a better understanding of the acoustic phenomena that is occurring within this type of environment. Therefore a simplified version of the complex curved geometry model is utilized, and shown in Figure 10.

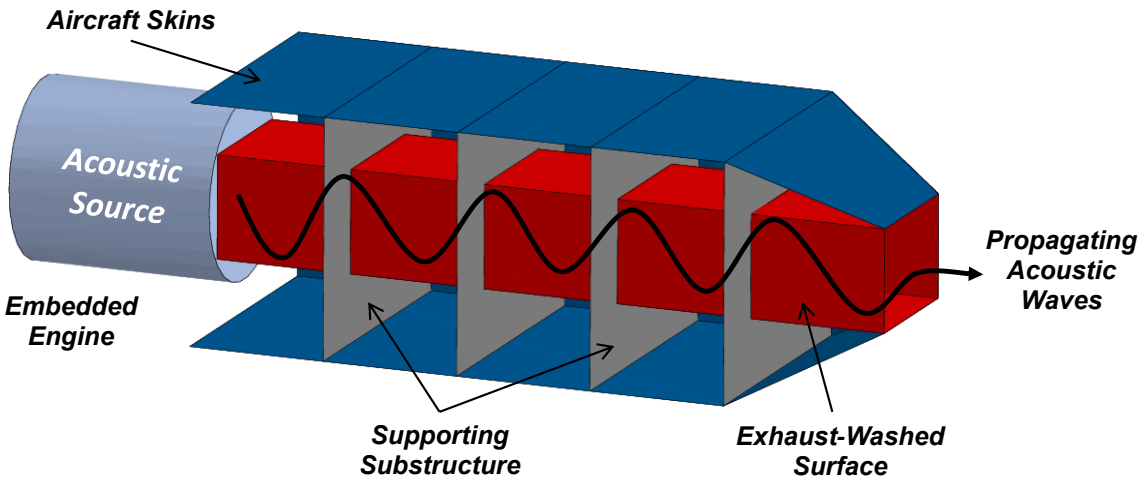

Figure 10: Representative Engine Exhaust-Washed Structure

In this figure, many of the same defined components and characteristics from an actual model can still be captured, only at a simplified version. As shown from the above figure, the actual curved geometry of an EEWS is represented by a rectangular cross-section duct, and the complicated supporting structures are simulated by using a reduced number of rectangular panels. All of the corresponding boundary conditions from a higher fidelity finite element model can still be captured in a reduced fidelity model. The aircraft skins can still be modeled as well, or boundary conditions can be used to approximate these structures. In fact, through FEA investigations it was determined that in the current model, simple supported boundary conditions resulted in approximately the same acoustic related stress in the duct structure as a model that

included geometrical definitions for air craft skins and associated properties. Therefore boundary conditions can be used to reduce the computational cost of analyzing additional air craft skin elements. The actual acoustic forcing function from the engine input is a complicated acoustic signature that experiences various stages of intense high cycle frequencies during service. Also, the mounting configuration of the engine and the inlet to the embedded exhaust structure contains intricate support mechanisms that would be difficult to model. Since the acoustic source loading data, as well as the engine/inlet configuration, is not specifically available, a representative dynamic distributed pressure load applied as a sinusoidal forcing function is implemented instead. This load is distributed across a plate structure connected to the front of the duct system. In this way, not only can the acoustic loads from the engine be accounted for, but also the mechanical vibrations traveling through the side duct walls and mechanical interfaces that a real engine would transmit. Since the representative system is modeled with basic definitions, the coupling effects between the acoustics in the fluid and the structure, the influence of changing boundary conditions at the duct's outlet, the impact of various mechanical substructural definitions, and other results, will all be more obvious in the analysis of the system. A 2D cross-sectional view of the simplified EEWS is shown in Figure 11.

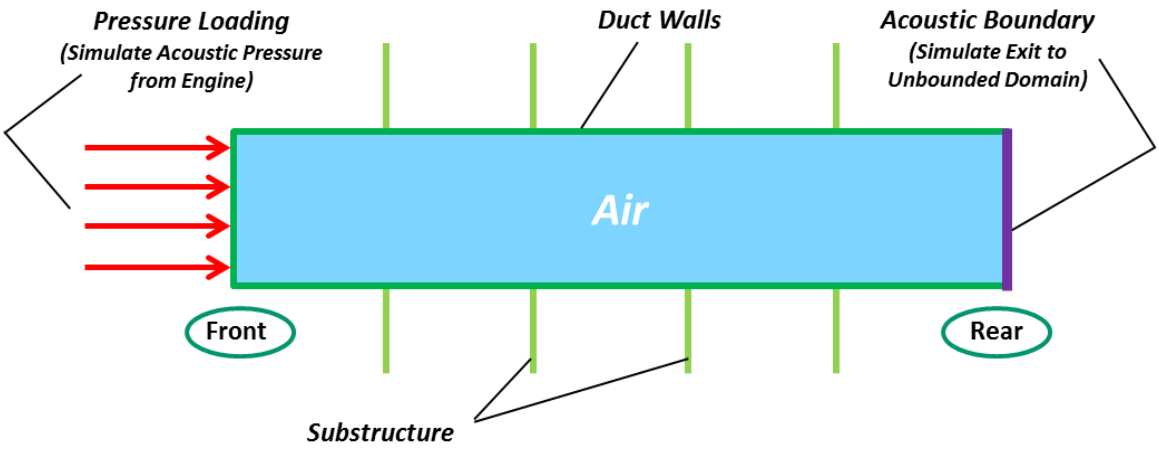

Figure 11: Cross-sectional view of EEWS

The material used for the structure is Aluminum Alloy 2024-T4 with a damping coefficient for the aluminum material of ζ = .004 or 0.4% [4]. Standard air at 20 °C and 1 atmospheric pressure is used to approximate the fluid domain. In reality, high technological composite materials are needed for the duct structure, which would increase the stiffness of the system, and high temperature exhaust of an unknown composition is most likely observed in the fluid domain, resulting in an increase in the speed of sound which would propagate acoustic pressure waves through the duct more quickly. However, for this research, the goal is to develop an acoustic analysis technique that can be used in any interacting structural-acoustic environment and account for any type of material property implementation.

4.2. Finite Element Model

In this research, numerical approaches through finite element methods are utilized along with the computational analysis tool, Abaqus [56]. This FEA program was used

because of its ability to effectively model fluid/structural interface coupling conditions, calculate combined acoustic pressures and structural stresses, provide implicit or explicit direct integration procedures, and model infinite acoustic boundary conditions [56].

The finite element model was created to study the interaction between the plate vibrations and the associated sound radiation into the air cavity. In this category of FEA models, four types of elements were primarily used to model the two different mediums. The structural plate elements (both the duct and substructure) were modeled using an S4 element, which is a conventional shell quadrilateral plate element. These elements account for finite membrane strains and arbitrarily large rotations; therefore they are suitable for large-strain analysis. The fluid elements were modeled using AC3D8 elements, which are defined as eight-node linear acoustic brick elements. Since the grids associated with the AC3D8 continuum elements are defined as fluid grid points, the degrees of freedom of the element become only the Fourier coefficients of the pressure function. Another element type needed in this work is the acoustic-structural interface (ASI) coupling element, which account for all the structural-acoustic coupling terms defined in Chapter 3. The interface was modeled using ASI3D4 elements, which are defined as 4-node linear element where a normal direction must also be defined. The connectivity of the acoustic interface elements and the right-hand rule define the normal direction for this element. For the mathematics to properly work out at the structural-acoustic interface, it is important that this normal points into the acoustic medium, as shown in the ASI3D4 element in Figure 12. These elements can be

automatically generated in Abaqus using TIE constraints, which automatically defaults the normal to the correct direction. Lastly, the infinite elements were modeled using an ACIN3D4 element, which is defined as a four-node acoustic infinite element with linear surface interpolation. These types of elements are used in boundary value problems defined in unbounded domains. In this element definition, a pole or reference point must be created so that the normal vectors from the element's nodes, point away from the pole and into the infinite domain.

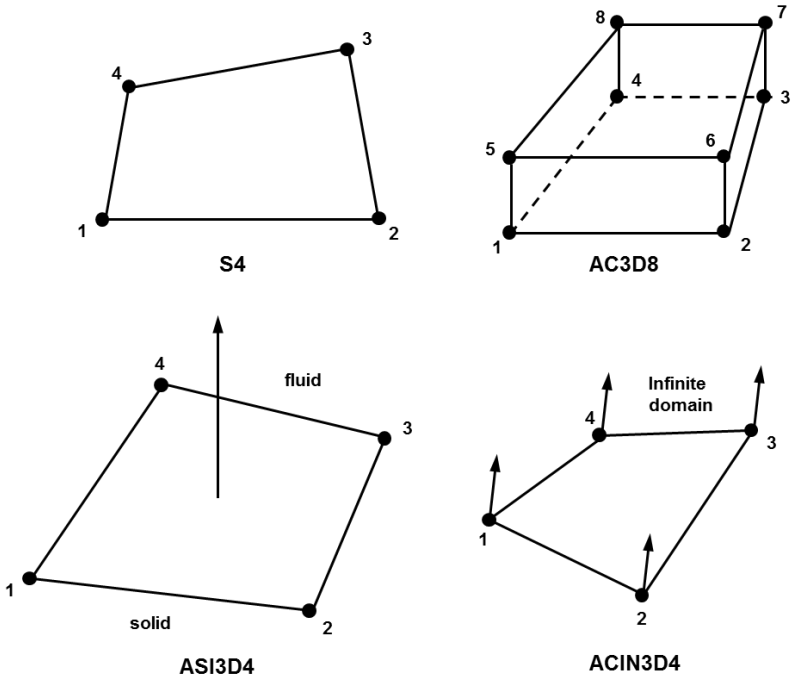

Figure 12: Elements used in modeling system

Before the finite element model for this research was created using the primary group of elements from Figure 12, many comparisons and studies were first conducted to determine the validity of using the structural-acoustic modeling capabilities of Abaqus. Although many of these investigations were carried out to better understand

the acoustics effects in FE models and validate the acoustic analysis procedure in Abaqus, only some of these studies were included in the thesis documentation and can be found in the Appendix. The discoveries found and knowledge gained through these investigations was imperative in developing better future acoustic models, like the ones used in the remainder of this research document.

Once the computing capabilities of Abaqus were validated for structural-acoustic problems, the geometry and finite element model could be established. In this setup, an acoustic cavity measuring 0.75 x 1.0 x 5.0 cubic meters is enclosed by five structural walls. At the rear of the duct, an infinite acoustic boundary is implemented to represent an opening to an unbounded domain. Four substructural panels, with the same properties as the main structure, are connected to the duct structure at intervals of one meter. This is to model the support structure found within the aircraft for the engine exhaust system. Mechanical drawings of the structural parts of the system can be seen in Figure 13.

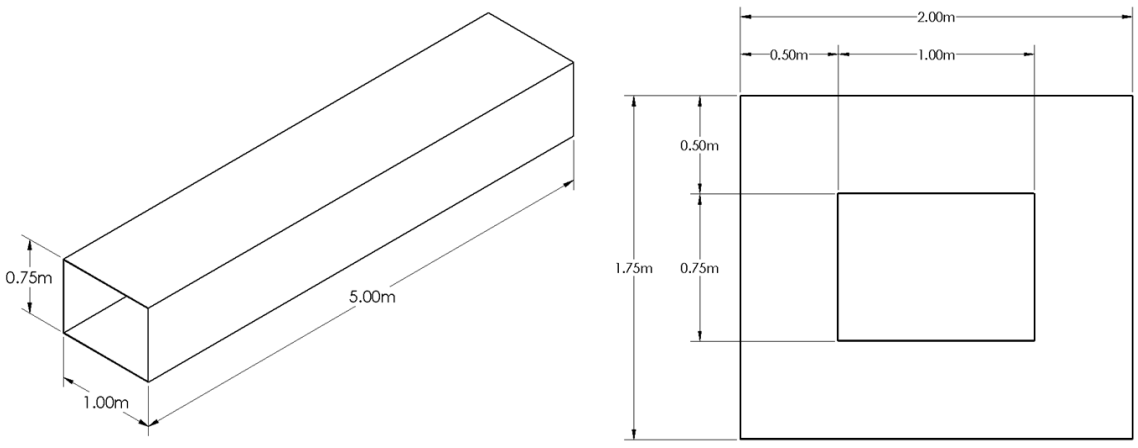

Figure 13: Mechanical drawings of the duct (left) and substructure (right)

Once the geometry configuration was built, a mesh convergence study was conducted on the system. Since the acoustic elements use the linearized wave equation which assumes small and irrotational motion, the acoustic behavior can typically be captured using a courser mesh of fluid elements compared to that of the structural mesh. This is beneficial from a computational basis, since in this model the fluid is the geometrically larger of the two domains. It is also feasible to have a finer structural mesh than the acoustic mesh because Abaqus can account for a coupled analysis in which the nodes from the fluid domain do not have to necessarily match up with the nodes from the structure due to interpolation schemes. Therefore, the convergence study was first performed on the fluid separately and then on the structural-fluid combined system, details of which can be seen in 8.3 of the Appendix. Once mesh convergence was accomplished in the model, the following meshed models were used in further research.

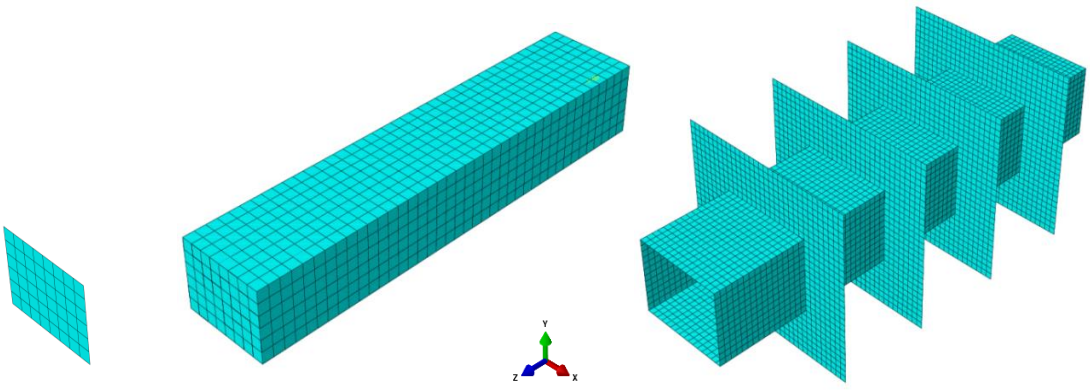

Figure 14: Meshed infinite boundary (left), fluid (middle), and structure (right)

Note that in regards to the element size on the duct portion of the model, the fluid has 8 elements span the width (x-direction) and 6 elements span the height (y-direction) compared to the structure where 16 elements and 12 elements are needed respectively.

This mesh convergence resulted in a fluid domain mesh of 1920 acoustic brick elements and 48 acoustic infinite elements, and a structural mesh of 7488 shell elements. The material properties assigned to these elements as well as the element count breakdown can be seen in the following properties table.

Table 2: Properties of the fluid-structure coupled system

Structure	Material	Aluminum 2024-T4
	Young's Modulus	72.4 GPa
	Density	2770 kg/m³
	Poisson's Ratio	0.33
	Elements (Duct)	4480
	Elements (Substructure)	704 x 4 Panels
Fluid	Cavity Dimensions	.75m x 1m x 5m
	Domain	Air at 20 °C and 1 atm
	Density	1.21 kg/m³
	Speed of Air	343 m/s
	Elements (Fluid Cavity)	1920
	Elements (Infinite)	48

Boundary conditions were applied to the plate, as shown in Figure 15, which fixed the nodes along the four edges of the structure in translation but are free in rotation. This creates a simply supported boundary condition on all four sides of the structural front and rear of the model. Identical boundary conditions were also applied to the outside edges of the sub-structural plates. Note that although Figure 15 does not represent the boundary conditions very well, every node along these edges is assigned the boundary condition as in Figure 16.

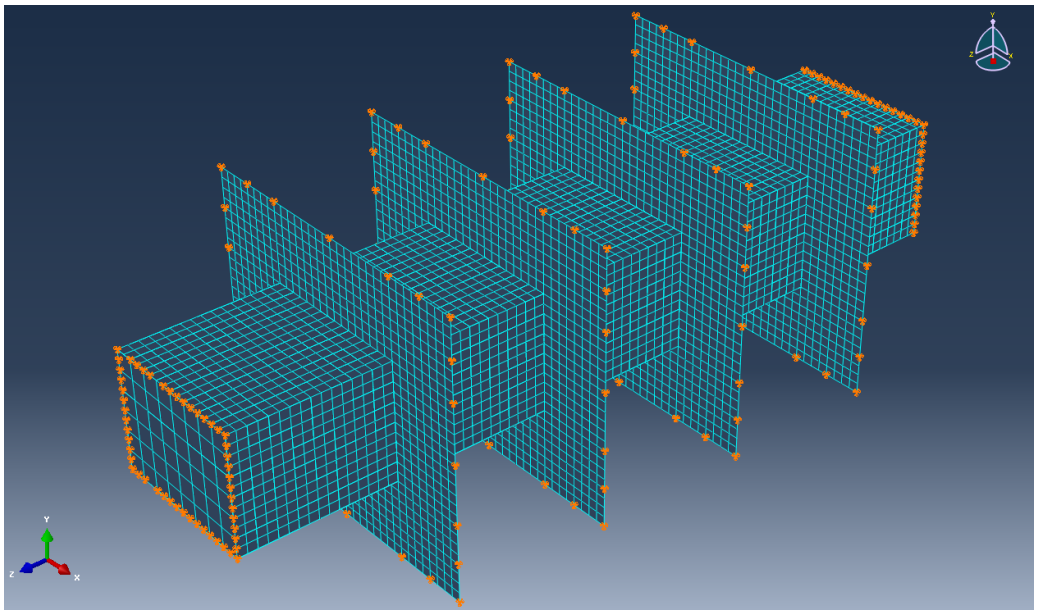

Figure 15: Structural boundary conditions

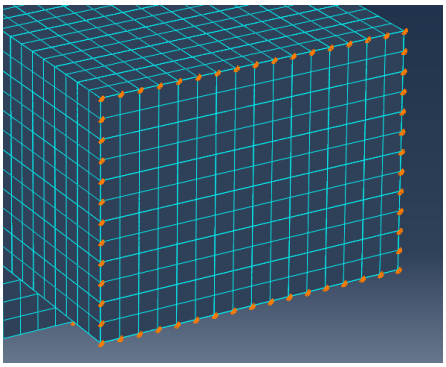

Figure 16: Structural boundary conditions on front of duct

The current geometrical setup and boundary conditions were applied after various representations were tested. Fixed boundary conditions caused the system to be too stiff, while only pinned boundary conditions at the ends of the duct created a very flexible system. The substructures with pinned boundary conditions give the model more flexibility than the fixed conditions and more support than the pinned only boundary conditions. These formulations were created by finding the eigenvalues of

multiple boundary condition configurations. The flexible model had a shift down in eigenfrequencies, while the more rigid model had a shift up. The intermediate model's natural frequencies fell in between the two extremes, making the model a better representation of the embedded exhaust washed system, while still retaining its simplicity. However, structural stresses near any approximated boundary condition will be inaccurate. Therefore, the stresses and acoustic pressures were obtained from the duct itself, away from the substructural boundary conditions, which results in a more realistic stress response. In regards to the acoustic pressure in the fluid domain, the results were nearly indifferent to which boundary condition was applied, as well as additional modeling of stagnant air in between the substructures (outside the duct). Therefore, in this analysis the simply supported boundary conditions on the specified edges were used, and only the fluid within the exhaust duct was included in the model going forward.

Once the finite element model was established, several acoustic effects were explored on the model that turned out to have a significant effect on the finite element results. One effect that was explored was the importance of analyzing the coupled fluid structural model and how the mode shapes and natural frequencies can differ from the uncoupled system, which is discussed in Section 4.3. The effect of modeling the boundary conditions in an external acoustic problem that contains an unbounded domain was also evaluated in Section 4.4. In Section 4.5 an investigation on how the acoustic pressure changes as the thickness of the surrounding structure increases was explored.

4.3. Evaluation of the Coupled vs. Uncoupled Duct System

The first case study explored in this document is the coupling effects of the FE model. In some acoustic related problems involving gases, just the uncoupled structural model response may be accurate enough. As shown in Eq. (36), the coupled structural acoustic matrix depends primarily on the mass and stiffness of the components. In many cases where gases, such as air, are incorporated into the system, a majority of the coupled matrix is contributed by the structure. In some systems, the contribution from the gas or fluid in the system is so trivial that an analysis of just the structural response is sufficient. If the accuracy of only the structural response is adequate, the computational cost can be significantly reduced by simply not modeling the fluid in the FE model. But if the fluid does slightly affect the system, erroneous results will be produced by not modeling the coupled problem. Determining the need for the coupled structural acoustic matrix is crucial in most vibro-acoustic simulations [57].

In order to determine whether coupled responses are needed, a frequency analysis was performed to calculate the first 10 natural frequencies of the fluid separately, the structure separately, and the fluid-structure coupled system. The duct wall thickness and the substructure thickness were given initial values of 5 mm. All other properties were kept the same as described in the previous section. The eigenfrequencies, calculated using a Lanczos eigensolving approach, are shown in Table 3.

Table 3: Natural frequencies of model in Hz

Mode	Structure	Fluid	Coupled System
1	29.32	9.38	8.31
2	30.71	37.38	27.98
3	32.33	70.21	29.93
4	32.45	103.80	31.27
5	33.64	137.50	31.99
6	34.86	171.09	32.00
7	35.33	171.13	33.30
8	37.21	176.88	34.96
9	37.58	187.87	37.17
10	39.71	203.32	37.66

For better comparison purposes, the fluid and structural modes were combined into a broad category of "Uncoupled" natural frequencies and then sorted. As seen from Table 3, a majority of these uncoupled modes are contributed by primarily the structure (only the first and tenth modes are from the fluid). Using participation factors and inspecting modal analysis plots allows one to see which of the "Coupled" modes have mostly structural or mostly acoustic contributions. It turns out, that both the first and tenth modes of the coupled system are also primarily fluid modes, all of which are denoted in blue in Table 4.

Table 4: Natural frequencies of the coupled and uncoupled model in Hz

Mode	Uncoupled	Coupled
1	9.38	8.31
2	29.32	27.98
3	30.71	29.93
4	32.33	31.27
5	32.45	31.99
6	33.64	32.00
7	34.86	33.30
8	35.33	34.96
9	37.21	37.17
10	37.38	37.66

In the following figures, contour plots of the first five modes of both the uncoupled and coupled cases are shown from this analysis. In the fluid modes, the contour plot shows the change of acoustic pressure throughout the cavity. In the structural modes, the contour plot shows the change in nodal displacement scaled so that the locations of maximum displacement are clearly visible. For better visibility in the coupled figures below, the structure is hidden for the fluid modes and the fluid cavity is hidden for the structural modes. Note that the analysis was not done separately for the independent materials as it was in the uncoupled analysis. It should also be noted, that the front of the models is located on the right side in these figures, and the aft or outlet is located on the left.

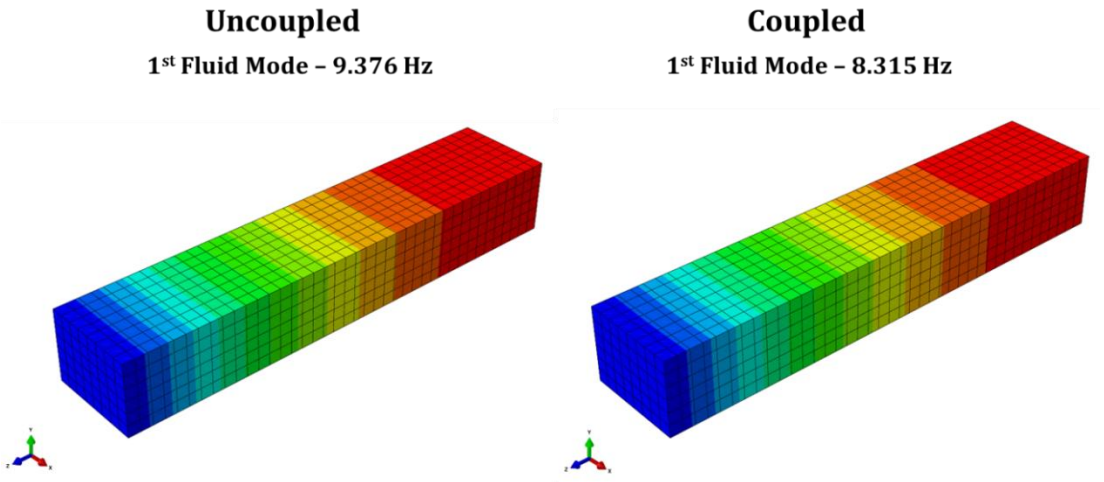

Figure 17: First mode shapes

Mode 1 is a fluid mode for both the uncoupled and coupled analysis. It can be seen that although the two modes differ in frequency, the mode shapes are identical. This observation in the fluid modes was true for even higher fluid modes that were seen.

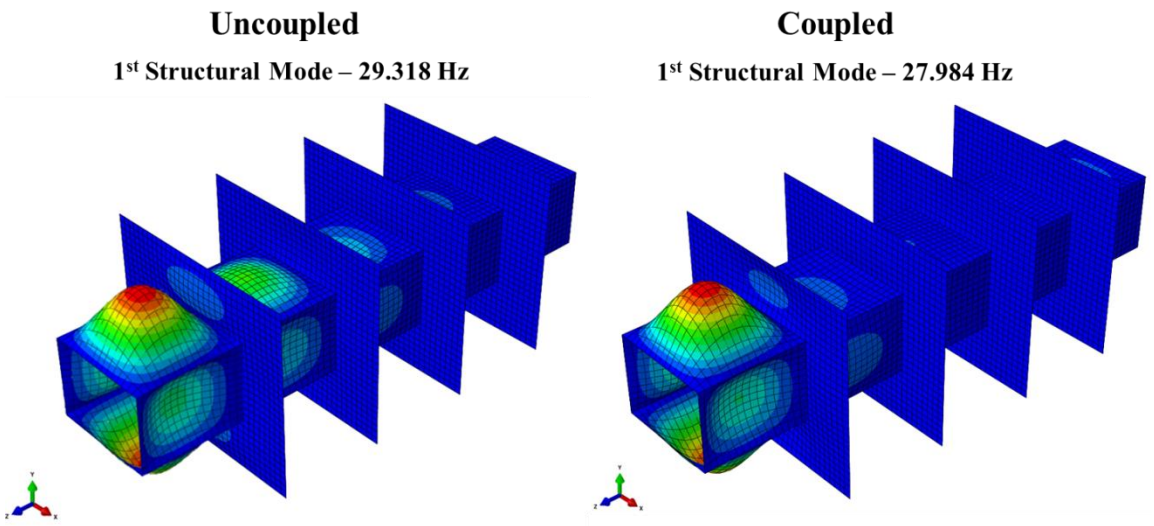

Figure 18: Second mode shapes

The 2nd mode is a structural mode for both the uncoupled and coupled case. Although the still frame of the mode shape shows that the two models have maximum deflections at the same location (last segment) in the opposite direction (max deflection inward for uncoupled and outward for coupled) the panels will oscillate and actually have almost the same mode shape. There is a slightly larger deflection in the 4th segment (between the 3rd and 4th substructures) on the uncoupled case, but overall there is not enough of a difference to warrant the need for a coupled analysis.

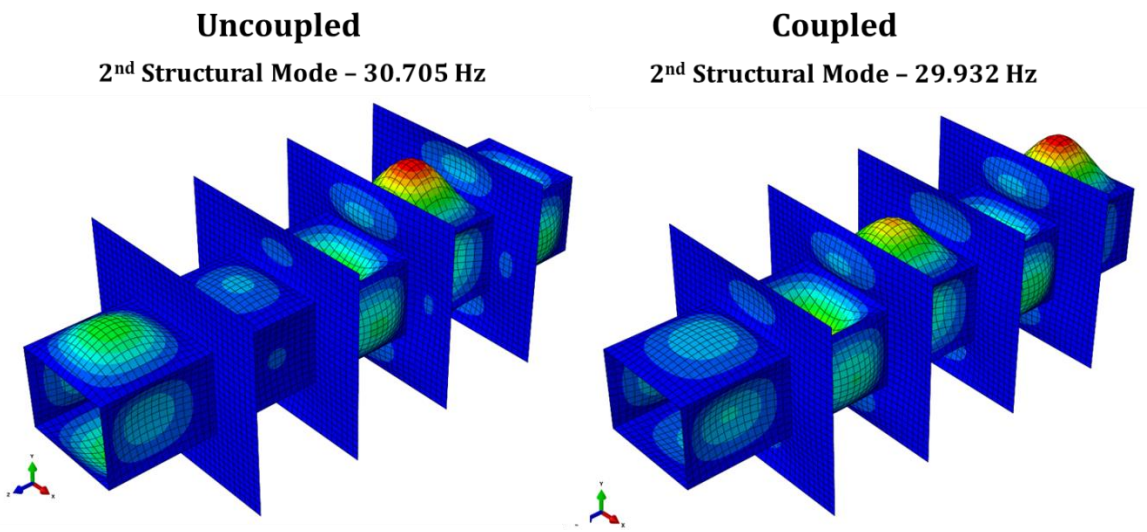

Figure 19: Third mode shapes

It is not until the 3rd mode (2nd structural mode) where we can begin to observe a major difference between the two mode shapes. In Figure 19, the maximum deflection on the uncoupled model is observed to be in the top and bottom panels of the 2nd segment (between the 1st and 2nd substructures). However, the coupled analysis shows that the maximum deflection occurs in the first segment. Although the difference in frequency between the uncoupled and coupled modes is small, the maximum displacement in the structure is not observed to be in the same location. This tendency maximum deflections varying between the uncoupled and coupled mode shapes continues with the 4th and 5th modes shown in Figures 20 and 21.

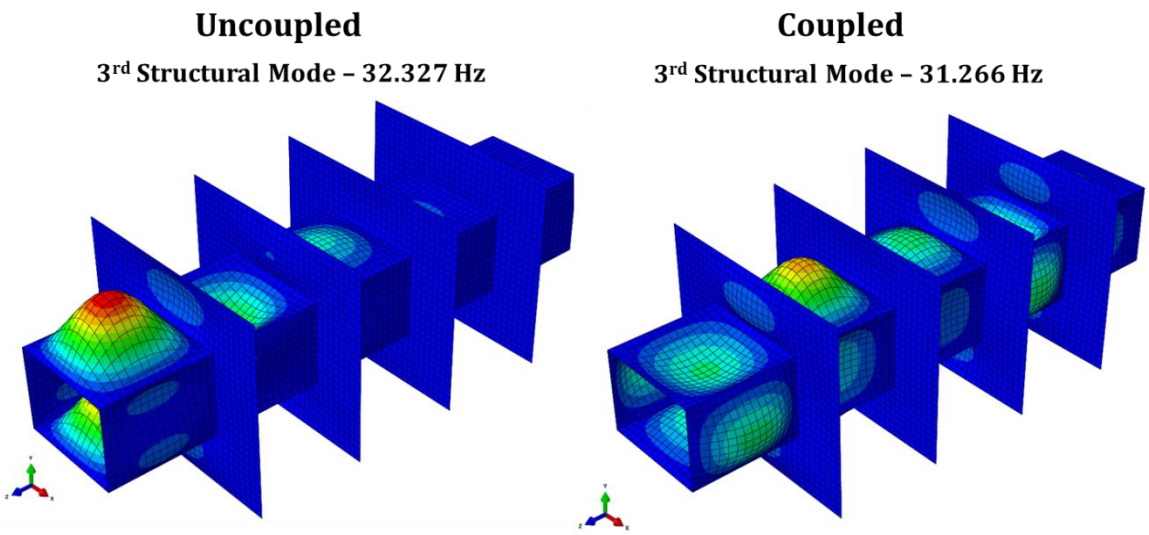

Figure 20: Fourth mode shapes

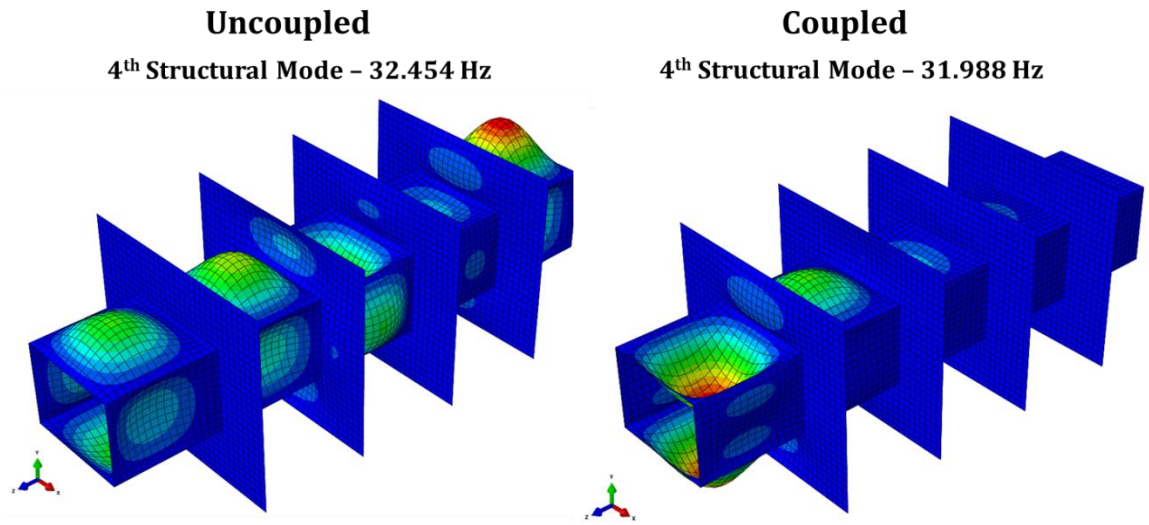

Figure 21: Fifth mode shapes

The 4th mode (3rd structural mode) again shows a slight difference between the mode shapes. The 5th mode (4th structural mode), however, shows a complete difference in the location of maximum deflection. In the uncoupled analysis the maximum deflection is observed in the first segment, whereas the coupled analysis shows the largest deflection in the last segment. These resulting differences in mode shapes along with

the slight difference in frequency at which it occurs, indicates that the coupling effect of air does contribute to the mode shapes of the structure, and in the case with mode 5, have a significant impact on the effect of the response.

The small difference in frequency between the uncoupled and coupled models is also significant when studying the frequency response function. Shown below is the frequency response function of the coupled model. For this particular response, the structure thickness is 5 mm, the dynamic distributed loading pressure was assigned an amplitude of 1500 Pa, the sensing location is on the top left corner 12.5 mm away from the end of the duct, and the system damping that is applied is 0.4% through all modes. Here the parameters are not of significant importance, like in the following sections, because the message of this plot is to show how approximating a model with the uncoupled response could potentially be inaccurate.

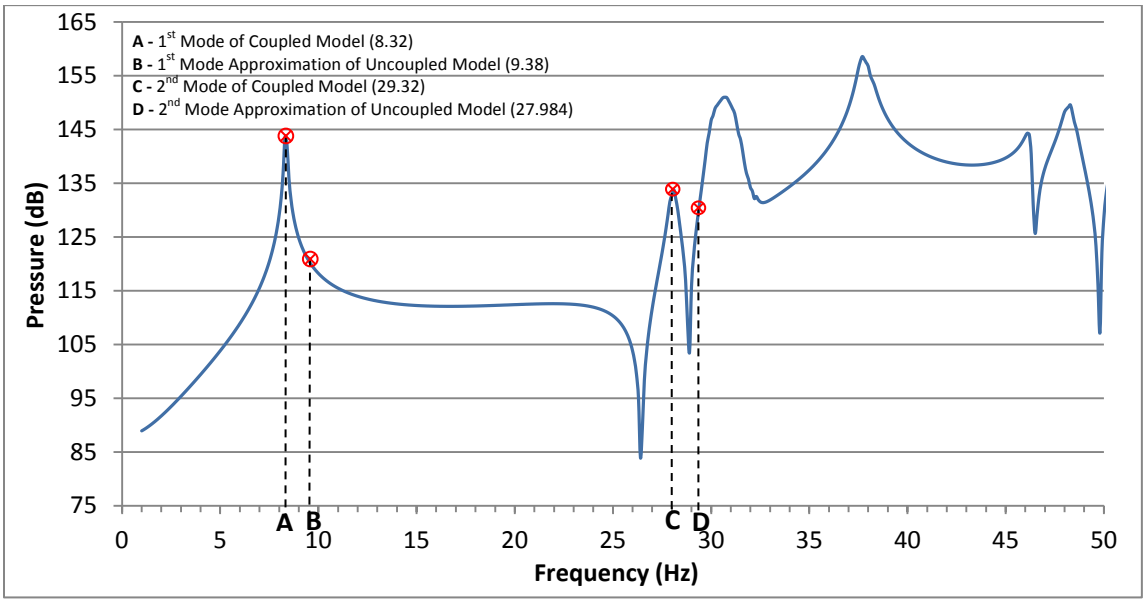

Figure 22: Frequency response function of the coupled duct model

Figure 22 shows the frequency response function of the coupled model (representing the true model in this case) with a frequency range of 0-50 Hz for better visual purposes. The first mode, shown in Figure 17, is denoted in this plot by “A”. At this frequency (8.32 Hz) a local peak pressure of approximately 144 dB is found. If the uncoupled model is used, the first resonating peak of the true response would be missed by only 1.06 Hz. Although 1.06 Hz may seem to be a very small difference, it is shown to be otherwise in the plot above. At the frequency of 9.38 Hz (frequency of the first uncoupled mode), the pressure is now approximately 122 dB, which is a difference of 22 dB to the coupled analysis. This difference is even more significant in higher ranges of SPL, as discussed in Section 3.11. The pressure difference between the second coupled mode and the approximation of this mode using the uncoupled model proves to be much smaller. However, as seen in Figure 22, this is only a coincidence because the frequency at “D” corresponds to a pressure on a totally different peak resonance than “C”. Therefore, in all models containing a fluid, an analysis of the coupling effects should be completed before assuming that the uncoupled model will be sufficient. In cases where less interaction occurs between the fluid and structural domain, the difference in “actual” pressure and the approximation of this pressure would be much smaller than the differences observed in this analysis. Once it was determined that the fluid did have an effect on this particular model’s response, the coupled system was used for further investigations [58].

4.4. Influence of Acoustic Infinite Elements

Another important aspect of acoustic modeling is the ability to capture the phenomena occurring in an actual environment with a finite element model. Many interior acoustic problems are already difficult to represent, but combining an exterior acoustic domain creates an even larger challenge. Acoustic fields are strongly dependent on the conditions at the boundary of the acoustic medium. Using Abaqus, problems in unbounded domains can be approximately solved by using impedance boundary conditions and infinite elements as discussed in Section 3.9. One class of infinite boundary treatment available in Abaqus is the impedance boundary, which acts as a non-reflecting boundary condition. To be used effectively, the default radiating condition must be relatively far away from the acoustic source. Another type of treatment for unbounded problems is acoustic infinite elements. These types of elements can be directly applied to the structure, which eliminates meshing of the exterior acoustic domain. To test which boundary treatment would be best for the embedded duct model, three scenarios were explored: no treatment (only finite air elements at boundary), impedance boundary condition, and acoustic infinite elements. For this comparison, the following figure showing the load and location of measurement was used. Here, the front of the structure is excited by a uniformly distributed pressure of 1500 Pa as shown in Figure 23.

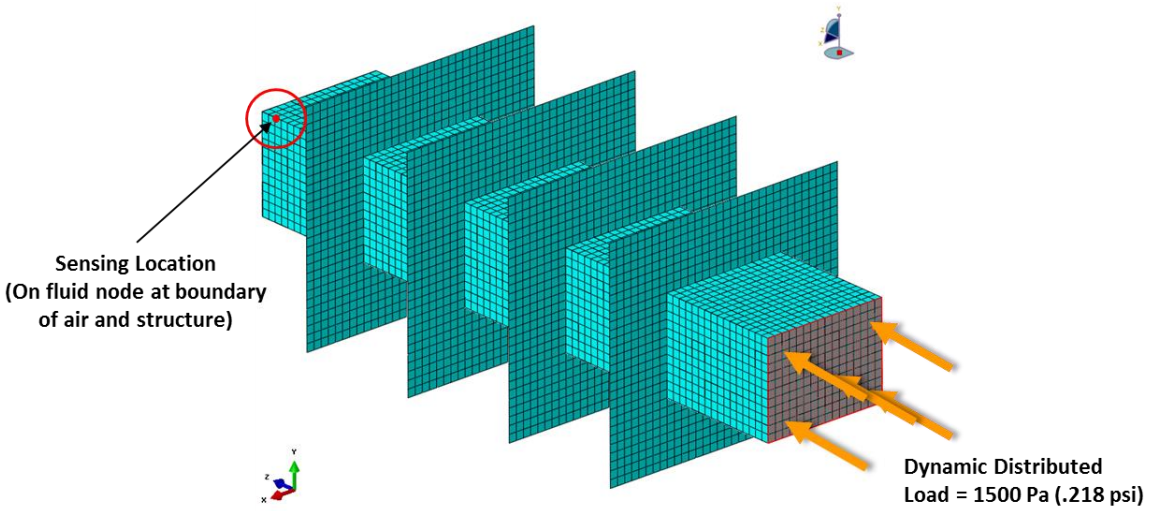

Figure 23: Loading applied to front of duct

For this analysis the duct walls and substructure were 5 mm thick, which represents an approximate thickness for actual embedded exhaust-washed applications, and the sensing location for the response was selected to be at a fluid node in the upper left corner, 12.5 mm from the end of the duct as shown above. The region was selected due to the intense pressures and modal deflections that the system experiences near the outlet of the duct. By using a steady-state dynamic analysis in Abaqus, the model with infinite elements could be compared with the model having an impedance boundary condition. This analysis type is able to bias the excitation frequencies toward the values that generate a response peak. In order to accurately capture the peak acoustic pressures, even with the structural damping applied to the model, a frequency step size of 0.1 Hz is used on all frequency response functions in the proceeding plots. The frequency step size, which was previously investigated in convergence studies, proved to be most suitable for the current model and frequency ranges explored. Using

this solution method, the frequency response functions for the three scenarios were obtained as shown in Figure 24.

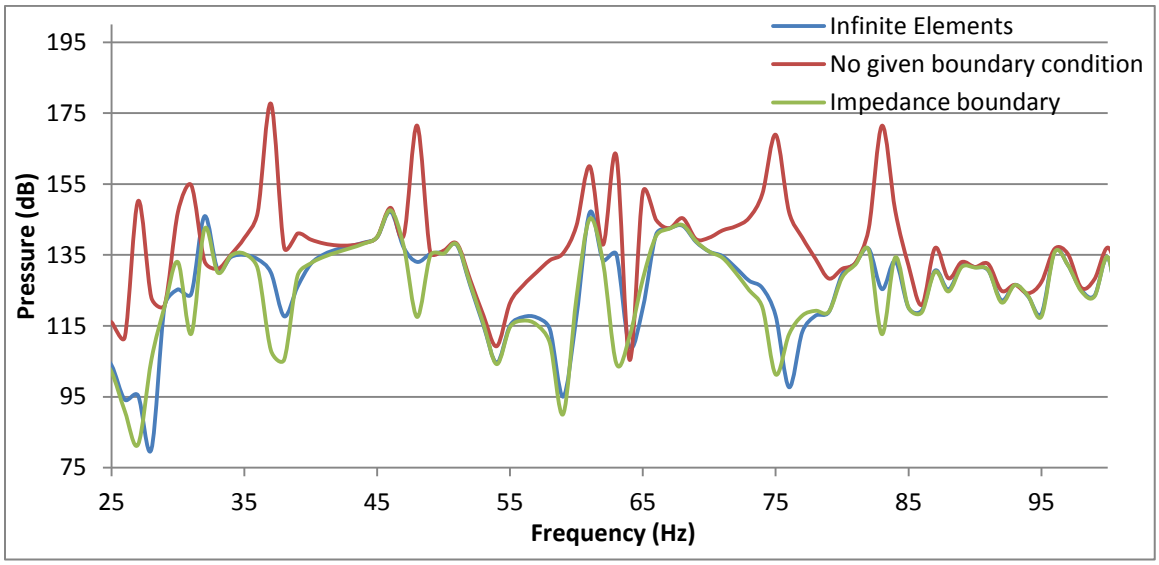

Figure 24: Frequency response functions with varying boundary conditions

From the figure above, one can clearly see that not applying a boundary condition to the model drastically alters the response of the system. Here the impedance boundary and infinite elements that account for the unbounded domain produce similar responses, but the model without the boundary condition has resonating pressure peaks of a much larger magnitude. Through this analysis it was determined that the unbounded domain must be taken into account for acoustic FEA. In Abaqus, a finite acoustic element boundary that is not coupled to another type of element or boundary condition (structure, infinite elements/impedance boundary, etc.) will automatically default that boundary to a fixed, rigid boundary condition (which approximates a normal pressure gradient of zero at the boundary). Therefore the acoustic energy does not leave the mesh, and instead is reflected back into the mesh from the boundary. If structural

elements are coupled to the finite acoustic element surface, they will generate flow into the fluid and affect the pressure. The absorber elements or infinite elements create a condition where the propagating acoustic waves do not reflect off the boundary, creating a more realistic representation of the open end of the exhaust system.

Once it was determined that a boundary condition or infinite elements must be applied to more accurately capture the response of an embedded exhaust duct, the next step is deciding which of these conditions to use going forward. From the above plot, the maximum pressures and associated frequencies were extracted and shown below.

Table 5: Maximum pressure results

	Maximum Pressure (dB)	**Frequency (Hz)**
No Boundary	177.7	37.0
Infinite Elements	147.3	46.0
Impedance Boundary	147.6	46.0

Just looking at the maximum pressures, the infinite elements and impedance boundary conditions produce almost identical results. Here the non-reflecting boundary condition (defined using impedance) is an approximation for acoustic waves that are transmitted across the boundary with a small amount of reflection. The equation for impedance is shown in Eq. (52). Abaqus internally calculates the correct impedance parameters to approximate the non-reflecting boundary. However, the default radiating boundary conditions must be relatively far away from the acoustic sources to be accurate for general problems [56]. This creates the need for an external finite acoustic mesh shown in Figure 4, which can significantly add to the computational cost of the analysis. Acoustic infinite elements have surface topology similar to that of structural infinite

elements, and can be defined on the terminating region of the acoustic finite elements of the model. Since these elements are more accurate than the non-reflecting boundaries due to the ninth-order approximation they use, and because impedance boundary conditions cannot be used in modal analysis in Abaqus, the infinite elements approach was selected to model the outlet of the system. In reality, not all of the acoustic waves would exit the embedded exhaust system due to impedance mismatching at this interface, however, most of the acoustic pressure does leave the system which justifies the future use of the acoustic infinite elements going forward.

4.5. Parametric Study of Varying Thickness in Structural-Acoustic Coupled Environment

The next investigation, and main focus of this chapter, was to explore how adding structural material to the system affects the acoustic pressure in the fluid at a location along the duct. This is accomplished by conducting a parametric study at some nodal location by again running a steady-state dynamic analysis on the duct system. All of the parameters associated with the analysis in Section 4.4 are the same for this particular analysis. The only difference is that infinite elements were chosen to represent the open end of the duct and the frequency range of interest was expanded to 0-300 Hz. In this parametric study, thickness values of all the structural components (both duct and substructure) vary from 1 mm to 10 mm. The front plate receiving the pressure loading is assigned a thickness of 5 mm, and this thickness remains the same throughout all of

the parametric case studies, so that the initial loading remains constant. The frequency plots obtained contain complicated response functions that are difficult to quantify and compare against one another, as shown in Figure 25 where several responses for varying thicknesses are shown.

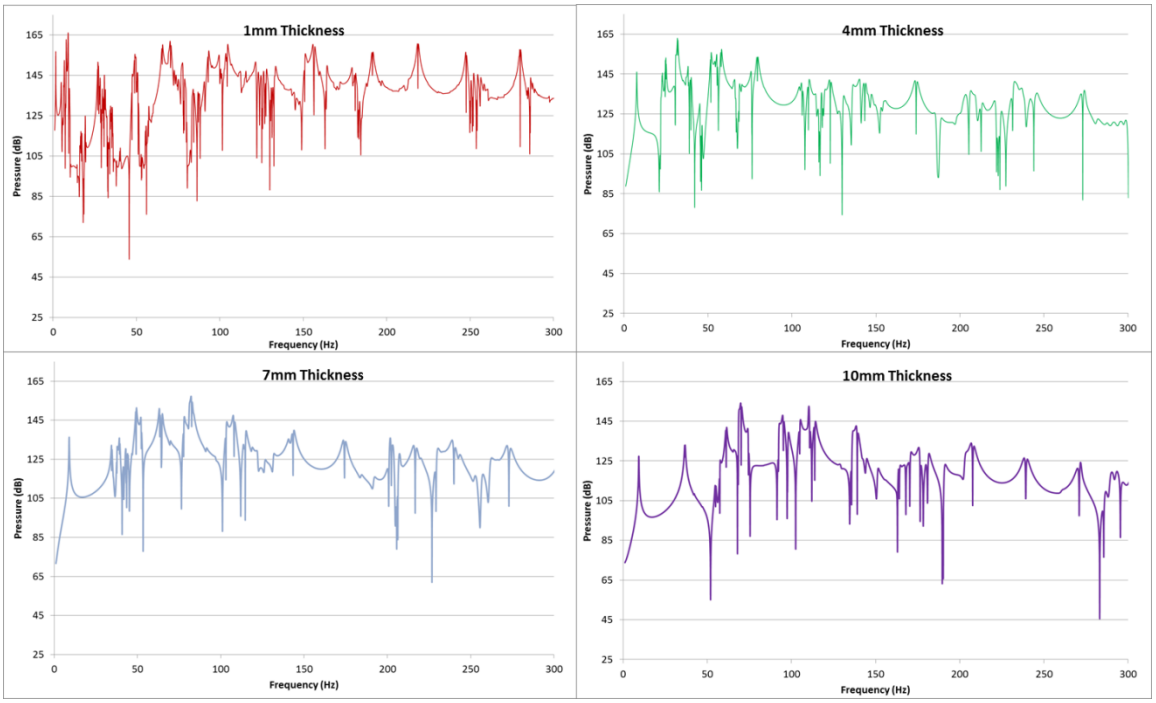

Figure 25: Frequency response function plots

For this reason, the peak pressures in the curves are selected and an envelope of these peak pressures is taken, creating trendlines of the maximum resulting pressures from each thickness. This procedure is highlighted in Figure 26, where the structural thickness value used was 5 mm.

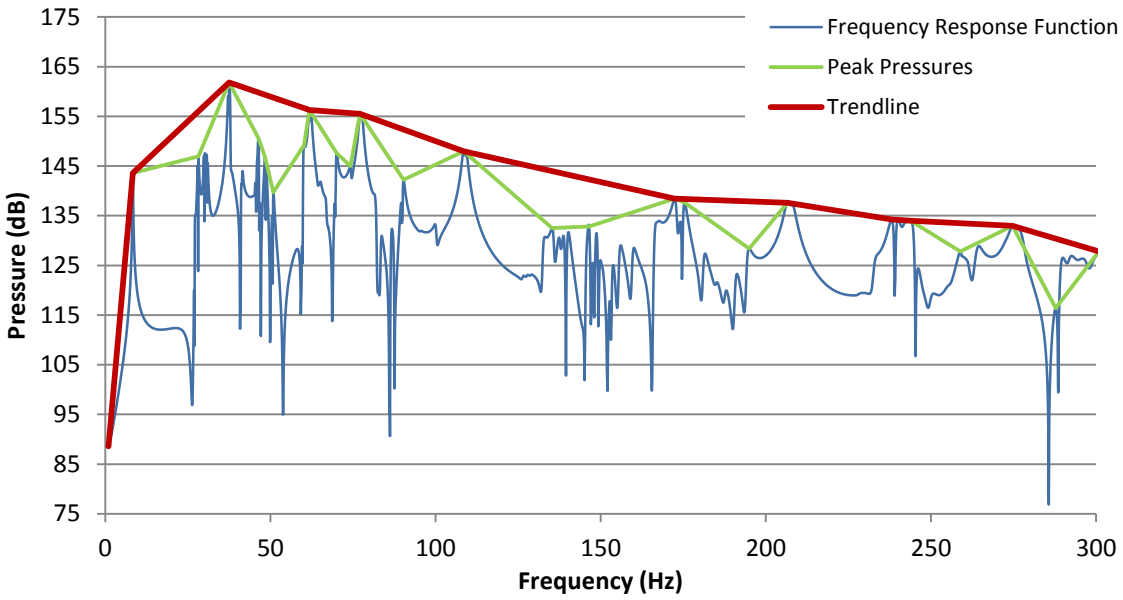

Figure 26: Envelope of frequency response function for 5 mm thickness

Taking envelopes of the frequency response functions in this way allows a better comparison of multiple responses on the same plot. Using this strategy the following figure was obtained.

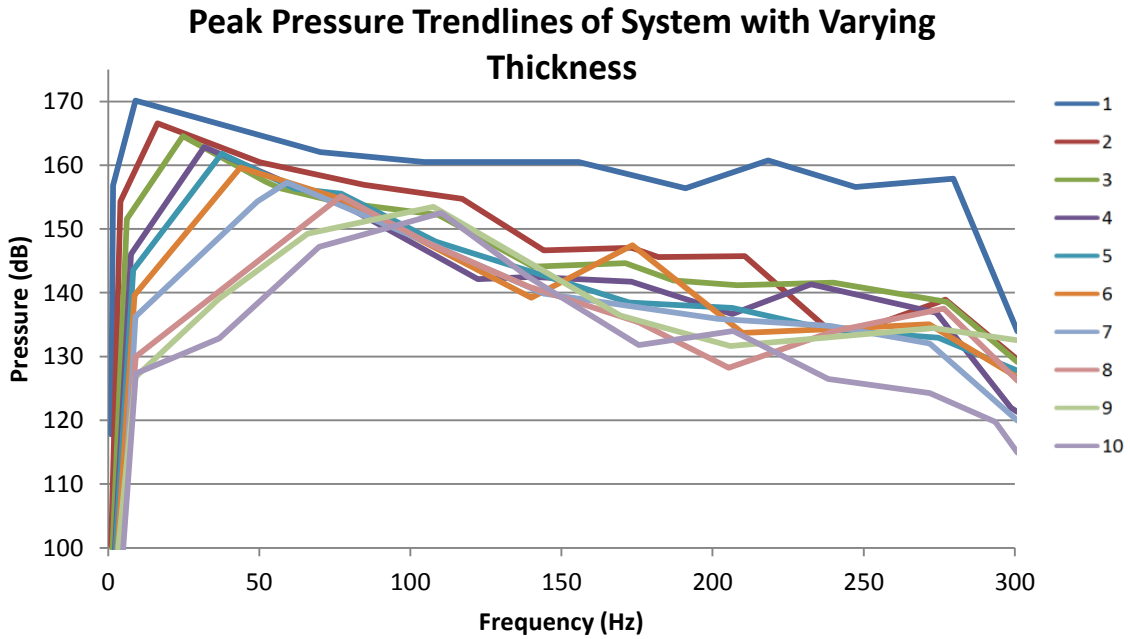

Figure 27: Trendlines of frequency response functions

From these results, one can see that by adding thickness to the duct and substructure, the maximum pressure in the system can be reduced. Adding more thickness to the structural walls also increases the mass and stiffness of the coupled matrix, which causes the system to stiffen explaining the upward shift in natural frequencies. The maximum pressure and associated frequency of the various responses are shown in the table below:

Table 6: Maximum pressure results

Model Thickness (mm)	Max Pressure (dB)	Frequency (Hz)
1.0	170.1	9.0
2.0	166.6	16.4
3.0	164.5	24.7
4.0	162.9	31.8
5.0	161.8	37.5
6.0	159.6	43.8
7.0	157.3	59.2
8.0	155.1	77.0
9.0	153.5	107.6
10.0	152.5	110.3

This table shows that as the thickness increases, the frequency of the maximum pressure shifts upwards. The difference in frequency between peak pressures of the 1 mm and 10 mm thicknesses is almost 100 hertz, and the pressure difference between these two thicknesses is nearly 20 decibels. Clearly the material thickness in an acoustic environment alters the pressure found within the fluid domain. A reduction of 20 dB would have an immense effect of prolonging the fatigue life of the embedded jet engine components. This effect is due to the fact that as the thickness of the structure and

substructure changes, the mass and stiffness matrices of the system's structural equation of motion also changes. So if the thickness increases, values in the mass and stiffness matrices also increase, creating a reduction in pressure at the fluid structure interface in the coupled matrix equation. Although the additional thickness reduces the pressure within the duct, increasing the thickness adds additional weight to the system. This is clearly a disadvantage for new air vehicle design, so the duct sections that are altered must be limited to critical areas that are more susceptible to the intense acoustic loading. The information on the frequency of the maximum pressure is also significant to design, especially if a fixture for the duct were to be created in order to dampen out the maximum pressure in the system.

However, the results from this study are misleading, because the frequency response function was plotted for only one node that was located 12.5 mm from the duct exit in the top-left corner. The above results for this particular node are accurate, but this tendency does not define the frequency output of the entire system. To further study the effects, the frequency response functions were evaluated at a different nodal region for comparison as shown in the following figure.

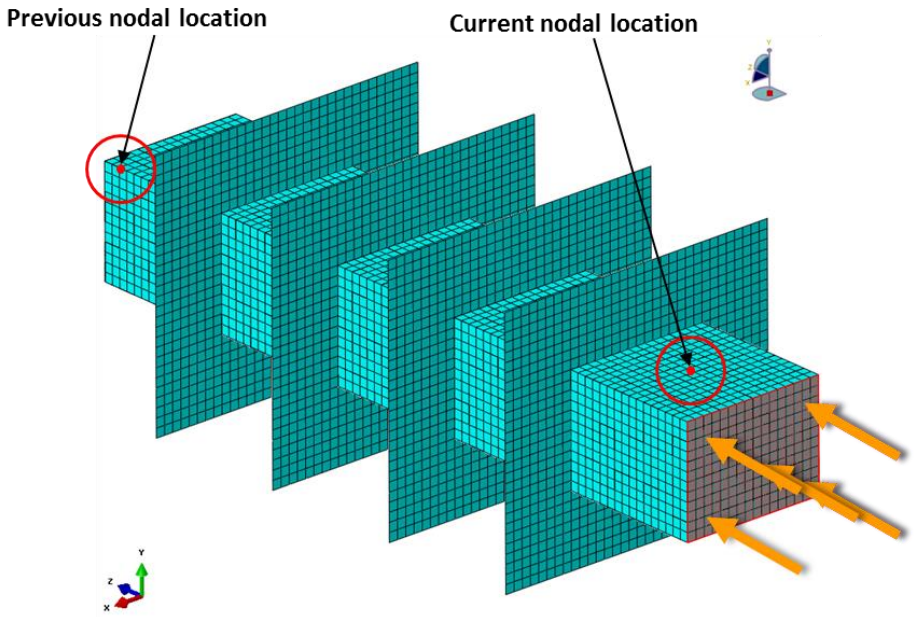

Figure 28: Varying nodal regions on duct

In a similar manner, the frequency responses were plotted and envelopes of the peaks pressures were obtained as shown in the Figure 29.

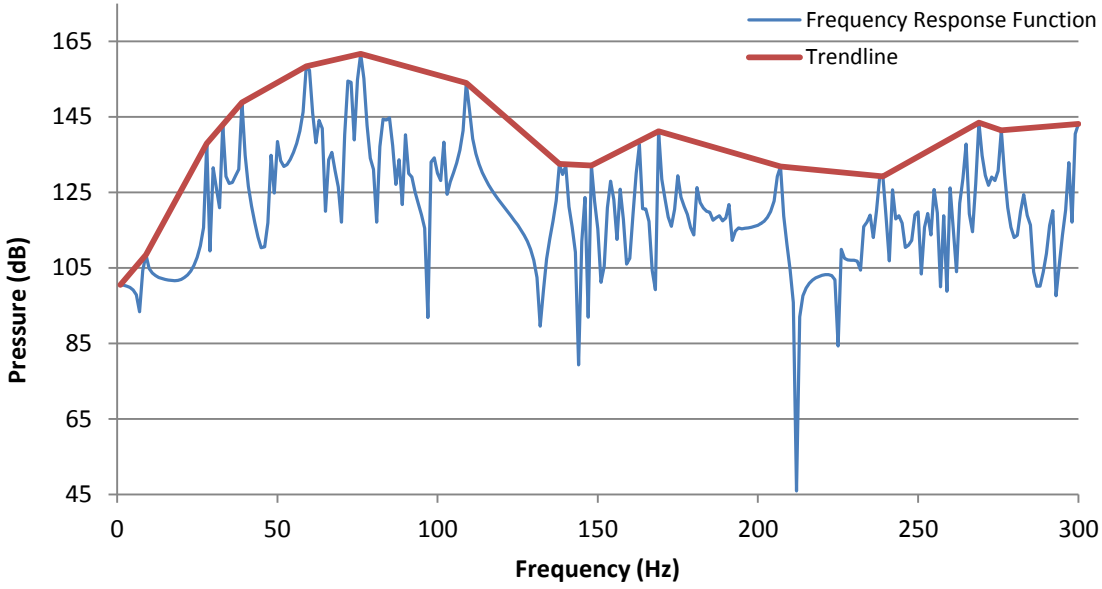

Figure 29: Envelope of frequency response function for 5 mm thickness

So in this way, the envelopes of the frequency response function can be plotted on the same graph for comparison purposes.

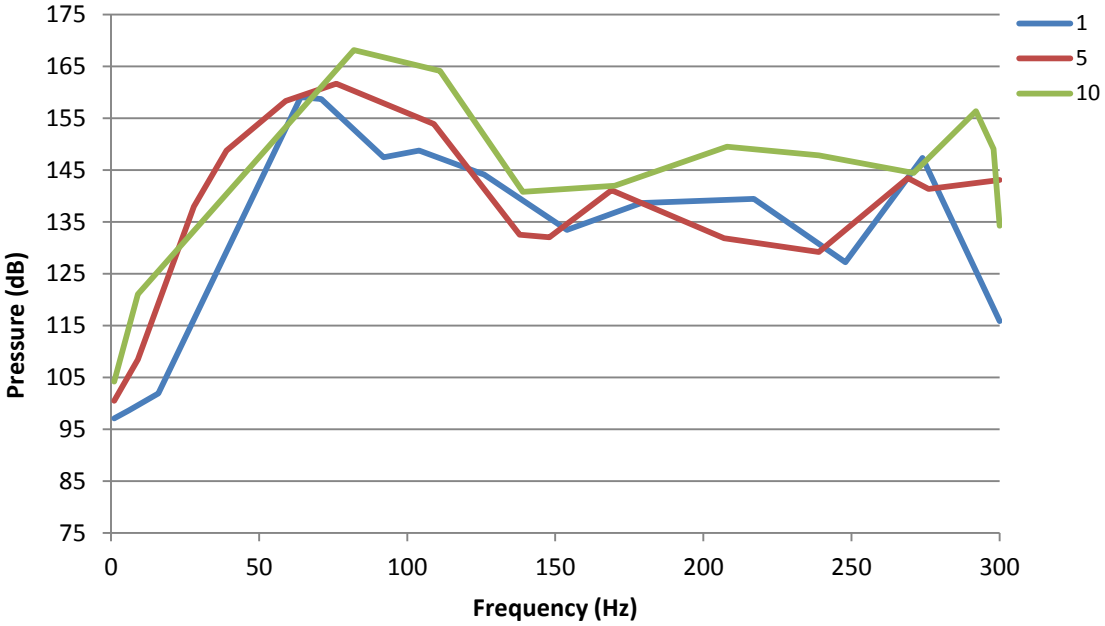

Figure 30: Trendlines of frequency response functions

Table 7: Maximum pressure results

Model Thickness (mm)	Max Pressure (dB)	Frequency (Hz)
1.0	159.1	64.2
5.0	161.7	76.5
10.0	168.2	81.7

The study at the varying nodal location actually showed the reverse effect of the previous study, that increasing model thickness caused an increase in maximum pressure. This prescription is very problematic for our structural-acoustic model. Re-designing the structure to minimize acoustic pressure at only one node can result in the acoustic pressure to significantly increase at another node. For this reason, by optimizing the thickness design variables for minimum acoustic pressure at all nodes of

the model (subject to stress and mass constraints), we can exploit the conflicting behavior of this design effect. We can also ensure that the overall pressure seen in the model is actually decreasing instead of only decreasing in one location (which could result in a pressure spike at another location).

This research concluded that that fluid and structural damping properties, as well as the compliability of the panel, promotes damping of the acoustic pressure and related stress in the frequency response function of the system. This effect is apparent in nodal locations where the structure can more easily expand/contract, and is less evident in more rigid locations near supports or boundary conditions. This issue means that not only is the problem dependent on the excitation frequency, but it is also spatially dependent. The conflicting acoustic effects at differing nodal regions add more complexity to this already challenging dynamic coupled problem. Re-designing the structure to minimize acoustic loading effects at one nodal region can result in the acoustic related stress to significantly increase at another region. This introduces the need for optimization in this vibro-acoustic problem, where the correct optimization schemes can exploit the controversial behavior of this acoustic design effect. Utilizing optimization, the mass of the system can be minimized while constraining the stress magnitudes at all critical locations in the system.

5. Structural-Acoustic Optimization

5.1. Design Goal

On a low observable aircraft, the embedded engine exhaust ducts have been meticulously designed and tested for exact specifications. For this reason, much of the geometry, area, and location of the exhaust ducted path itself is fixed and unlikely to drastically change. However, the subspace areas located between the exhaust duct and the aircraft skins, which contain the substructure supports, do not influence the exhaust flow and could be reinforced or redesigned. It has been proven in the previous chapter that the thickness of these members influence the acoustic pressure distribution throughout the exhaust duct system. Therefore, this effect can be exploited through an optimization process as conceptually shown in Figure 31.

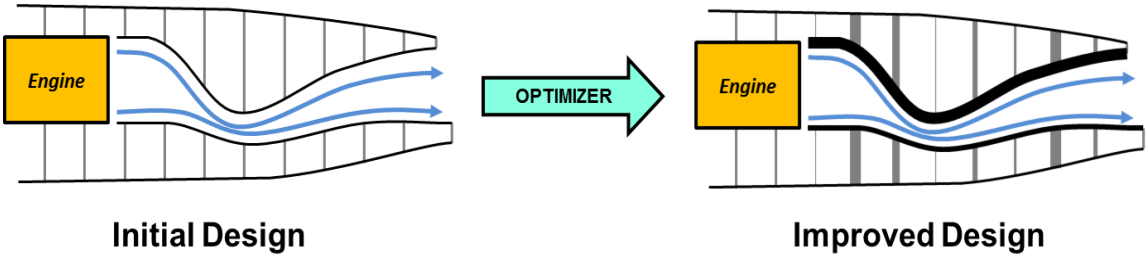

Figure 31: Conceptual thickness optimization

Using this thickness optimization ideology, the initial or baseline design will change through the process and determine where more material should be added or removed.

In this way, the system's structural thicknesses will simultaneously change to reduce the acoustic related stress throughout the entire model (not one nodal location) while minimizing mass, therefore improving the structure.

5.2. Objective Function and Constraints

For this analysis, the objective function is to minimize weight of the structure subject to constraints on the structural elements' stress values. Utilizing this methodology allows the optimization statement to not only account for the acoustic pressure acting on the structure (as in Section 4.5), but also the mechanical vibrations that travel through the duct walls [59]. However, because this problem is dynamic and coupled, the stress constraints depend not only on space but frequency as well. Another issue that stress constraints cause in this complex structural-acoustic problem is that the optimization method selected is computationally affected by the total number constraints used. After mesh convergence, the current model of the exhaust system requires approximately 7500 structural elements, which translates to 7500 element stress constraints that must be placed on the finite element model in order to monitor the entire system. However, not every single element stress constraint is needed in the model because the stress gradient between adjoining elements is not extremely significant as long as the mesh size is refined well enough.

For instance, a plate with fixed boundary conditions along the edges (Figure 32) and a distributed pressure load across the entire top surface will typically have two critical regions for redesign.

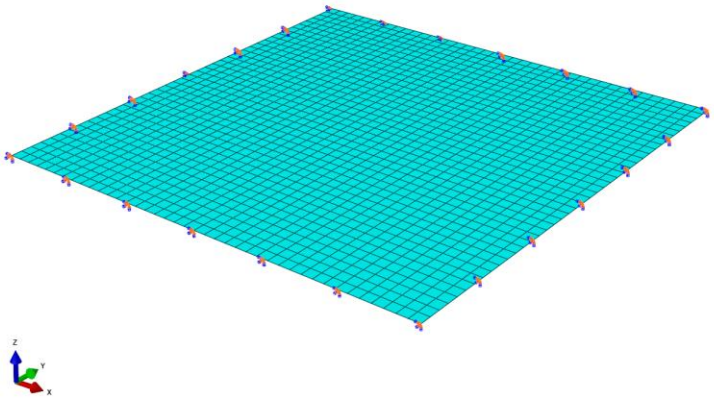

Figure 32: Plate FE model

One location is in the center of the plate, which experiences the largest deflection due to that mode being most easily excited. The second is at the elements located on the edges next to the boundary conditions. These areas will experience the largest amounts of stress. The analysis for displacement and stress in this model at the first mode can be seen in Figure 33.

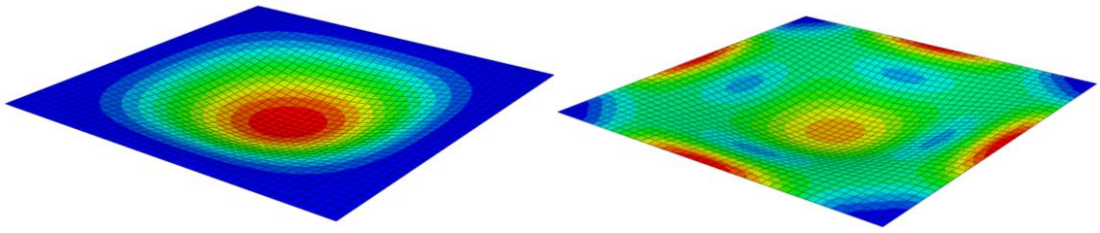

Figure 33: FEA on plate: displacement (left) and von Mises stress (right)

The elements in between these two regions are important, but do not necessarily have to be monitored as closely as the elements in the center and around the outside of the

plate, specifically the middle and corners. Using this ideology, a critical point constraints technique can be utilized in the embedded exhaust system, where only the elements receiving the most modal participation and largest stress contributions are monitored under the constraints.

Utilizing this critical point constraint technique, will not only account for the stress dependence on the frequency and spatial regions, but significantly reduce the number of constraints used in the problem formulation saving computational time in the optimization stage. For this particular problem, the critical point constraints were applied to the elements highlighted in Figure 34.

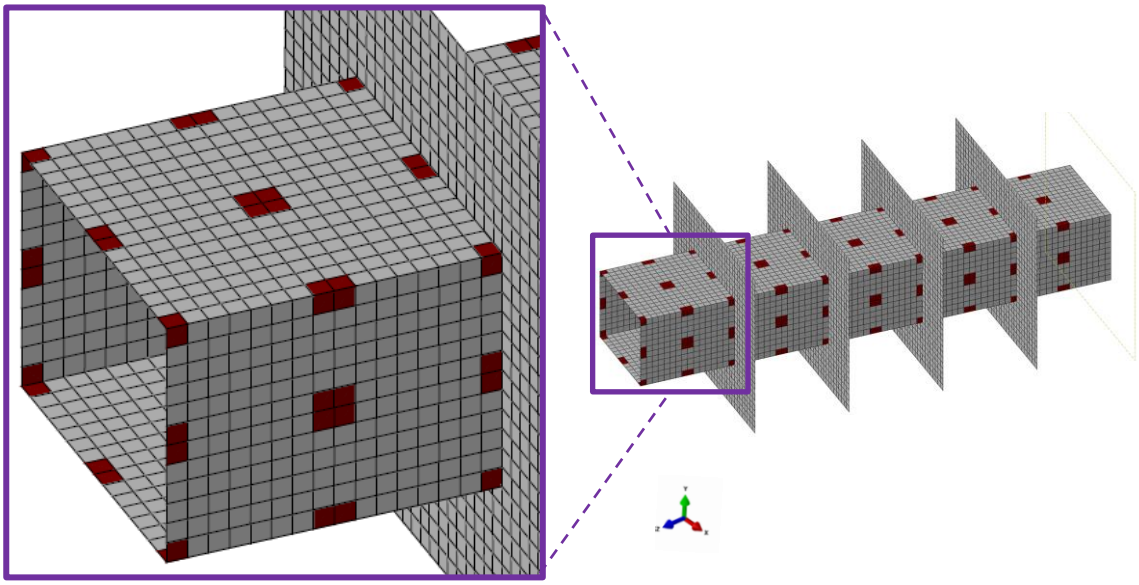

Figure 34: Critical Point Constraint Regions

Note that this pattern of elements with stress constraints is applied to all segments of the structure, not just the last segment, which was enlarged in Figure 34 for visual purposes. The stresses in the substructures are not monitored in this analysis, because

the elemental stress is very dependent on the boundary conditions. Since only simply supported boundary conditions are used as an approximation, the stresses that result from these conditions on the substructural panels will be inaccurate. The same stress spikes will be seen at the front of the structure near the approximated load. Since realistically there will be no plate at the front of the exhaust duct, the stress that arise are unreliable. However, the stresses obtained from the duct itself, away from the substructural edge boundary conditions and front loading of the system, will be more realistic to the actual stress response. The process of using the critical point constraints technique in the optimization process resulted in a stress evaluation that captured all of the largest stresses that were seen in the fully constrained model. In addition, utilizing the critical point constraints technique resulted in a computational cost reduction during the optimization process from 33.96 minutes to 16.37 minutes per data point acquisition (on a i7 core computer with a 3.40 GHz processor) which results in a reduction of approximately half (51.8%).

As systems experience higher excitation frequencies, the element regions used in the critical point constraints technique for this analysis will need to be expanded to account for the higher order mode shapes that can occur in the duct. For this reason, previous modal analyses must be executed to have a better understanding of the problem before a critical point constraints technique is utilized in the optimization process. From the numerous frequency response functions that were analyzed in this research, the maximum pressure peaks for this model are observed to occur anywhere from 9 Hz to 110 Hz as seen similarly in Table 6 from Chapter 4. Although the engine

associated with the embedded exhaust-washed structure will likely operate at much higher frequency ranges, this research is directed towards developing the tools to accomplish the structural-acoustic optimization of a system in a multidisciplinary loading environment. For this reason, the analysis will be constrained to a frequency range of 0-120 Hz. Most aerospace engine applications will operate at much higher frequencies than this frequency range, however, the goal of this work was to develop an optimization technique that could account for this spatially and frequency dependent problem. Therefore, a lower frequency range was selected for this work, but the tools developed in this research can be implemented on any frequency range of interest in the future.

5.3. Design Variables

The design variables in this optimization setup, like previously specified, are the structural thicknesses of the engine exhaust-washed structure. Each element of the duct and substructures could potentially be a thickness design variable, but this approach would be improbable to manufacture because of the cost associated with layering material in this fashion. Therefore, for this optimization problem, the design variables that were chosen are the thickness of the duct walls and the four separate substructures shown in Figure 35. By utilizing the model's symmetrical design, t1 and t2 were established for the horizontal and vertical walls of the duct respectively, therefore reducing the number of variables even further.

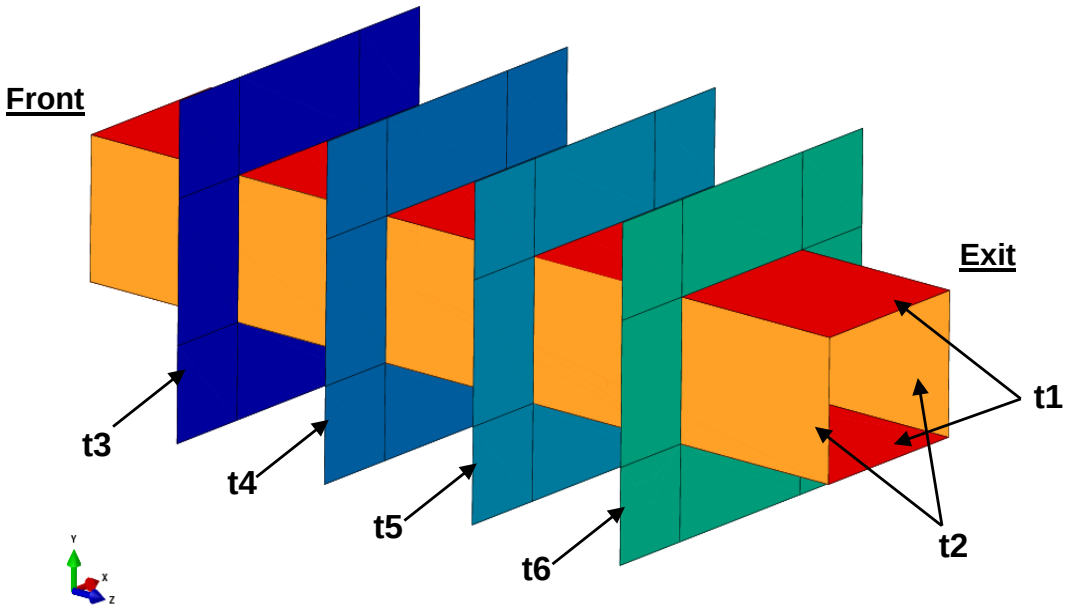

Figure 35: Design variables shown in different colors

5.4. Problem Statement

The optimization problem statement containing the objective function, constraint functions, and the side bounds on the design variables is shown below

$$\begin{aligned} \text{Minimize:} \quad & h(\boldsymbol{x}) = \textit{Total Mass} \\ \text{Subject to:} \quad & g_i(\boldsymbol{x}) = \sigma_{VM}(x,y,z) \leq 100\ \textit{MPa} \\ \text{Design Variables:} \quad & \boldsymbol{x}_i = [t_1, t_2, t_3, t_4, t_5, t_6] \\ \text{Side Bounds:} \quad & 1\ mm \leq x_i \leq 10\ mm \end{aligned} \tag{60}$$

Where $\boldsymbol{\sigma_{VM}}$ is the von Mises stress of the critical point constraint elements and t is the corresponding thickness for each design variable. The allowable stress constraint of 100 MPa was selected as the upper limit of the von Mises stress range, because this value results in a life cycle for the structure through a high cycle fatigue calculation (details of

which can be seen in Section 8.4). Note that these constraints are applied to every element considered using the critical point constraints technique. The design bounds for the variables were selected by using approximations on actual aluminum thickness values that could be potentially used. Although 1 mm and 10 mm are slightly on the extreme side regarding their thinness and thickness respectively, this allows for a good design space in which the optimization algorithms can find a solution.

5.5. Solution Procedure

The simultaneous thickness optimization procedure utilizing the critical point constraint technique that is implemented for solving the structural-acoustic system, accounts for the spatial dependency in the problem. However, this problem is also dynamic and frequency dependent, so along with the spatial dependency, it creates a problem that is multi-modal. Therefore, the solution space contains multiple minima making the results from an initial gradient-based optimization technique solely dependent on the initial variables. In order to account for this issue, a hybrid optimization technique can be utilized that combines two different optimizing schemes. The first method utilizes an adaptive global search technique from the optimization package developed by Red Cedar Technology [60]. Then the second method takes the results found from the global optimizer and applies gradient based functions, through an SQP method, to locally optimize the structure. In this way, the spatially and frequency dependent structural-acoustic problem can be effectively optimized still using the problem statement shown in Eq. (60).

5.6. Computing Sensitivities

The Abaqus FEA model is originally evaluated at the initial design point to obtain the function value. The FEA can be conducted again by taking a small variation in the design variable range in order to obtain the gradients by the forward finite difference method, which is shown in the general form below.

$$\frac{\partial g(\bar{x})}{\partial x} = \frac{g(\bar{x} + \Delta x) - g(\bar{x})}{\Delta x} + \vartheta(\Delta x) \tag{61}$$

These gradient approximations are then utilized in the sequential quadratic programming method of optimization that is initiated for finding a better design solution.

5.7. Optimization Approach

The optimization technique used in this research is a hybrid method combining global and a local optimization techniques. The first optimization method used is SHERPA (Systematic Hybrid Exploration that is Robust, Progressive, and Adaptive) developed by HEEDS (Hierarchical Evolutionary Engineering Design System) of Red Cedar Technology. HEEDS is an optimization package that automates the iterative design process and uses an adaptive search strategy to efficiently find optimized solutions [60]. In the SHERPA scheme, the algorithm uses the elements of multiple search techniques simultaneously (not sequentially) in a unique blended manner in attempts to take

advantages of the best attributes from each methods. In these optimization methods, each participating approach contains internal tuning parameters that are modified during the search according to the knowledge obtained from the design space. In this way, SHERPA learns about the design space and adapts in order to effectively search all types of design spaces. This type of optimization is especially beneficial for solving this dynamic and frequency dependent problem because the multi-modality of the design space causes difficulties for most gradient-based optimization algorithms. Once the SHERPA method is used to find an approximate global optimum for the design, these parameters are input into the sequential quadratic programming (SQP) optimization method. Using this technique, the SQP method utilizes gradient information from the problem and locally converges to an optimum solution. If this local optimization scheme was implemented without an initial global optimization procedure, the results would be solely dependent on the baseline design parameters and converge on whichever local maxima was nearest. Therefore, by utilizing the SHERPA algorithm, an approximation of the best design parameters is obtained, and then this design is refined and improved further using the gradient based SQP method.

5.8. Optimization Results

An initial study was evaluated at the baseline design (design variables all equal to 5.0 mm), which resulted in a system mass of 405 kg and a maximum stress value of 235.53 MPa, violating the established constraint. Therefore, the hybrid optimization process is

utilized to reduce this stress magnitude to satisfy the constraint. The plot shown in Figure 36 represents the mass objective function history of the global SHERPA analysis. The blue line on this plot corresponds to the best design progress during optimization. The plot shown in Figure 37 represents the stress constraint history of the analysis. In this plot, the blue line still corresponds to the best design progress during the optimization process, and the red line depicts the constraint value. From this objective plot history, one can observe how the SHERPA algorithm gathers data and adapts to the design space as the iteration process progresses. Since SHERPA contains random search, genetic algorithm, and various sampling methods that adapt to the problem as more data is obtained, the global process can find a region in the design space where an optimal solution exists. One characteristic of this optimization algorithm is that while the best design solution is approached via the blue line in Figure 36 and 37, the global technique persists to continually check the entire design space to make sure that an optimum design does exist in the region.

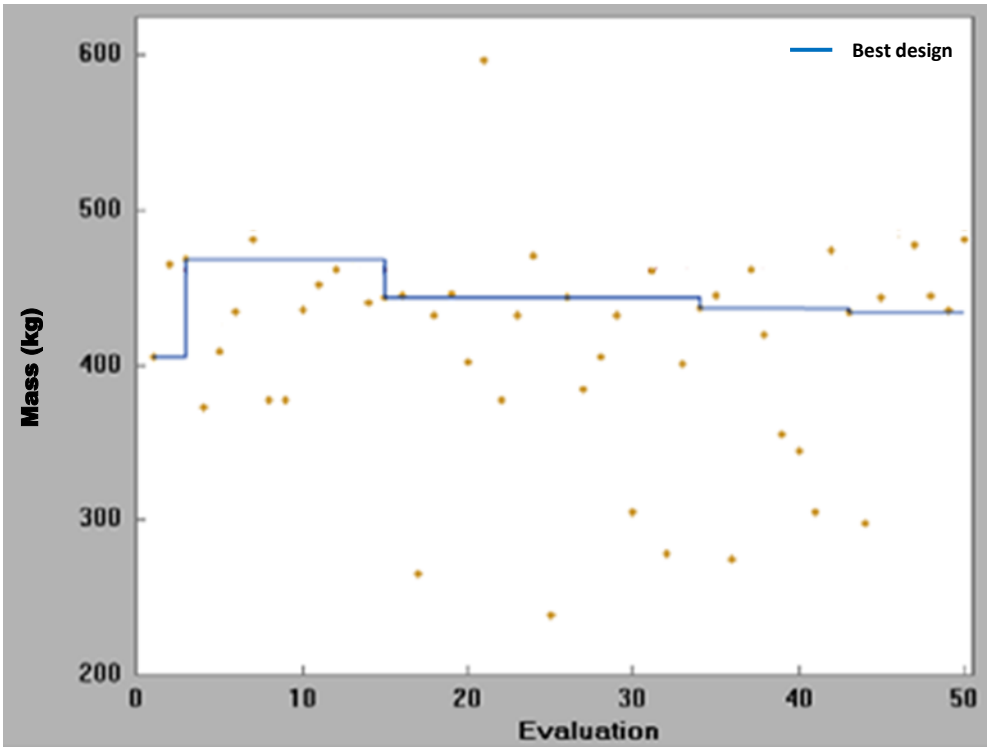

Figure 36: Objective function history

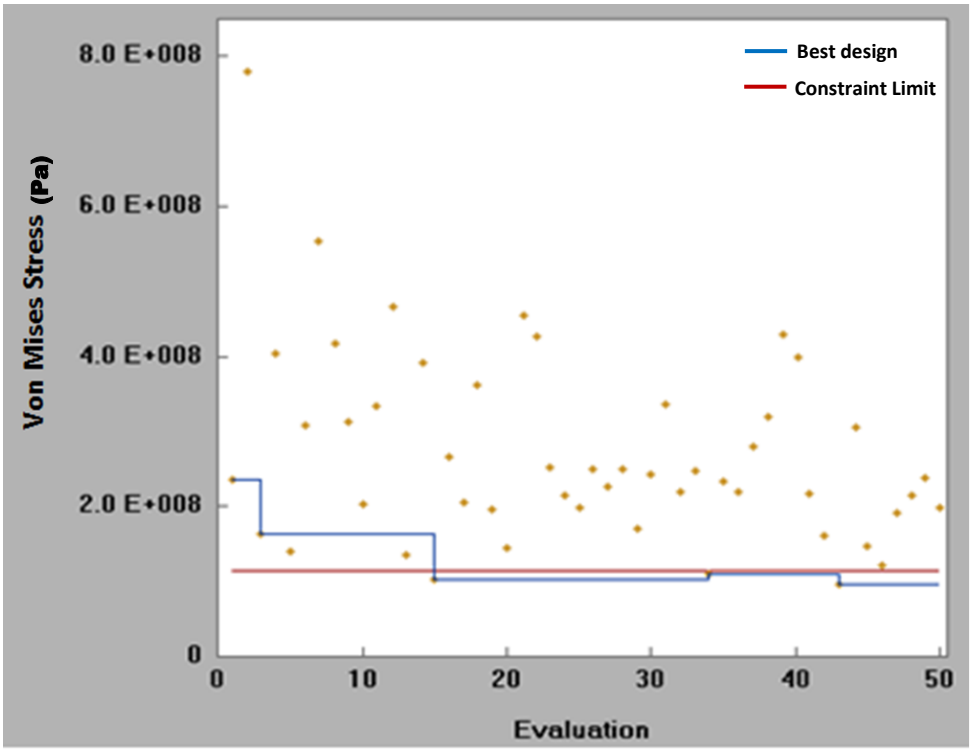

Figure 37: Constraint history

From this analysis, it can be observed that it took approximately 15 iterations to find a feasible solution that satisfied the stress constraint. The process continued to globally search for an optimum solution while minimizing weight through the remainder of the evaluations. Near the end of the evaluation process, an improved set of variables were found to minimize the weight and satisfy the stress constraints. Since all design variables for this problem are constrained within the same bounds, they can be shown on the same plot in Figure 38. Each colored "best design" line corresponds to the same colored thickness variable data point specified in the legend. In this way, one can observe how the design variables changed throughout the global design process.

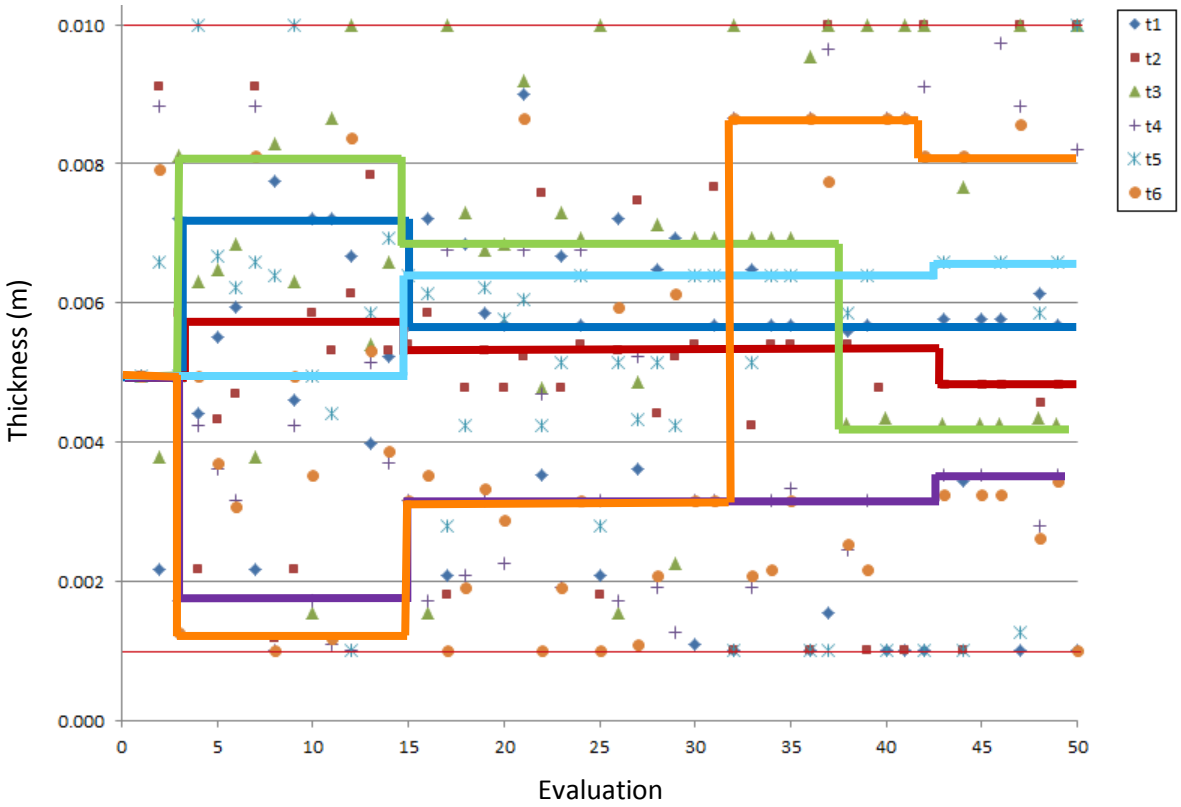

Figure 38: SHERPA "Best Design" variable history

Once the variables were approximated using the global optimization technique, these data points become the starting parameters for the SQP method in the local optimization stage. The objective function history (Figure 39) and the constraint history (Figure 40) show that the SQP optimization locally converges on a solution in a relatively small number of iterations.

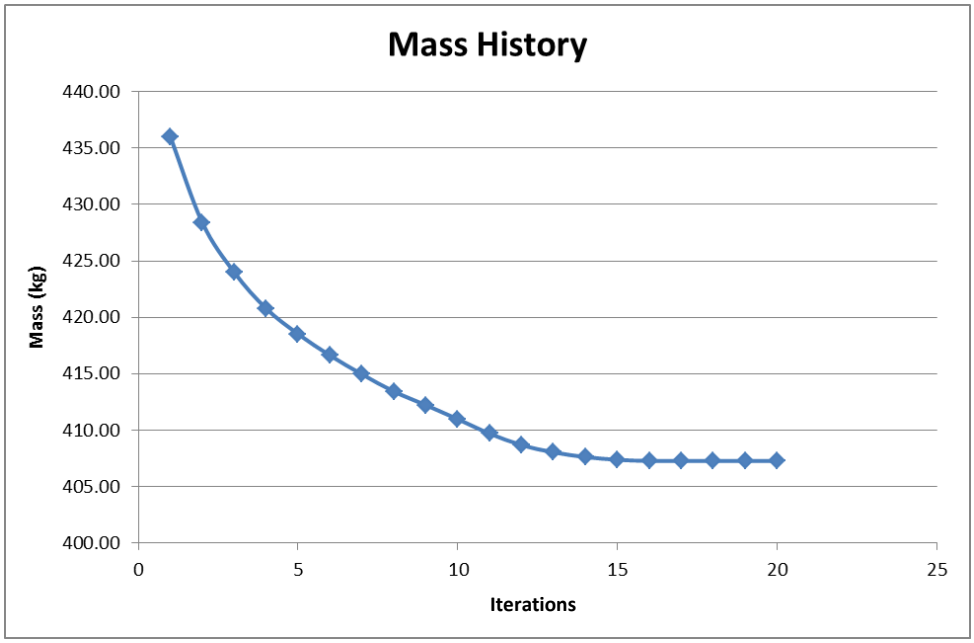

Figure 39: SQP objective function history

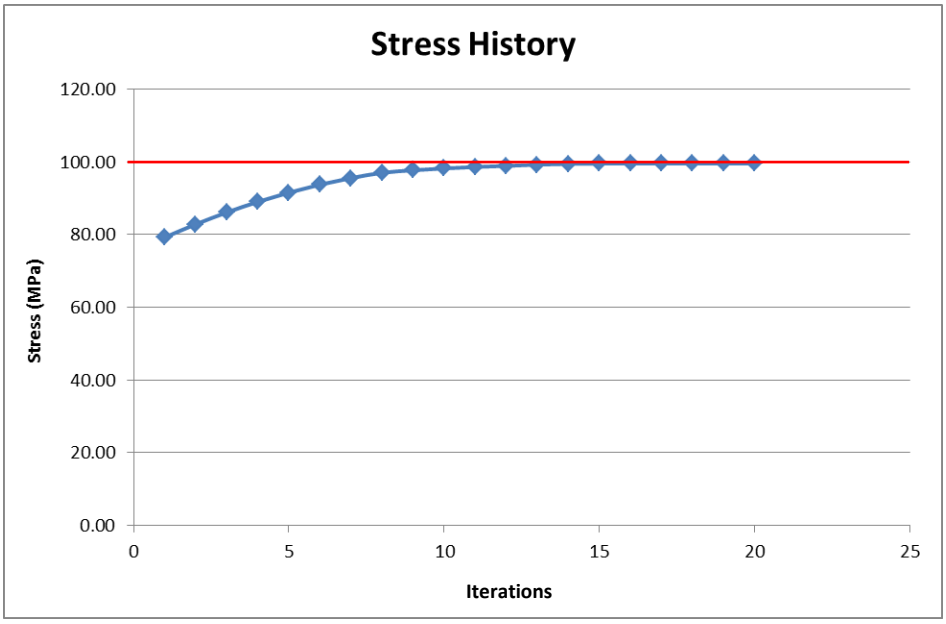

Figure 40: SQP constraint history

Similarly to Figure 38, the design variable histories for SQP can be shown in the same plot in Figure 41. Since a gradient based method is used instead of a global search method, the optimization results converge in a much more standard manner.

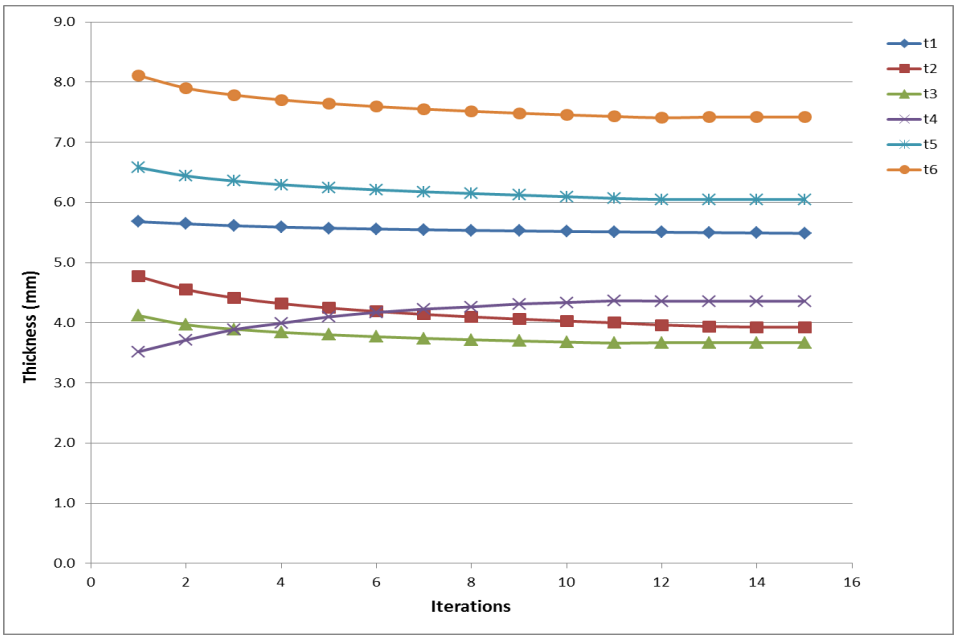

Figure 41: SQP thickness variable history

The results from using this hybrid optimization method can be seen in Table 8, along with the results from the baseline design and SHERPA method.

Table 8: Optimization Results

	Thickness (mm)		
Variable	**Initial**	**SHERPA**	**Hybrid**
t1	5.00	5.68	5.48
t2	5.00	4.77	3.91
t3	5.00	4.12	3.67
t4	5.00	3.52	4.36
t5	5.00	6.58	6.05
t6	5.00	8.11	7.42

Responses	**Initial**	**SHERPA**	**SQP**
Max von Mises Stress (MPa)	235.53	79.25	99.58
Mass (kg)	405.00	436.0	407.61

From this table one can see that the global optimizing SHERPA algorithm significantly improved the design in this structural-acoustic problem. The von Mises stress at the critical locations on the structure reduced significantly from the initial design results, although the mass did increase. Then by applying the SQP local optimization method given the design parameters from SHERPA, the system's mass is reduced by nearly 30 kg while converging to the stress constraint. Although it appears that the design parameters do not significantly change from SHERPA to the hybrid results, a slight reduction in t1 and t2 which span the entire lengths of the duct system, allows for the large reduction in mass. In comparisons of the initial design and the sequentially applied hybrid optimization technique, the mass stays nearly the same, but the stress has been

significantly decrease to the point where acoustic loading would not affect the fatigue life of this system. With this optimization approach, one can see that there is a structural tendency in this particular problem. It can be observed that the top and bottom sections of the duct (t1) become thicker than the left and right sides (t2), from Table 8. This could be due to the fact that these areas are larger than the side areas, and have more effect in reducing the stresses at the critical point constraints applied at corner regions. Another observation from these results is that as the substructural panels get farther away from the acoustic pressure source, the thickness increases. This could be as a result of the system to compensate for the larger modes that are observed at the outlet of the duct system.

In this research, it is important to use a hybrid optimization approach because of the nature of the structural-acoustic problem. The dynamic system is dependent on time and frequency, and very sensitive to small steps especially around peak stresses. Utilizing a critical point constraints technique and a hybrid optimization approach that accounts for both global and local optimization schemes, allows for a better solution to be obtained in a design space that contains multiple local solutions.

6. Summary and Future Work

6.1. Conclusions

Acoustic loading is becoming more important in the aerospace industry as technology in aircraft advances and continues to push the design envelope. With the current demand for new air vehicle platforms the technical challenges are much more critical for a reliable and cost effective operation under new and adverse stipulations. The acoustic based design of aircraft subsystems explored in this work, establishes the ground work for structural-acoustic analysis and optimization in this multidisciplinary loading environment. Since the acoustic wave equations were related to the finite element method equation, the analysis and optimization procedures developed in this work can easily be implemented into larger model frameworks that include more of the aircraft model or additional loading sources. The optimization technique that was implemented can extend component life and prohibit acoustic detection by reducing the acoustic signature and related stress on the vehicle, resulting in heightened protection/safety and considerable financial savings.

To properly model an acoustic problem like the one presented in this document, multiple points need to be addressed to more accurately represent the actual environment. For instance, determining if the model should be represented as a

coupled or uncoupled FEA model is crucial. Uncoupled models are less computationally expensive because the fluid does not need to be modeled. In many cases this method works well, but if the fluid does have an effect on the system, the mode shapes and responses could be drastically different. Another important aspect to consider in acoustic related problems is whether the environment is internal or external. For problems involving an external acoustic boundary, like EEWS models, the unbounded domain needs to be accounted for. The thickness of the structure in acoustic environments is also important for reducing the pressure within the fluid. In the analysis presented in Chapter 4, the pressure was reduced nearly 20 dB when the thickness increased from 1 mm to 10 mm at one nodal location. Changing the material's thickness not only changes the pressure but also the frequency at which this pressure occurs. This information is pertinent for the design process because the frequencies, at which peak pressures are targeted to be reduced, could shift with the change in design. It was also apparent that models experiencing heavy structural-acoustic coupling effects become spatially dependent, as shown in the parametric studies at different nodal locations. The spatial dependency, along with the frequency dependency of the problem creates a multi-modal issue in which typical gradient based methods struggle to find optimal solutions. Utilizing a hybrid optimization process that involves both global search strategies and local gradient methods, along with a critical point constraints technique, proved very effective in reducing the acoustic related stress for the system. In this research, the optimization process was able to reduce the acoustic related stress by over half the magnitude of the stress in the baseline design, while relatively maintaining

the same mass. The techniques developed in this structural-acoustic optimization are of a relatively low frequency, but can easily be applied to problems experiencing a much higher range of excitation frequencies. The wide variety of aerospace applications that this research can be applied to ranges from LRS missions in which vehicles experience vibro-acoustics fatiguing issues on critical components during extended flight, to Intelligence Surveillance and Reconnaissance mission applications in which UAVs, like the conceptual models being explored by the GHO program by IARPA, are designed to contain more efficient and quiet power sources and propulsion systems in order to reduce the ability of the target to counter surveillance. However, the structural-acoustic analysis strategies and optimization procedures not only can be utilized for aerospace related applications, but any problem that experiences interaction and coupling effects between acoustics and structures.

6.2. Future Work

As the previous section specified, the research presented in this document establishes the ground work for structural-acoustic analysis and implements an optimization technique to account for a dynamic system dependent on space and frequency/time. The FE model that was utilized for most of the work was a simplified model representation of the exhaust system from an embedded engine aircraft. In future work, additional results should be obtained from more realistic duct configurations, like the one shown in Figure 42.

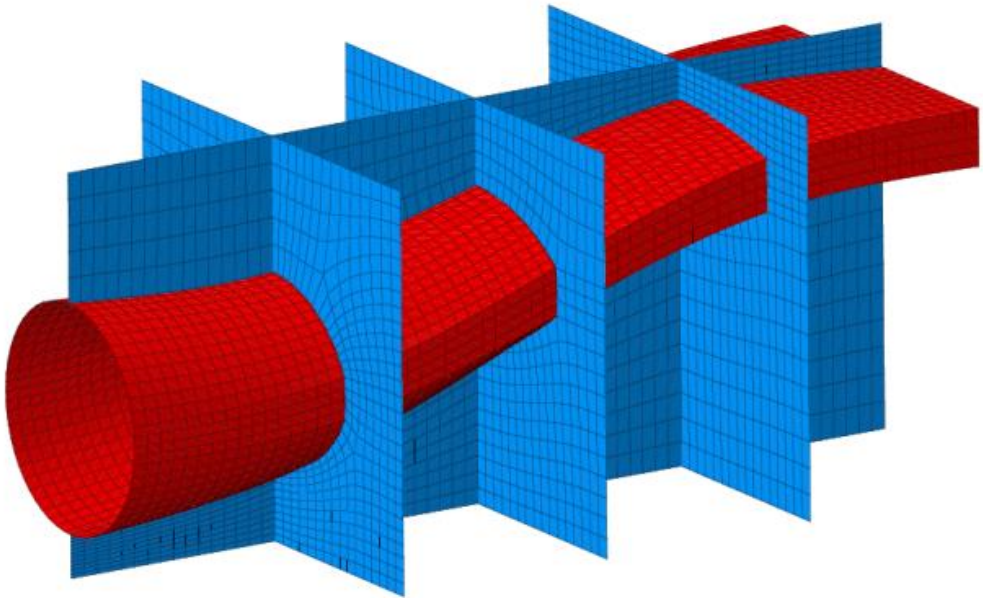

Figure 42: FE model of an embedded exhaust duct system

From preliminary investigations using this duct model, it was determined that the curved geometry resulted in even more acoustic-structure interaction. This is due to the increased reflection of acoustic pressure waves inside the curved duct compared to the rectangular straight duct model. This only further emphasizes the need to include acoustic analysis in these types of structures. A stress analysis of the model at a highly participating structural mode, shown in Figure 43, suggests again that the highest acoustic related stress concentration appears near the outlet of the duct system. This is very similar to the stress effects observed in the straight duct analysis.

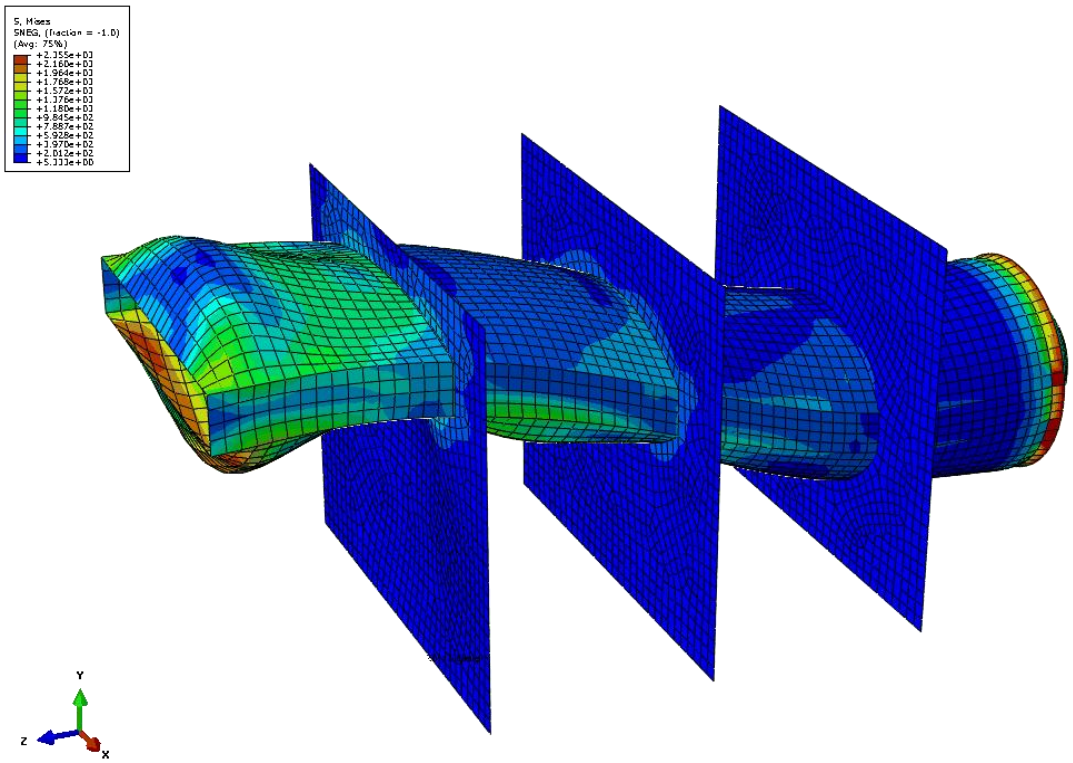

Figure 43: Stress analysis at the 3rd mode of the curved duct structure

In fatigue life prediction studies, reducing the stress in a system results in prolonging the fatigue life, which was emphasized in this work. However, in depth fatigue analysis was not primarily researched in this document, so structural fatigue comparisons could be included in future work.

In addition to more practical geometries being addressed, the inclusion of other participating loads needs to be evaluated. This would include the introduction of the intense thermal loading that is present in EEWS applications, which is known to create large thermal stresses and thermal expansion within the system [61]. Another participating discipline that could be included is CFD, in which the effect of the exhaust/fluid flow on the structure and the interactions of the fluid-structural model (FSI) could be investigated.

Another topic of future work could be additional exploration of optimization methods. A hybrid optimization method involving a critical point constraints technique was utilized in this work, which effectively improved the structural-acoustic coupled system. However, the location of the substructures was fixed in this analysis. If the design space truly includes the area between the duct and aircraft skins, possibly the structural supports would be more effective in other locations, orientations, and shapes as conceptually shown in Figure 44.

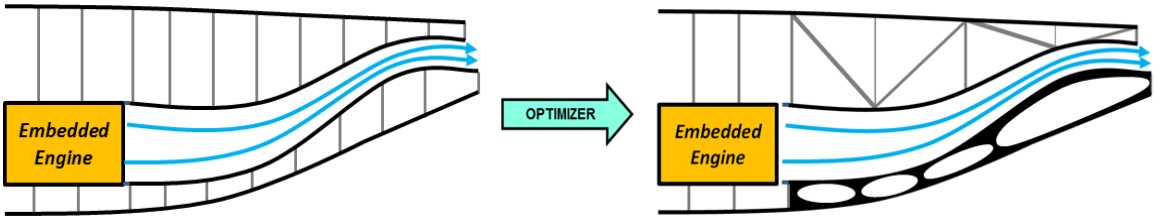

Figure 44: Conceptual future work optimization

This design strategy could be accomplished through shape or topology optimization methods, which are currently becoming more incorporated in a wide variety of engineering applications [62]. Wrapping these type of optimization techniques around a vibro-acoustic problem could have great benefits, especially when additional loading disciplines are included that can couple with the acoustic loads.

7. References

[1] Hollkamp, J.J., Gordon, R.W., and Spottswood, S.M., Nonlinear modal models for sonic fatigue response prediction: a comparison of methods, *Journal of Sound and Vibration*, Vol. 284, No. 3-5, pp. 1145-1163, 2005.

[2] Haney, M. A., and Grandhi, R. V., Consequences of material addition for a beam strip in thermal environment, *AIAA Journal*, Vol. 47, No. 4, pp. 1026-1034, 2009.

[3] Morshed, M.M., Hansen, C.H., and Zander, A.C., Prediction of acoustic loads on a launch vehicle fairing during liftoff, *Journal of Spacecraft and Rockets*, Vol. 50, No. 1, pp. 159-168, 2013.

[4] Gordon, R.W., and Hollkamp, J.J., Reduced order models for acoustic response prediction, *U.S. Air Force Research Laboratory Technical Report*, AFRL-RB-WP-TR-2011-3040, July 2011.

[5] Hong, K. L. and Kim, J., Analysis of free vibration of structural-acoustic coupled systems, *Journal of Sound and Vibration*, Vol. 188, No. 4, pp. 561-600, 1995.

[6] Pan, J. and Bies, D. A., The effect of fluid-structural coupling on sound waves in an enclosure-theoretical part, *The Journal of the Acoustical Society of America*, Vol. 87, No. 2, pp. 691-707, 1990.

[7] Pretlove, A. J., Forced vibrations of a rectangular panel backed by a closed rectangular cavity, *Journal of Sound and Vibration*, Vol. 3, No. 3, pp. 252-261,

1966.

[8] Atalla N. and Bernhard R. J., Review of numerical solutions for low-frequency structural-acoustic problems, *Applied Acoustics*, Vol. 43, No. 2, pp. 271-294, 1994.

[9] Brunner, D., Junge, M., and Gaul, L., A comparison of FE-BE coupling schemes for large-scale problems with fluid-structure interaction, *International Journal for Numerical Methods in Engineering*, Vol. 77, No. 5, pp. 664-688, 2009.

[10] Mejdi, A. and Atalla, N., Dynamic and acoustic response of bi-directionally stiffened plates with eccentric stiffeners subject to airborne and structure-borne excitations, *Journal of Sound and Vibration*, Vol. 329, No. 21, pp. 4422-4439, 2010.

[11] Dominguez, C., Stephan, E.P., and Maischak, M., FE/BE coupling for an acoustic fluid-structure interaction problem. Residual a posteriori error estimates, *International Journal for Numerical Methods in Engineering*, Vol. 89, No. 3, pp. 299-322, 2012.

[12] Ihlenburg, F., The medium-frequency range in computational acoustics: Practical and numerical aspects. *Journal of Computational Acoustics*, Vol. 11, No. 2, pp. 175-193, 2003.

[13] Dowell, E. and Peretti, L., Asymptotic modal analysis of a rectangular acoustic cavity excited by wall vibration, *AIAA Journal*, Vol. 30, No. 5, pp. 1191–1198, 1992.

[14] Morand, H. and Ohayon, R., Fluid structure interaction. *John Wiley & Sons, Chichester*, 1995.

[15] Everstine G. C., Finite element formulations of structural acoustics problems. *Computers & Structures*, Vol. 65, No. 2, pp. 307-321, 1997.

[16] Fang, B., Kelkar, A. G., Joshi, S. M., and Pota, H. R., Modelling, system identification, and control of acoustic-structure dynamics in 3-D enclosures," *Control Engineering Practice*, Vol. 12, No. 8, pp. 989-1004, 2004.

[17] Geng, H. C., Rao, Z. S., and Han, Z. S., New modeling method and mechanism analyses for active control of interior noise in an irregular enclosure using piezoelectric actuators, *Journal of the Acoustical Society of America*, Vol. 113, No. 3, pp. 1439– 1447, 2003.

[18] Meissner, M, Analytical and numerical study of acoustic intensity field in irregularly shaped room, *Applied Acoustics*, Vol. 74, No. 5, pp. 661– 668, 2013.

[19] Forouharmajd, F., Nassiri, P., and Monazzam, M.R., Noise pollution of air compressor and its noise reduction procedures by using an enclosure, *International Journal of Environmental Health Engineering*, pp. 1-20, 2013.

[20] Onuu, M.U., Road traffic noise in Nigeria: measurements, analysis, and evaluation of nuisance, *Journal of Sound and Vibration*, Vol. 233, No. 3, pp. 391-405, 2000.

[21] Rahmani, S., Mousavi, S.M., and Kamali, M.J., Modeling of road-traffic noise with the use of genetic algorithm, *Applied Soft Computing*, Vol. 11, No. 1, pp. 1008-

1013, 2011.

[22] Zannin, P.H.T., Diniz, F.B., Barbosa, W.A., Environmental noise pollution in the city of Curitiba, Brazil, *Applied Acoustics*, Vol. 63, No. 4, pp. 351-358, 2002.

[23] Astley, R.J., and Gabard, G., Computational aero-acoustics for aircraft noise prediction, *Journal of Sound and Vibration*, Vol. 330, No. 17, pp. 4081-4082, 2010.

[24] Sinibaldi, G., and Marino, L., Experimental analysis on the noise of propellers for small UAV, *Applied Acoustics*, Vol. 74, No. 1, pp. 79-88, 2013.

[25] Burley, C.L., Brooks, T.F., Humphreys, W.M., and Rawls, J.W., ANOPP landing-gear noise prediction with comparison to model-scale data, *International Journal of Aeroacoustics*, Vol. 8, pp. 445-475, 2009.

[26] Pavic, G., Air-borne sound source characterization by patch impedance coupling approach, *Journal of Sound and Vibration*, Vol. 329, No. 23, pp. 4907-44921, 2010.

[27] Janssens, M.H.A., Verheij, J.W., A pseudo-forces methodology to be used in characterization of structure-borne sound sources, *Applied Acoustics*, Vol. 61, pp. 285-308, 2000.

[28] Petersson, B.A.T., and Gibbs, B.M., Towards a structure-borne sound source characterization, *Applied Acoustics*, Vol. 61, pp. 325-343, 2000.

[29] Moorhouse, A.T., Elliott, A.S., and Evans, T.A., In situ measurement of the blocked forces of structure-borne sound sources, *Journal of Sound and Vibration*, Vol. 325, pp. 679-685, 2009.

[30] Gibbs, B.M., Uncertainties in predicting structure-borne sound power input into buildings, *Journal of the Acoustical Society of America*, Vol. 133, No. 5, pp. 2678-2689, 2013.

[31] Lee, D.H., Optimal placement of constrained-layer damping for reduction of interior noise, *AIAA Journal*, Vol. 46, No. 1, pp. 75-83, 2008.

[32] Olhoff, N., Optimal design of vibrating circular plates. *International Journal of Solids and Structures*, Vol. 6, pp. 139-156, 1970.

[33] Thambiratnam, D. P. and Thevendran, V., Optimum vibrating shapes of beams and circular plates. *Journal of Sound and Vibration*, Vol. 121, No. 1, pp. 13-23, 1988.

[34] Pritchard, J. I., Adelman, H. M., and Haftka, R. T., Sensitivity analysis and optimization of nodal point placement for vibration control. *Journal of Sound and Vibration*, Vol. 119, No. 2, pp. 277-289, 1987.

[35] Bai, M. R. and Liu, B., Determination of optimal exciter deployment for panel speakers using the genetic algorithm. *Journal of Sound and Vibration*, Vol. 269, No. 3-5, pp. 727-743, 2004.

[36] Lee, K. H. and Park, G. J., A global robust optimization using kriging based approximation model. *JSME International Journal Series C Mechanical Systems, Machine Elements and Manufacturing*, Vol. 49, No. 3, pp. 779-788, 2006.

[37] Fritze, D., Marburg, S., and Hardtke, H., Estimation of radiated sound power: A case study on common approximation methods. *Acta Acustica united with Acustica*, pp. 833-842, 2009.

[38] Qzakça, M. and Hinton, E., Free vibration analysis and optimisation of axisymmetric plates and shells: shape optimization. *Computers & Structures*, Vol. 52, No. 6, pp. 1199-1211, 1994.

[39] Ranjbar, M., Marburg, S., and Hardtke, H., Structural-acoustic optimization of a rectangular plate: a tabu search approach. *Finite Elements in Analysis and Design*, Vol. 50, pp. 142-146, 2012.

[40] Ranjbar, M. and Marburg, S., Vibroacoustic optimization of mechanical structures: a controlled random search approach. *Advanced Materials Research*, Vol. 622, pp. 158-161, 2013.

[41] Akl, W., El-Sabbagh, A., Al-Mitani, K., and Baz, A., Topology optimization of a plate coupled with acoustic cavity, *International Journal of Solids and Structures*, Vol. 46, pp. 2060-2074, 2009.

[42] Jensen, J.S., Pedersen, N.L., On maximal eigenfrequency separation in two-material structures: the 1D and 2D scalar cases. *Journal of Sound and Vibration*. Vol. 289, 967–986, 2006.

[43] Yoon, G.H., Jensen, J.S., and Sigmund, O., Topology optimization of acoustic–structure interaction problems using a mixed finite element formulation.

International Journal for Mechanical Methods in Engineering, Vol. 70, pp. 1049-1075, 2007.

[44] Maeda, Y., Nishiwaki, S., Izui, K., Yoshimura, M., Matsui, K., and Terada, K., Structural topology optimization of vibrating structures with specified eigenfrequencies and eigenmode shapes, *International Journal for Numerical Methods in Engineering*, Vol. 67, No. 5, pp. 597-628, 2006.

[45] Bendsoe, M. P., Lund, E., Olhoff, N., and Sigmund, O., Topology optimization - broadening the areas of application. *Control and Cybernetics*, Vol. 34, No. 1, pp. 7-35, 2005.

[46] Du, J. and Olhoff, N., Minimization of sound radiation from vibrating bi-material structures using topology optimization, *Structural and Multidisciplinary Optimization*, Vol. 33, No. 4-5, pp. 305-321, 2007.

[47] Denli, H. and Sun, J. Q., Structural-acoustic optimization of sandwich structures with cellular cores for minimum sound radiation, *Journal of Sound and Vibration*, Vol. 301, No. 1-2, pp. 93-105, 2007.

[48] Denli, H. and Sun, J. Q., Structural–acoustic optimization of sandwich cylindrical shells for minimum interior sound transmission, *Journal of Sound and Vibration*, Vol. 316, pp. 32-49, 2008.

[49] Franco, F., Cunefare, K. A., and Ruzzene, M., Structural-Acoustic Optimization of Sandwich Panels, *Journal of Vibration and Acoustics*, Vol. 129, No. 3, pp. 330-340, 2007.

[50] Bregant, L. and Puzzi, S., Optimization by evolutionary algorithms of free-layer damping treatments on plates, *International Journal of Acoustics and Vibration*, Vol. 8, No. 1, pp. 15-20, 2003.

[51] Aginsky, Z. and Gottlieb, O., Nonlinear bifurcation structure of panels subject to periodic acoustic fluid-structure interaction, *AIAA Journal*, Vol. 50, No. 9, pp. 1979-1992, 2012.

[52] Monnigmann, M., Marquardt, W., Bischof, C. H., Beelitz, T., Lang, B., and Willems, P., A hybrid approach for efficient robust design of dynamic systems, *SIAM Review*, Vol. 49, No. 2, pp. 236-254, 2007.

[53] Yildiz, A. R., Ozturk, N., Kaya, N., and Ozturk, F., Hybrid multi-objective shape design optimization using Taguchi's method and genetic algorithm, *Structural and Multidisciplinary Optimization*, Vol. 34, No. 4, pp. 317-332, 2007.

[54] Everstine, G.C., *Structural analogies for scalar field problems*, Journal of Numerical Methods in Engineering, Vol. 17, pp. 471-476, 1981.

[55] Sengpiel, E., Microphone recording techniques and studio technology: decibel table, *Sengpielaudio*, 8 July 2013. Web. 4 June 2012.

[56] ABAQUS Theory Manual (2012) Version 6.12. Dassault Systems Corp.

[57] Sandberg, G., Wernberg, P., and Davidsson, P., Fundamentals of Fluid-Structure-Interaction, Lund AB, Sweden, 2004.

[58] Vogel, R.N., and Grandhi, R.V., Structural Acoustic Analysis and Design of Aircraft Components, AIAA-2012-5557, MAO Conference, Indianapolis, IN, September 2012.

[59] Vogel, R.N., and Grandhi, R.V., Acoustic Analysis and Optimization of Embedded Exhaust-Washed Structures, ISSMO-2013-5429, 2013, WCSMO Conference, Orlando, FL, May 2013.

[60] HEEDS MDO User Manual, Ver. 6.1, Red Cedar Technology, Inc. East Lansing, MI, 2011.

[61] Deaton, J. D., and Grandhi, R. V., Stiffening of restrained thermal structures via topology optimization, *Structural and Multidisciplinary Optimization*, DOI: 10.1007/s00158-013-0934-5, April 2013.

[62] Deaton, J. D., and Grandhi, R. V., A Survey of Structural and Multidisciplinary Topology Optimization: post 2000, *Structural and Multidisciplinary Optimization*, May 2013.

[63] Rajalingham, C., Bhat, R. B., and Xistris, G. D., Natural vibration of a cavity backed rectangular plate using a receptor-rejector system, *Journal of Vibration and Acoustics*, Vol. 117, No. 4, pp. 416-423, 1995.

[64] Du, J. T., Li, W. L., Xu, H. A., and Liu, Z. G., Vibro-acoustic analysis of a rectangular cavity bounded by a flexible panel with elastically restrained edges, *The Journal of the Acoustical Society of America*, Vol. 131, No. 4, pp. 2799-2810, 2012.

[65] Bahaideen, F.B., Saleem, A., Hussain, K., Ripin, Z., Ahmad, Z., Samad, Z., Badarulzman, N., Fatigue behavior of aluminum alloy at elevated temperature, *Modern Applied Science*, Vol. 3, No. 4, pp. 52-61, 2009.

[66] Cowles, B.A., High cycle fatigue in aircraft gas turbines – an industry perspective: FEM and measurement, *Journal of Sound and Vibration*, Vol. 193, No. 3, pp. 669-690, 1996.

8. Appendix

The following sections in this chapter will discuss various acoustic analysis investigations and validations that were essential in understanding the acoustic behavior in a structural acoustic environment. These results contain findings that were imperative in developing better future acoustic models and producing the analysis procedure utilized in the work.

Section 8.1 of the Appendix includes a large documented study on chamber or room acoustics. The model created in this EEWS investigation contains rigid walls, so the boundary conditions can be modeled using Eq. (16). Using rigid wall boundaries significantly reduces the complexity of the analysis, because the coupling terms, as well as the structural equation of motion, drops out of the analysis. Therefore, a problem like this can be solved analytically for the natural frequencies, which was done and validated against the FEA results from Abaqus. Section 8.2 of the Appendix contains a study in which results from a journal paper on a fluid-structural coupled system was validated through the use of Abaqus. This study proved that Abaqus has the ability to model systems that contain interaction between a fluid and structural domain. The mesh convergence study for the representative EEWS used in the research is displayed in Section 8.3, and the fatigue life prediction estimate that was used to obtain the stress constraint in the optimization problem statement can be found in section 8.4.

8.1. Room/Chamber Acoustics

The objective of this section is to study the effect of low frequency acoustics on a small chamber. As the result of its size and geometry, a room excessively amplifies sound at certain frequencies. This is the result of resonant standing waves (acoustic resonances/modes) of the room. Large rooms also have many resonances, but only the low-frequency ones are discrete and distinct. The low frequency resonances typically accommodate most of the acoustic energy build up in acoustic systems. However, these low frequency resonances are also typically unaffected by the sound absorbing material in the room.

A chamber with the dimensions of 7m x 5m x 2.4m is studied for this analysis. Air is the fluid present within the chamber which has the properties of 343m/s for the wave speed, and 1.2 kg/m^3 for the density. A schematic of the cavity can be seen below.

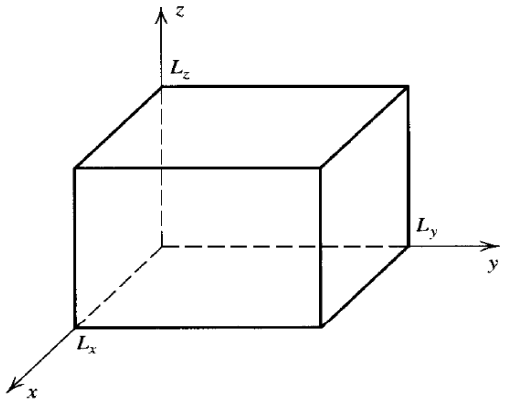

Figure 45: Rectangular cavity with dimension Lx, Ly, and Lz

This box could represent any type of cavity, such as a simple room, a basic box wing, or any other hexahedral space that has few openings and fairly rigid walls. Analytically, the resonant frequencies and mode shapes can be determined over any base frequency range. If the surfaces of the cavity are assumed to be perfectly rigid, the normal component of the particle velocity vanishes at the boundaries, and produces the following equations for the 3D space:

$$\left(\frac{\partial p}{\partial x}\right)_{x=0} = \left(\frac{\partial p}{\partial x}\right)_{x=L_x} = 0$$

$$\left(\frac{\partial p}{\partial y}\right)_{y=0} = \left(\frac{\partial p}{\partial y}\right)_{y=L_y} = 0 \tag{62}$$

$$\left(\frac{\partial p}{\partial z}\right)_{z=0} = \left(\frac{\partial p}{\partial z}\right)_{z=L_z} = 0$$

Since there are no openings for the acoustic waves to escape and the walls are rigid, the most appropriate solutions of the wave equation are standing waves. The substitution of Eq. (63),

$$p(x, y, z, t) = X(x)Y(y)Z(z)e^{i\omega t} \tag{63}$$

which is the acoustic pressure in terms of the three dimensional space and time, into the wave equation (9), along with the separations of variable results in Eq. (64) will help accomplish finding the solution,

$$\left(\frac{d^2}{dx^2} + k_x^2\right)\boldsymbol{X} = 0$$

$$\left(\frac{d^2}{dy^2} + k_x^2\right)\boldsymbol{Y} = 0 \tag{64}$$

$$\left(\frac{d^2}{dz^2} + k_z^2\right)\boldsymbol{Z} = 0$$

This requires that the angular frequency must be given by the following equation:

$$\left(\frac{\omega}{c}\right)^2 = k^2 = k_x^2 + k_x^2 + k_z^2 \tag{65}$$

Applying the rigid boundary conditions from eq. (62) shows that the cosines are appropriate solutions, so eq. (63) now becomes:

$$\boldsymbol{p}_{lmn} = \boldsymbol{A}_{lmn}\cos(k_{xl}x)\cos\left(k_{ym}y\right)\cos(k_{zn}z)\,e^{i\omega_{lmn}t} \tag{66}$$

Where the values for the acoustic wave number k are:

$$_{xl} = \frac{l\pi}{L_x} \qquad l = 0, 1, 2, \ldots$$

$$k_{ym} = \frac{m\pi}{L_y} \qquad m = 0, 1, 2, \ldots \tag{67}$$

$$k_{zn} = \frac{n\pi}{L_z} \qquad n = 0, 1, 2, \ldots$$

Using the values of k, the angular frequency of the vibration in radians per second can be calculated using the equation:

$$\omega_{lmn} = c\sqrt{\left(\frac{l\pi}{L_x}\right)^2\left(\frac{m\pi}{L_z}\right)^2\left(\frac{n\pi}{L_z}\right)^2} \tag{68}$$

For the frequency in hertz, this equation can be simplified into:

$$\omega_{l,m,n} = c\sqrt{\left(\frac{l}{2L_x}\right)^2 + \left(\frac{m}{2L_y}\right)^2 + \left(\frac{n}{2L_z}\right)^2} \tag{69}$$

The values of $l, m, \text{and } n$ correspond to the integer values that determine the resonance in each direction and the $L_x, L_y, \text{and } L_z$ variables correspond to the length of the sides of the chamber. By substituting the values 0, 1, 2, … in for l, m, n, one can obtain the resonant frequencies for the model. This process can be analytically done by hand, but it also can be done systematically by creating a MATLAB code to cycle through the many combinations of values and sorting to obtain the lowest frequencies first. Using this technique, the first 15 the resonant frequencies could be obtained and are displayed in Table 9.

Next, the analytical resonant frequencies are validated by running an eigenfrequency analysis in the finite element analysis package, Abaqus. After the model was created and the normal modes found in Abaqus, the results were tabulated in Table 10. From observation, one can see that the results for using the acoustic analysis software correspond very well to the analytically solved frequencies.

Table 9: Theoretical resonant frequencies of the chamber

	l	m	n	(ω) radians/sec	(f) Hz
1	1	0	0	154.387	24.571
2	0	1	0	216.142	34.400
3	1	1	0	265.617	42.274
4	2	0	0	308.774	49.143
5	2	1	0	376.906	59.987
6	0	2	0	432.283	68.800
7	0	0	1	450.295	71.667
8	1	2	0	459.025	73.056
9	3	0	0	463.161	73.714
10	1	0	1	476.026	75.762
11	0	1	1	499.482	79.495
12	3	1	0	511.111	81.346
13	1	1	1	522.798	83.206
14	2	2	0	531.234	84.549
15	2	0	1	545.992	86.897

Table 10: Resonant frequencies of air inside chamber in Hz

Mode	Theoretical	Abaqus
1	24.6	24.6
2	34.4	34.4
3	42.3	42.3
4	49.1	49.1
5	60.0	59.9
6	68.8	68.8
7	71.7	71.6
8	73.1	73.0
9	73.7	73.7
10	75.8	75.7
11	79.5	79.4
12	81.3	81.2
13	83.2	83.1
14	84.5	84.4
15	86.9	86.8

8.2. Partially Coupled Duct Analysis

The objective of this study is to further investigate the validity of the structural-acoustic coupling equations and to begin looking at preliminary studies on the simplified EEWS. In the previous section, modal analysis was conducted on the air cavity with surround rigid boundary conditions. However, aerospace vehicles contain flexible structural walls that have drastically different effects than systems containing only rigid walls. To validate the coupling equations and interaction effects presented in this research, a partially coupled plate-cavity system is investigated that was previously studied in the work by Rajalingham et al. [63] and Du et al. [64]. In this analysis a simply supported flexible panel with dimensions of 203.2 mm x 406.4 mm and thickness of 1.524 mm is coupled to an acoustic cavity of dimensions 203.2 mm x 406.4 mm x 609.6 mm. The material properties of the structure are: Young's modulus = 71 GPa, Poisson's ratio = 0.3, and mass density = 2700 kg/m^3. The properties of the air are: speed of sound = 344 m/s, and air density = 1.21 kg/m^3. In this problem, the one surface of the fluid is coupled with the structure and the rest of the surfaces are again given rigid boundary conditions. The FE model used in this analysis can be seen in the figure below.

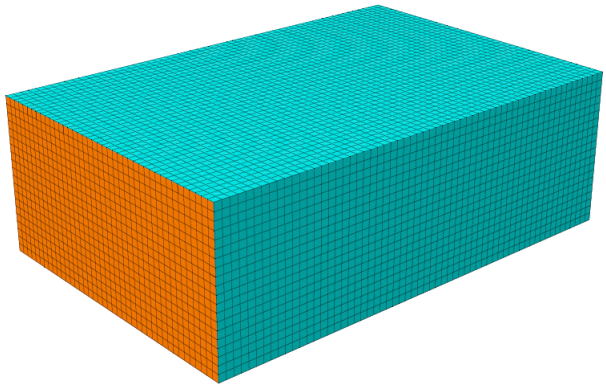

Figure 46: FE model of plate-cavity system

The results obtained from a normal modes analysis are compared with the results from literature in the following table. Here Ref 63 and Ref 64 corresponds to the results obtained from Rajalingham et al. [63] and Du et al [64] respectively.

Table 11: First six modal frequencies for the coupled panel-cavity system

	Frequency (Hz)			% Difference	
Mode	**Ref 63**	**Ref 64**	**Abaqus**	**A-63**	**A-64**
1	113.91	114.06	114.03	0.11	0.03
2	177.48	178.04	177.57	0.05	0.26
3	280.71	281.02	280.96	0.09	0.02
4	295.97	296.62	296.39	0.14	0.08
5	379.77	379.71	380.15	0.10	0.12
6	423.05	423.11	423.12	0.02	0.00

As one can see from Table 11, the results obtained using Abaqus correspond very closely to the results from the literature. The largest percentage difference observed is in Mode 2 between the current results and Ref 64, which corresponds to a difference of .47 Hz. From this analysis, one can see that the structural-acoustic equations used in this research are capable of capturing the coupling effects of this problem. Since the analysis is validated against published work, we can assume that Abaqus is capable of

modeling other fully-coupled problems with additional structural boundaries and more complicated geometries at high accuracy.

8.3. FEA Mesh Convergence

This section briefly shows the mesh convergence results for the finite element modeled discussed in Chapter 4. As previously specified, in Abaqus, coupling surfaces and elements do not necessarily have to match up at every nodal location due to interpolation equations that are used at these interfaces. Therefore a courser fluid mesh in a structural-fluid coupled system can save computational time while still retaining accuracy. However, the analysis will be more accurate if the nodes present on the outside surface of the fluid do share nodes with the structure. This strategy, shown in Figure 47 where the red lines connecting the fluid and structural nodes represent that that these nodes are shared, influenced the way the number of elements was selected in each convergence analysis.

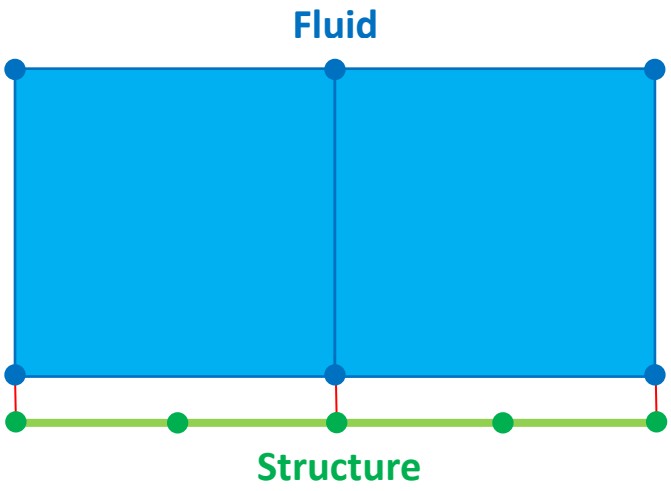

Figure 47: Node sharing between structure and fluid mesh

Typical convergence studies double the amount of elements used for each evaluation, however, due to geometry restrictions and limitations established for nodal sharing between the fluid and structure, selecting the size of the elements had to be done carefully. In this analysis, this issue was accounted for by reducing the global element size (element side lengths between nodes) for both the fluid and structure at equivalent intervals.

The first convergence study was conducted on the 3D fluid domain modeled using AC3D8 elements. The meshed models are shown in Figure 48, and the convergence results for frequency in a normal modes analysis and pressure from a steady-state dynamics analysis are shown in Figure 49 and 50 respectively.

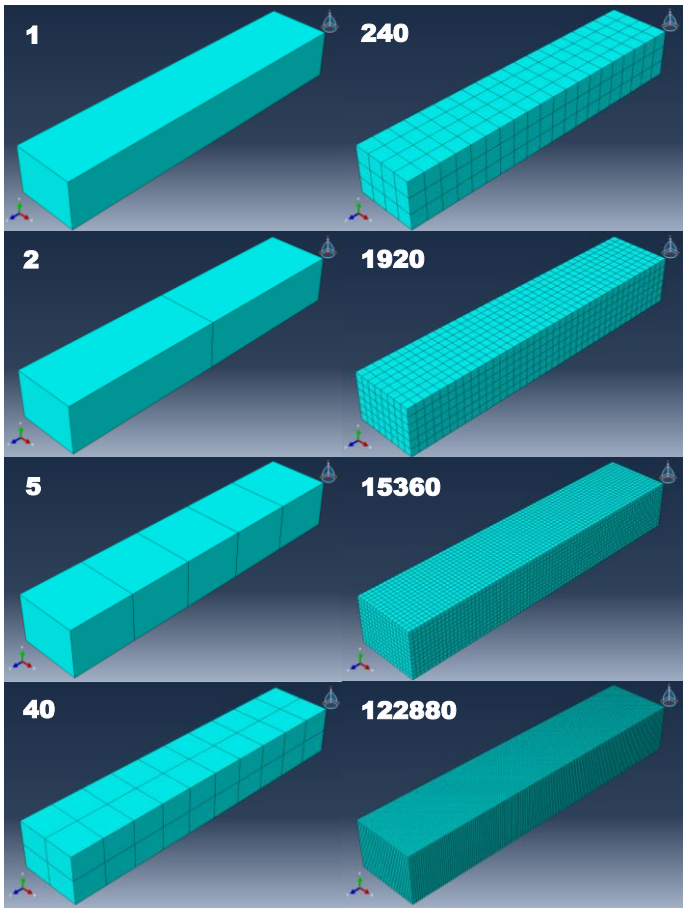

Figure 48: Meshed fluid models with corresponding elements used

From Figure 49, one can see that convergence, at even modes 4 and 5, is nearly obtained with only 240 elements. To further check convergence, the steady-state dynamics analysis was evaluated where a dynamic pressure load was applied to the model, specified in Chapter 4, and a pressure measurement was taken at a corner node located at the rear of the fluid domain. The resulting pressures plotted vs. number of elements can be seen in Figure 50 for the frequency selected at the 3rd resonating mode for the fluid system (70 Hz). In this Figure, 240 elements do not quite capture the converged pressure. Therefore, 1920 elements, which properly modeled the acoustic behavior in both studies, were selected to accurately model the fluid domain. Note that

during this process, acoustic infinite elements (ACIN3D4) were coupled to the rear of the finite fluid cavity. They converged at the same "global element size" rate as the 3D acoustic elements, which resulted in an infinite acoustic boundary of 48 elements. This element mesh can be seen in Figure 14.

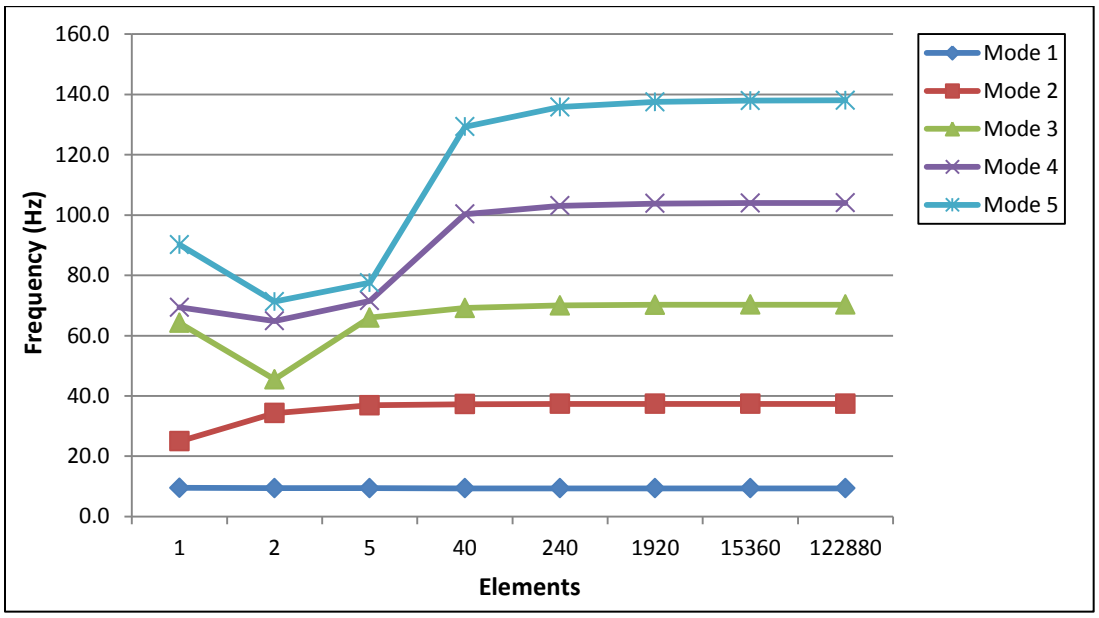

Figure 49: Frequency convergence study for fluid domain

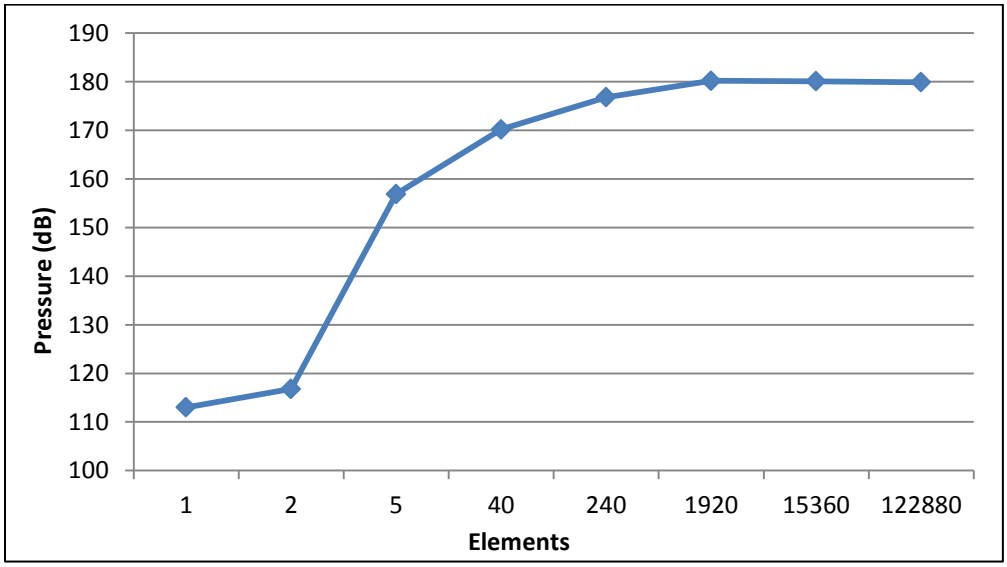

Figure 50: Pressure convergence study for fluid domain (70 Hz)

The next convergence study was conducted on the structural-fluid coupled model to find the number of structural elements (S4) needed to model the structure. In this analysis the structure was coupled to the previously converged fluid mesh and the same normal modes analysis and steady-state dynamics analysis was evaluated. The meshed models are shown in Figure 51, and the convergence results are shown in Figure 52 and 53.

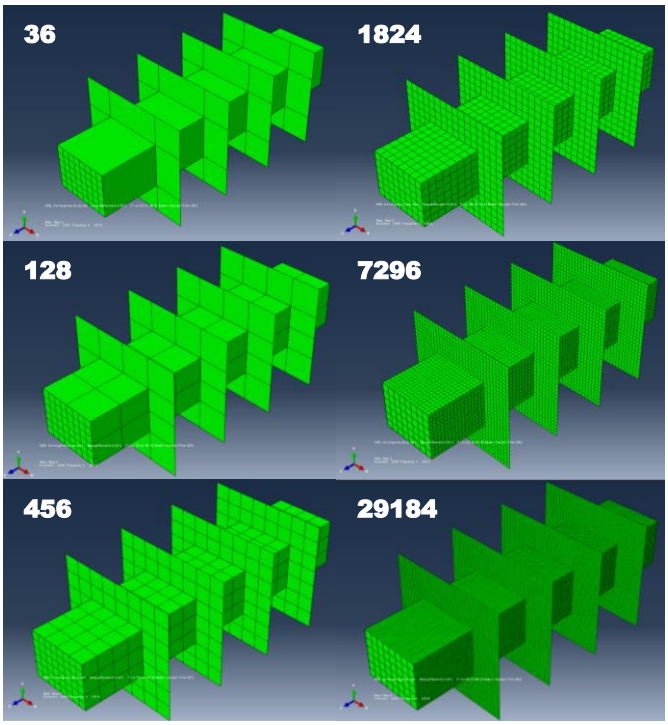

Figure 51: Meshed coupled fluid-structure models with corresponding elements used

Due to the partitioning of the substructural panels where smaller elements were initially needed to model the different geometry, only the elements on the duct model of the structure were refined in the first three studies: for 36, 40, and 52 elements. Since the model appears the same in the first three cases, only one was shown in Figure 51. Once the element size was reduced to a size smaller than the partitions, the element refining

was continued in the same way as the fluid mesh. From Figure 52, it can be observed that approximately 456 elements can capture the converged frequencies of the first 5 modes. However, in a similar manner to the fluid study, a steady-state dynamics analysis was conducted (at the 5th resonating mode of the structural-acoustic system) to determine if the pressure was converged. Similarly to the fluid study, Figure 53 shows that it requires more elements to converge the pressure results pressure results. For this reason, the model containing 7296 structural elements was selected. Therefore, the converged model contains 1920 acoustic brick elements, 48 acoustic infinite elements, 7296 structural elements (4480 duct and 2816 substructures), and an additional 192 structural elements to model the front loading plate that approximates the acoustic loading from the engine.

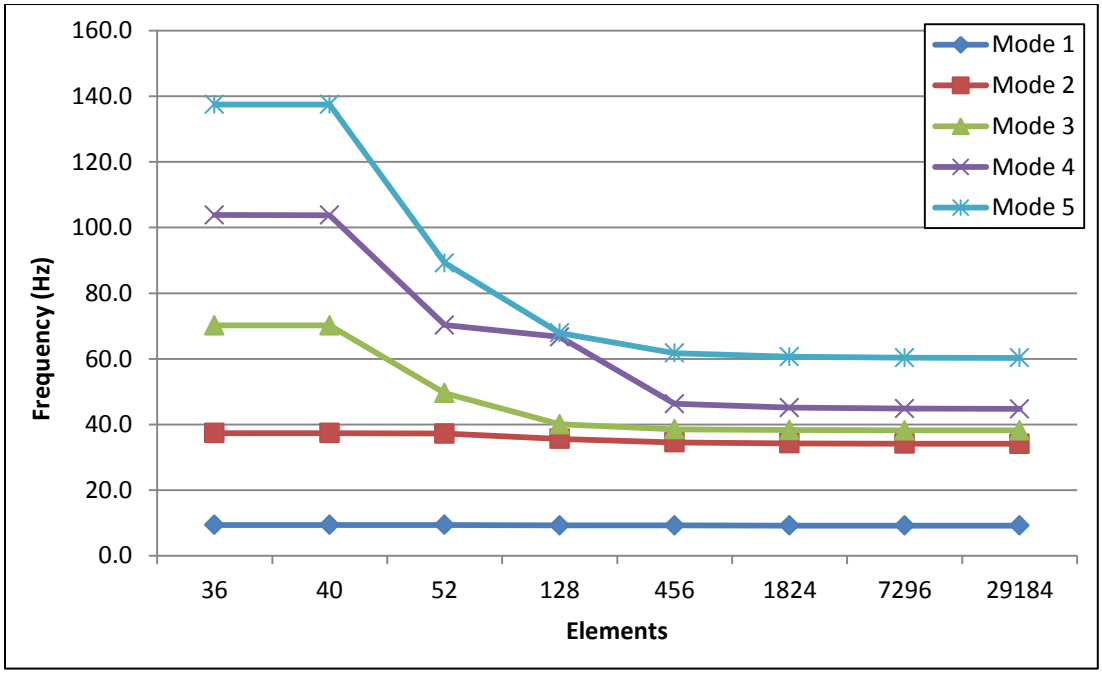

Figure 52: Frequency convergence study for structural-fluid coupled system

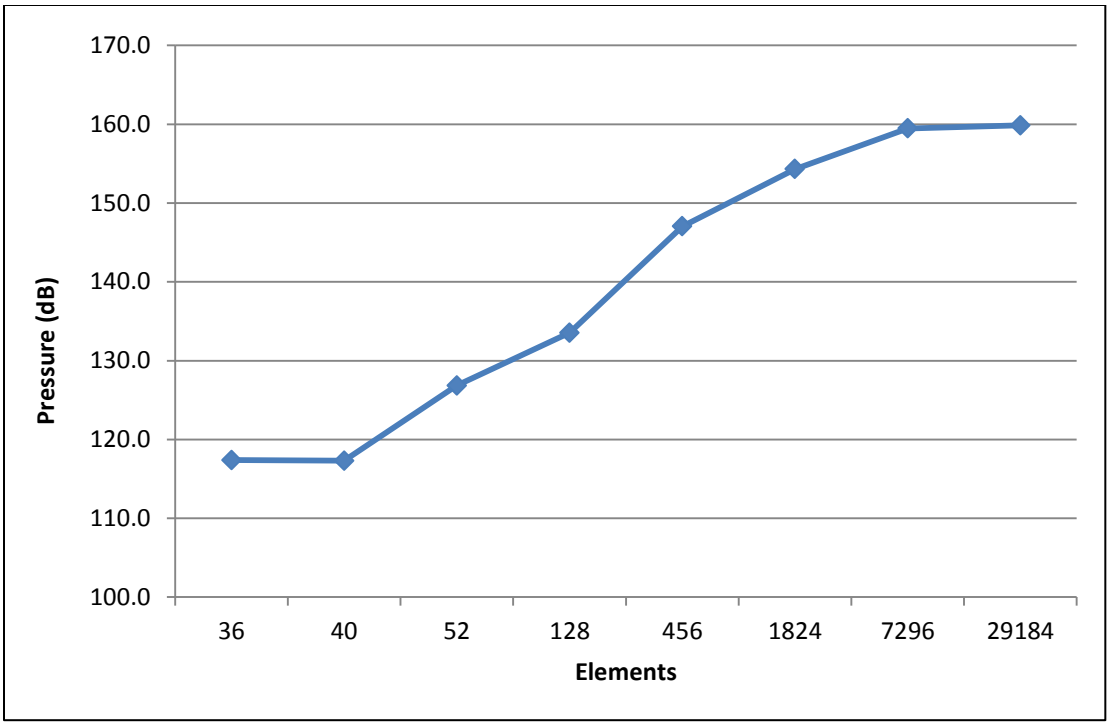

Figure 53: Pressure convergence study for structural-fluid coupled system (60 Hz)

8.4. Fatigue Calculation

In order to establish an approximate stress constraint value that would yield a life cycle for the structure, a fatigue life prediction can be made using a stress-life approach. FEA can be used to establish the hot spots for each load case based on a load spectrum. The stress levels obtained from this step can be represented as variable amplitude loading which can be used to compute the fatigue life of the component. Typically a Rainflow Cycle Counting method can be used to calculate the mean stress and amplitude from the loading effects, which in turn is used to calculate the fatigue strength and cycles to failure. Although in this research, similar stress values can be obtained from the loading spectrum, the changing design through optimization would require fatigue analysis per

iteration. Therefore, a stress value can be back calculated from an ideal life cycle prediction to obtain a stress constraint that would be used in the optimization problem statement. First however, the equations defining the fatigue strength and the cycles at this fatigue strength must be established. Here the Modified Goodman equation can be used to obtain the fatigue strength of each load segment, and this equation is given by:

$$\frac{\sigma_a}{\sigma_{N_f}} + \frac{\sigma_m}{\sigma_u} = 1 \tag{62}$$

where σ_a is the stress amplitude, σ_m is the mean stress, σ_{N_f} is the fatigue strength at N_f cycles, and σ_u is the ultimate strength of the material. The material used in this research is Aluminum Alloy 2024-T4, which has an ultimate strength of 469 MPa. The number of cycles to failure for the structural components can be found by using Basquin's Equation, which uses the fatigue strength and values obtained from the S-N curve for Aluminum 2024-T4. This equation can be shown as:

$$\sigma_{N_f} = A(N_f)^B \tag{63}$$

where the S-N curve constants, $A = 1479$ and $B = -.147$, were obtained from the experimental results of aluminum alloy in Bahaideen et al [65]. Typically a cycle of $N_f > 10^6$ constitutes a life cycle (infinite life) for normal stressed components, however, high cycle aircraft fatigue sometimes requires an even larger life cycle (10^8-10^{10}) due to safety issues and additional loading [66]. Therefore, if 10^8 is the life cycle to be achieved in this optimization, the resultant fatigue strength for Aluminum 2024-T4 is 70.3 MPa. Substituting this value into Eq. (62), and using an estimate on the minimum

stress the system experiences, the stress magnitude of 107.5 MPa can be obtained. This stress value (rounded to 100 MPa for additional fatigue longevity) is then used as the stress constraint in the critical point constraints optimization technique specified in Chapter 5. Of course, this value is only an approximation for the constraint in the problem setup in this research, and can easily be changed to a more accurate or meaningful value in the future.